A Quest for PeVatrons Employing Radio Detection of Extensive Air Showers

Zur Erlangung des akademischen Grades eines
Doktors der Naturwissenschaften
von der KIT-Fakultät für Physik
des Karlsruher Instituts für Technologie (KIT)

genehmigte
Dissertation

von Aswathi Balagopal V. (M.Sc.)
aus Kozhikode, Indien

Tag der mündlichen Prüfung: 12.02.2019
Referent: Prof. Dr. Dr. h.c. Johannes Blümer
Korreferent: Prof. Dr. Thomas Schwetz-Mangold
Betreuer: Dr. Andreas Haungs

Abstract

A Quest for PeVatrons Employing Radio Detection of Extensive Air Showers

The origin of cosmic rays from the knee and beyond, i.e. with a primary energy of 2×10^{15} eV and above, remains an open question even today. Several experiments have tried to search for possible candidate PeVatrons (particle accelerators) within our Galaxy that can produce these PeV energy particles. Most of these experiments employ the method of detection of the air showers of PeV gamma rays as they interact with the atmosphere, by measuring their secondary particles. In this thesis, a new realm for the detection of air showers generated by PeV gamma rays is explored by using the radio detection technique.

The radio detection technique for the observation of air showers has so far only been applied for the detection of cosmic rays. This is done in the energy range of $10^{16.5}$ eV and above. This thesis explores the method for lowering the energy threshold of radio detection to use it for the detection of PeV gamma rays, that can directly point to PeVatrons. In particular, the focus is on a candidate PeVatron at the Galactic Centre that was observed by H.E.S.S.

The South Pole, where the IceCube Neutrino Observatory is under operation, is an excellent location for observing the Galactic Centre. The Galactic Centre has an around-the-clock exposure from here, and is constantly visible at a zenith angle of 61°. This low elevation renders it difficult for the existing particle-detector array at the South Pole to detect the air showers. Here, we attempt to tap into the unattenuated radio signals (unlike the particle content) of such showers on the ground. With the goal of measuring these radio signals, the work of this thesis successfully achieves the following:

* The frequency band of operation is optimised to obtain an enhanced signal-to-noise ratio for air showers. On performing the measurement in the band 100-190 MHz, the energy threshold for the detection of air showers using the radio technique is lowered by an order of magnitude. This enables the detection of PeV gamma rays from the Galactic Centre.

* The expected number of gamma rays at PeV energies, the fraction of them that can be detected by a radio array at the surface of IceCube, and the required

gamma-hadron separation to detect these gamma rays are determined. With this, the sensitivity of the radio array to a flux of PeV gamma rays from the Galactic Centre is established.

* The capability of IceTop—the air-shower particle detector array of IceCube—to act as a trigger for the radio antennas is investigated. An approach utilising the method of constant intensities is used for determining the energy threshold of IceTop for the detection of air showers in the direction of the Galactic Centre. This revealed the IceTop array to have a threshold that is too high to be used as an external trigger for the radio array (for PeV-Radio). The future scintillator array as an external trigger as well as self-triggering of the radio array are seen as alternatives that will require further optimisation.

The promising results of the study done in this thesis resulted in a planned surface-radio array at the IceCube Observatory. This is included in the ongoing enhancement activities of IceTop. Two prototype antennas will be installed at the South Pole in the Austral summer of 2018/2019 as a first step towards this.

Following the work done in this thesis, it was realised that the simplistic frequency optimisation is a novel technique that can be used for all radio air-shower experiments. A further study reveals this optimal frequency band to be universal. Consequently, GRAND, a future radio air shower array for the detection of high energy neutrinos and cosmic rays, also plans to use an optimised frequency band for improving its performance.

Zusammenfassung

Die Suche nach PeVatrons mittels der Radiodetektion ausgedehnter Luftschauer

Der Ursprung der kosmischen Strahlung bei Energien oberhalb des Knies von 2×10^{15} eV ist bis heute ungekärt. Mehrere Experimente suchen nach möglichen PeVatrons (Teilchenbeschleuniger) in unserer Galaxie, also Objekte die Teilchen mit Energien im PeV-Bereich (10^{15} eV) produzieren können. Die meisten dieser Experimente messen dabei die Sekundärteilchen von Luftschauer generiert von PeV-Gammastrahlen, welche in Wechselwirkung mit unserer Atmosphäre entstehen. In dieser Arbeit wird als neue Methode für die Detektion von Luftschauern aus PeV-Gammastrahlen die Möglichkeiten von Radiomessungen untersucht. Die Radiotechnik zur Beobachtung von Luftschauern wurde bisher nur zur Detektion von kosmischer Strahlung in einem Energiebereich oberhalb von $10^{16.5}$ eV eingesetzt. In dieser Arbeit wird untersucht, ob es möglich ist die Energieschwelle der Radiomessung soweit zu senken, dass PeV-Gammastrahlen detektiert werden können, welche direkt aufgrund der fehlenden Ladung zu ihrer Quelle weisen. Insbesondere liegt der Fokus auf einem PeVatron Kandidaten im Galaktischen Zentrum, der von H.E.S.S. beobachtet wurde. Der Südpol, an dem das IceCube Neutrino Observatorium betrieben wird, ist ein ausgezeichneter Standort für die Beobachtung des Galaktischen Zentrums. Das Galaktische Zentrum ist von hier aus ständig unter einem Zenitwinkel von 61° sichtbar. Dieser grosse Zenitwinkel macht es jedoch für die bestehende Teilchendetektoren am Südpol schwierig, die Luftschauer zu detektieren. Die Radiotechnik ist für solche Zenitwinkel ideal, da das Radiosignal nicht durch die Atmosphäre abgeschwächt wird. Im Rahmen dieser Arbeit wurden verschiedene Aspekte untersucht, um zu entscheiden ob eine solche Messung erfolgreich sein kann:

* Das genutzte Frequenzband wurde optimiert, um ein verbessertes Signal-zu-Rausch-Verhältnis f ür Luftschauer zu erhalten. Damit konnte eine Senkung der Energieschwelle für Radiomessungen um eine Gr ößenordnung erreicht werden, wodurch der Nachweis von PeV- Gammastrahlen aus dem Galaktischen Zentrum ermöglicht wird.

* Die erwartete Anzahl an PeV-Gammastrahlen, sowie der Anteil dieser Strahlung

der mit einem Radiodetektor am Südpol messbar wäre, wurde bestimmt. Außerdem wurde die Qualität der Gamma-Hadron Seperation ermittelt, welche nötig ist um diese Gammastrahlung zu detektieren. Damit wird die Sensitivität eines möglichen Radiodetektors für die Messung von Gammastrahlung aus dem Galaktischen Zentrum angegeben.

* Es wurde untersucht ob IceTop-der (Oberflächen) Teilchendetektor von IceCube- als Trigger für ein Radiodetektor genutzt werden kann. Hierzu wurde die Methode der konstanten Intensitäten verwendet, um die Energieschwelle von IceTop für die Erkennung von Luftschauern aus Richtung des Galaktischen Zentrums zu bestimmen. Es hat sich jedoch gezeigt, dass die Schwelle zu hoch ist um IceTop als externen Trigger für ein Radiodetektor im PeV-Bereich zu nutzen. Ein geplantes Szintillator Array als externer Trigger sowie ein selbst-getriggerter Radiodetektor werden als Alternative betrachtet, die allerdings einer weiteren Optimierung bedürfen.

Aufgrund der vielversprechenden Ergebnisse dieser Arbeit wird ein Oberflächen Radiodetektor für das IceCube Observatorium geplant. Im Zuge der laufenden Aktivitäten der IceTop-Erweiterung werden in einem ersten Schritt im antarktischen Sommer 2018/2019 zwei Prototyp-Antennen installiert.

Die im Rahmen dieser Arbeit entwickelte Frequenzoptimierung ist eine neue Technik, welche für alle Luftschauer-Radiodetektoren verwendet werden kann. Eine weitere Studie zeigt, dass dieses optimierte Frequenzband universell ist. Das zukünftige Radioexperiment zur Detektion von hochenergetischen Neutrinos und kosmischer Strahlung, GRAND, plant folglich auch ein optimiertes Frequenzband zu nutzen.

Contents

CHAPTER 1

Introduction

The mystery of the accelerators of cosmic nuclei in the Universe is a problem that has raised numerous questions for nearly a century, since the discovery of cosmic rays. With the help of space-based experiments, the supernova remnants have been identified as the major source of cosmic rays with energies up to 10^{14} eV. Although, there are some conjectures about the accelerators that produce cosmic rays beyond this energy range, it is still an unsolved puzzle. At PeV energies, the power law of the flux of cosmic rays changes from $E^{-2.7}$ to E^{-3} [1]. This is commonly referred to as the *knee*. It is expected that close to these energies, there is an overlap between the contribution of Galactic and extragalactic sources to the spectrum.

A concrete explanation to the knee structure is still not available. It is speculated that this is the maximum energy of the Galactic accelerators. Another explanation is the *Leaky box model* that states that particles of higher energy escape from the Galaxy, thereby softening the observed flux. To answer these questions, it is important to identify the sources of accelerators near to the knee, and study their internal processes.

Galactic PeVatrons, which are accelerators that can produce PeV energy particles, could solve the knee problem. That is, they could explain why we observe cosmic rays with PeV energies. A direct observation of these accelerators of cosmic rays can be performed by looking for neutrinos and gamma rays from these sources, since they will also be produced along with the cosmic rays. Several experiments have tried to employ various methods to search for these PeV-particle sources. The IceCube Neutrino Observatory has conducted several surveys for such sources using the stamps left by neutrinos or PeV gamma rays in the detector [2] [3] [4]. This resulted in the most stringent upper limits from several sources in the Galaxy.

The H.E.S.S. telescope in Namibia has reported the possible presence of a PeVatron at the Centre of the Milky Way [5]. This candidate PeVatron is close to the black hole of our Galaxy, Sagittarius A*. The diffuse gamma-ray spectrum within 10 parsecs surrounding this black hole was measured by H.E.S.S., which showed a spectrum with no cut-off at the measured energy range. The maximum energy of the measured spectrum extended to ≈ 80 TeV. An extrapolation of this spectrum to PeV energies is possible. Such a spectrum may imply that PeV gamma rays are produced by this PeVatron. If such PeV gamma rays are observed, this would directly imply that cosmic rays close to the knee are produced by this candidate accelerator.

The location of the IceCube Observatory [6] is ideal for Galactic Centre observations. Located at the South Pole, it has the Galactic Centre within its field of view

throughout the year. The Centre of the Milky Way is always located at a zenith angle of 61° at the South Pole. Hence, air showers from PeV gamma rays from the Galactic Centre will be inclined in nature at the South Pole. These showers will be nearly impossible to detect using IceTop, the existing surface array of IceCube, that detects particles from air showers. Inclined PeV showers have a low number of particles reaching the ground, and therefore will leave less signals on the IceTop array.

The technique of radio detection of air showers can instead be used for the detection of these PeV gamma ray showers. Unlike the particle contents, the radio signals from these showers will be able to reach the ground. Since it is an inclined shower, this will also leave a large radio footprint on the ground [7]. Therefore, a dense array of antennas (where antennas have a few tens of metres of spacing) is not required to measure these showers.

However, the challenge remains that PeV air showers have not been detected so far using the radio detection technique. Radio air shower experiments have successfully measured showers only above energies close to 40 PeV. This brings us to the critical point of devising a method to lower the energy threshold of radio detection of air showers. As a result of the findings of this thesis, a means to lower the energy threshold has been found. A significant challenge for this was to find a way to distinguish the radio signals from the measurable noise, which is especially difficult at PeV energies. Therefore the signal-to-noise ratio, a simple parameter that compares the signal to the noise, was studied within the scope of this thesis.

A description of gamma rays, their importance in solving the cosmic mystery, the details of the candidate PeVatron at the Galactic Centre observed by H.E.S.S., and the important aspects to be considered for the observation of PeV gamma rays are discussed in chapter 2. The thesis further moves on to a description of the IceCube Observatory and its surface component, IceTop. The measurement of air showers with IceTop, including the simulations and reconstruction scheme used for IceTop is described along with this in chapter 3. The future enhancement of IceTop is also discussed here. A general account of air showers, in particular the differences between gamma ray and cosmic ray showers is given in chapter 4. After a brief discussion of the general detection methods, a detailed description of radio detection of air showers and its mechanism is given. The common models used for radio emission and the existing radio air shower experiments are further described. The chapter then advances to a potential radio air shower array at the South Pole, and its scientific potential, including the detection of PeV gamma rays.

A detailed study of the contributions to the total noise that is usually influencing radio measurements is done in chapter 5. This is very important, since the detectability of PeV showers depends heavily on the noise conditions. Since the South Pole is relatively radio-quiet, man-made noise is omitted in this study. After understanding the noise conditions, the radio signals are studied in detail in chapter 6. With this, the signals are compared to the predicted noise levels. This is done for different frequency bands and ultimately culminates in a realisation of the optimal frequency band that enhances the signal-to-noise ratio. The chapter further studies the different shower parameters that can affect the shower, and how this influences the optimal band. Finally, the lowest energy threshold for radio detection that can be achieved at the South Pole conditions is arrived at.

With the successful determination of the method to improve the radio measure-

ments, the detectable flux of PeV gamma rays from the Galactic Centre is studied in chapter 7. This is used to then estimate the required gamma-hadron separation and thereby the sensitivity of the radio array. The final question to be answered is the trigger strategy of the radio array. External triggers with the help of particle detectors are used most commonly for the radio detection of air showers. The scope of this, along with the possibility of a self-triggered radio array is discussed in chapter 8. The results obtained in this thesis, along with the future studies that can be conducted are presented in chapter 9.

The results obtained from this thesis is applicable to the entire field of radio detection of air showers. A simulation study done for other experimental conditions, i.e. for GRAND and AERA experiments shows that the results obtained from this thesis is universally applicable. This is shown in Appendix C. The implementation of the frequency optimisation, performed as shown in this thesis, will improve the performance of future radio arrays. Based on the work of this thesis, both IceCube and GRAND plan to have frequency-optimised radio arrays that will show enhanced performance.

CHAPTER 2

The Science of Gamma Rays

Cosmic rays, gamma rays and neutrinos are commonly considered as the messengers of the high-energy Universe. The history of this field goes as far back as 1912 when Victor Hess discovered ionising radiation penetrating the Earth with the help of a balloon experiment. He found that the intensity of this radiation increased at higher altitudes in the atmosphere. These ionising particles were later called as cosmic rays. Today, we know that numerous *cosmic accelerators* exist in the universe, which act as sources of cosmic rays, gamma rays and neutrinos.

Cosmic rays are highly energetic charged particles produced by both galactic and extra-galactic sources in the universe. Supernova remnants are the most well known sources of cosmic rays. Other sources like active galactic nuclei or galactic mergers are also suspected to contribute to the wide spectrum of cosmic rays. Cosmic rays are composed of atomic nuclei, from the lighter protons all the way up to the heavier iron nuclei. Since they are charged particles, they are largely deflected by the magnetic fields in space, depending on their rigidity. This results in a loss of information of the source which directly produced the observed cosmic rays (except at extremely high energies where the bending radius of the cosmic-ray particle in the magnetic field becomes very large when compared to its distance of propagation).

Gamma rays and neutrinos, on the other hand, are neutral particles and are hence unaffected by inter-galactic magnetic fields. Thus, they help us in pointing back to their origin. Gamma rays are produced in a variety of processes occurring within and near to the sources. They are sometimes produced in *leptonic* processes that involve accelerated electrons, and sometimes through the interaction of cosmic rays in the media within or surrounding the source. Therefore the observation of gamma rays can indicate the presence of both electromagnetic as well as hadronic interactions in the source. Neutrinos, on the other hand are produced only in the presence of hadronic processes within the source. Therefore, they are direct indicators of such interactions. Therefore, observed energy spectrum of gamma rays and neutrinos can indicate the processes occurring within the source itself. This in turn shows the acceleration processes within the source and the maximum energy up to which it can accelerate particles. Since gamma rays and neutrinos are produced along with cosmic rays, they act as a smoking gun to the presence of the accelerators that produce cosmic rays.

2.1 Observation of gamma rays

The high energy gamma-ray sky has been studied extensively in the past few decades using various telescopes. The gamma-ray flux goes down with energy (normally with an E^{-2} behaviour). Due to this, the low energy gamma rays can be observed with smaller-sized detectors and still provide enough statistics. Space-based telescopes are normally used for the observation of low energy gamma rays. Some examples are: Fermi-LAT (20 MeV to more than 300 GeV) [8], Agile (30 MeV–50 GeV gamma rays and hard X-rays in the 18–60 keV band) [9] and Swift (a Burst Alert Telescope for the 15–150 keV band, an X-Ray Telescope for in the 0.3–10.0 keV band, and a UV and Optical Telescope for the 170–600 nm range) [10].

Gamma rays with energies ranging to a few TeV is out of the scope of space-based experiments. This is due to the lower flux of gamma rays of these energies, which in turn requires larger observatories to increase the exposure. Therefore, for gamma-ray observations in the energy range of hundreds of GeV to hundreds of TeV, ground-based experiments are used. These experiments tap into the air showers produced by these TeV gamma rays to observe them. More about air showers is given in chapter 4 in section 4.1.

H.E.S.S. (High Energy Stereoscopic System) [11], VERITAS (Very Energetic Radiation Imaging Telescope Array System) [12], and MAGIC (Major Atmospheric Gamma-ray Imaging Cherenkov) [13] are ground-based telescopes that measure the air-Cherenkov emission from the gamma-ray showers produced in the atmosphere. These telescopes can measure gamma rays with energies of tens of GeV to nearly a hundred TeV. The Cherenkov Telescope Array (CTA) is a next generation detector that will use this technique, and is planned to have a larger area on the ground and a better performance than the existing experiments using the imaging air-Cherenkov technique [14]. Certain experiments rely on the measurement of the particles reaching the ground from the gamma-ray induced showers. They measure the particles reaching the ground and their interaction with the detector medium. Some examples are HAWC (High-Altitude Water Cherenkov Observatory) [15] and MILAGRO [16]. LHAASO [17] is the planned next generation extensive air shower experiment that plans on the detection of gamma rays using the same method as experiments like HAWC, MILAGRO. The Southern Gamma-ray Survey Observatory Alliance (SGSO) is an effort to have an extensive air shower detector located at South America, that can measure astrophysical gamma rays and cosmic rays in the energy range between 100 GeV and 100 TeV. The concept and design of such an experiment is currently under discussion [18]. The sensitivity of some of these ground-based experiments to a Crab-like source (source with a spectral index of ~ 2.4) is given in Figure 2.1.

As mentioned earlier, the flux of very high energy gamma rays is relatively lower than GeV-TeV energy gamma rays, mainly due to its inevitable absorption during its travel from the source to the observer. For this reason, gamma rays of very high energies are limited to those originating from within our Galaxy. At distances greater than the size of our Galaxy, the very high energy gamma-ray sky is mainly opaque.

Very high energy gamma rays are of particular interest since the detection of these can be directly correlated to the the cosmic rays at the knee. That is, it is of particular interest to search for PeVatrons in our galaxy which may accelerate

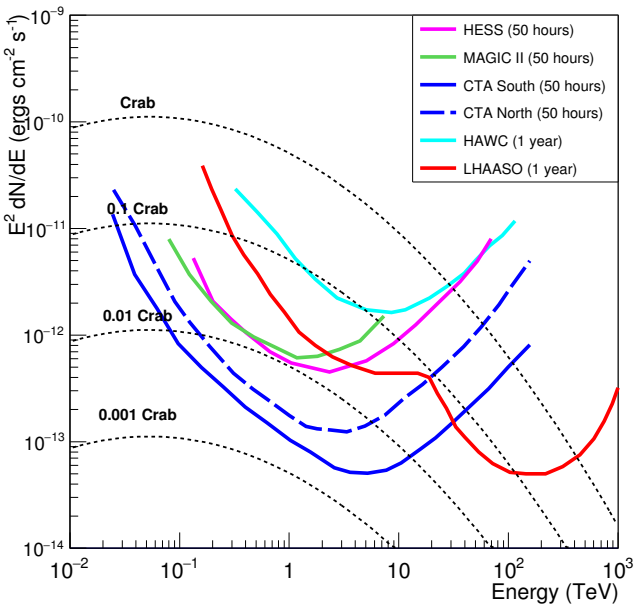

Figure 2.1: The differential sensitivity of various experiments to a source like Crab Nebula. Also shown are the spectra for Crab, 0.1 Crab, 0.01 Crab, and 0.001 Crab. The figure is from [17].

particles to several tens of PeV. These will consequently produce gamma rays and neutrinos with energies in the PeV range ($E_{\gamma,\nu} \approx E_{CR}/10$). Hence, the detection of such PeV gamma rays will directly point to sources of PeVatrons in our galaxy. The detection of such PeV gamma rays will require sensitive instruments of sufficiently large area of coverage, since the incoming flux of these PeV gamma rays will be very low.

Gamma rays with energies lower than 30 TeV can easily propagate through the intergalactic and intragalactic media. Most of the gamma-ray observatories operate in this energy regime. Gamma rays with larger energies are heavily attenuated in the galactic and extragalactic media. This is due to the rising interaction cross section for the di-electron creation through photon-photon interaction ($\gamma\gamma \rightarrow e^+e^-$). This process occurs due to the radiation that exist in space. That is, the gamma ray propagating through space interacts with the sea of photons in the galactic and intergalactic media, causing a large fraction of the gamma rays to be absorbed.

A major part of this radiation is the Cosmic Microwave Background (CMB). The CMB is the medium of photons remaining from the Big Bang (relic radiation). This radiation is seen to have a black body spectrum with a mean temperature of T = 2.73 K. The CMB photons have a number density of approximately 410 cm^{-3}. The threshold energy for this pair production process is around 3 TeV. The cross section rises significantly with energy and peaks at PeV energies, thereby being the major source of attenuation for PeV gamma rays.

Another contribution to the background radiation comes from the Galactic dust emission (IR emission). This emission has the largest effect on photons with a few TeV energy and thereafter the cross section declines. Apart from this, the Extra Galactic Background Light (EBL) interacts with gamma rays traversing the inter-

galactic space. This radiation field is very complicated to describe. Nevertheless, since its number density is only around 1.5 cm^{-3}, this effect can be safely neglected, in comparison to the attenuation contribution from CMB [19].

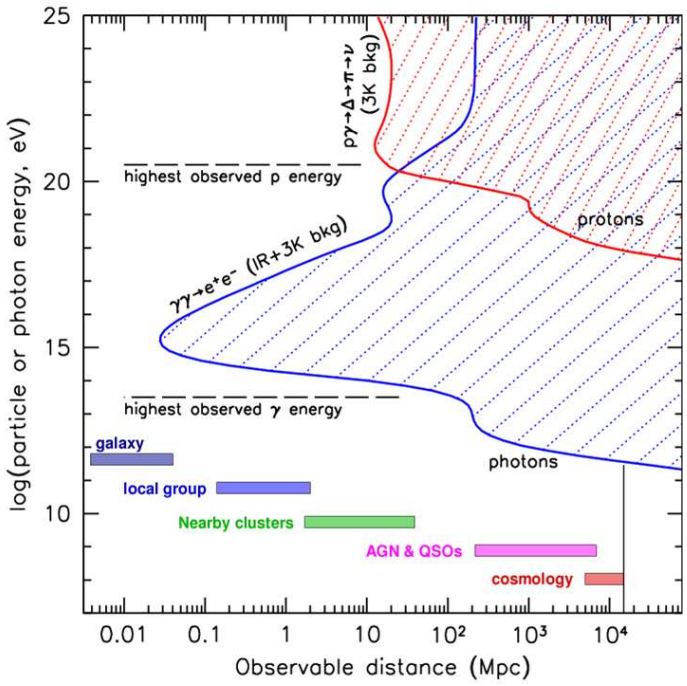

Figure 2.2: The maximum observable distances for gamma rays and protons, for each energy range. PeV energy gamma rays can travel a maximum distance of the size of the Galaxy. The figure is from [20].

Figure 2.2 shows the distances up to which gamma rays of different energies can be observed. Also shown are the common observable sources at different distances. At energies lower than 10^{11} eV, gamma rays can be observed from very large distances. The figure shows that attenuation starts occurring for energies larger than this. It can be seen that at PeV energies, only gamma rays within the Galaxy can be observed by us. At energies larger than this, there could be a revival, but such high energy gamma rays are not observed. This could be due to the limitation of the local sources, as they run out of enough energy. The observable distances for protons are also shown in the figure. Protons start getting absorbed by the CMB only at energies larger than $10^{19.5}$ eV. This is commonly known as the GZK suppression. This occurs through the processes $\gamma_{\mathrm{CMB}} + p \rightarrow \Delta^{+} \rightarrow p + \pi^{0}$ and $\gamma_{\mathrm{CMB}} + p \rightarrow \Delta^{+} \rightarrow n + \pi^{+}$. The resulting pions decay into either photons or neutrinos. The Pierre Auger Observatory attempts to measure the photons produced by the GZK process [21], while several extremely high energy neutrino experiments like IceCube-Gen2 [22], GRAND [23], ARA [24], etc. aim at measuring GZK neutrinos.

Figure 2.3 shows the probability of gamma rays surviving the absorption and arriving at the observer location for different energies (model generated by Silvia Vernetto and Paulo Lipari [19]). Shown is the level of absorption for gamma rays travelling from the Galactic Centre to the sun. As described above, at energies up to tens of TeV, the dominant source of absorption is the dust radiation, and at PeV energies, the absorption is due to the CMB. The survival probability is the least (0.3) at 2 PeV. As shown in the inset, the contribution from EBL and other sources is

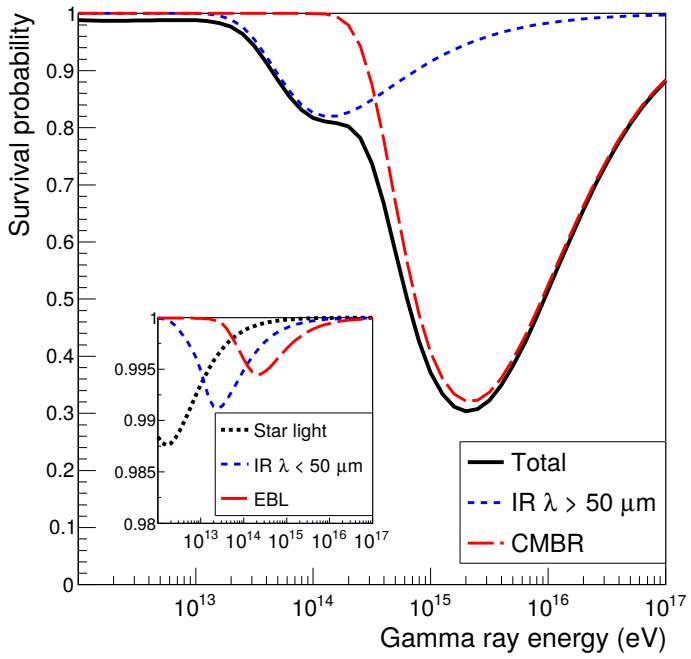

Figure 2.3: The survival probability of gamma rays after interacting with the photons in its path. At PeV energies, the major absorption is due to the CMB photons. At energies close to a hundred TeV, the IR dust contributes the most to the absorption. Figure from [19].

relatively low.

Several attempts have been made by various experiments to detect gamma rays of PeV energies, since they would potentially explain the knee structure of cosmic rays. Although there has been no successful detection of PeV gamma rays yet, upper limits at various energies have been established by different experiments. Figure 2.4 shows some of the diffuse upper limits obtained from different experiments. The left panel shows the upper limit to the isotropic diffuse flux obtained with the KASCADE-Grande experiment [25]. These upper limits were used for constraining the distance of the possible sources for the IceCube neutrino excess. The right panel in the figure shows the upper limit to the diffuse gamma-ray flux from the Galactic Plane that is obtained with the 86 string version of IceCube (IC86)[26]. These limits are compared to the limits from the Galactic Plane obtained with CASA-MIA. In addition to this, surveys for point sources of PeV gamma rays from the Galactic Plane have been done by IceCube. These surveys also predict strong PeV gamma ray upper limits to various H.E.S.S. sources in the field of view of IceCube [4].

2.2 The Galactic Centre: a PeVatron?

It is already established from Fermi-LAT observations that the major source of cosmic rays with energies up to nearly 10 TeV are supernova remnants [27]. It is also anticipated that these supernova remnants produce cosmic rays up to the knee. However, the sources producing cosmic rays with energies greater than this (PeV range) are yet to be discovered. The search for the origin of cosmic rays with PeV energies has been going on for decades. It is expected that such sources exist within

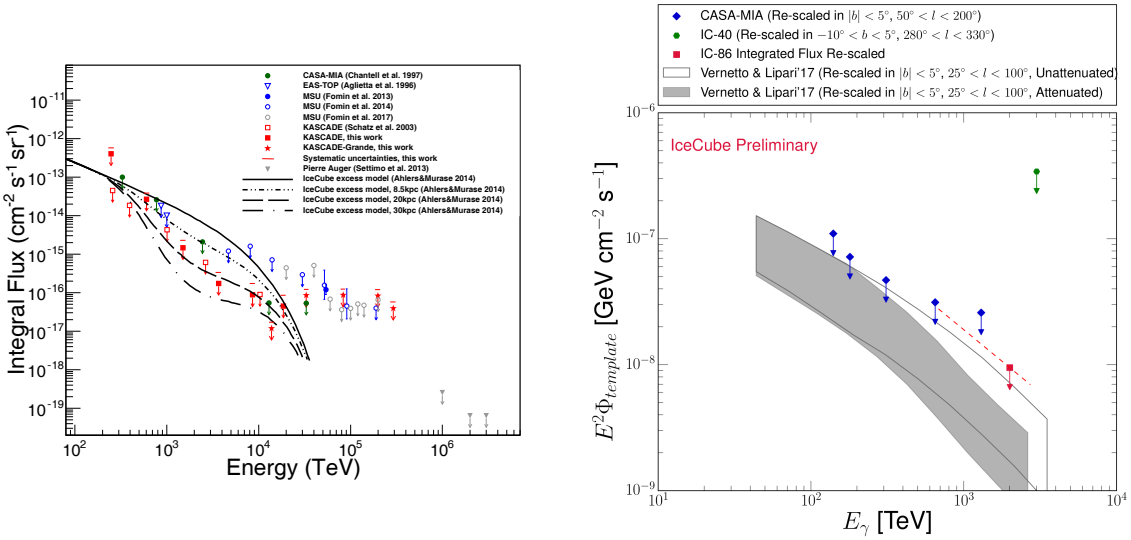

Figure 2.4: Gamma ray upper limits from KASCADE-Grande (isotropic diffuse flux [25]) and IceCube (diffuse Galactic Plane emission [26]).

our Galaxy itself. The ideal way to search for such sources are through the gamma ray and neutrino signatures from these sources. Such accelerators that can produce highly energetic particles with energies in the PeV range are commonly known as *PeVatrons*.

Recently, the High Energy Stereoscopic System (H.E.S.S.) has reported the presence of a plausible PeVatron at the centre of the Milky Way [5]. The telescope measured the region surrounding the Galactic Centre to find very high energy gamma rays within the central 10 parsecs. The location of the emission region is close to the super-massive black hole, Sagittarius A* (Sgr A*), at the centre of the Milky Way. A possible linkage between the proposed PeVatron and Sgr A* cannot be ignored. Such a PeVatron could be an alternative to the standard picture of supernova remnants that are considered as accelerators of PeV cosmic rays [5].

The diffuse gamma-ray spectrum that was observed by H.E.S.S. extends to energies up to around 80 TeV. The annular region around the Galactic Centre that was used for obtaining this spectrum is shown in the top panel of Figure 2.5 [5]. The region bordered with black in the zoomed in version shows this annulus around Sgr A*. It was found that the data follows a spectral shape that has a spectral index of ≈ 2.32, and extends to energies up to tens of TeV. It was also seen that the spectrum prefers no cut-off or break within this energy range. It was also found that a fit of the spectrum with a cut-off energy at 2.9 PeV, 0.6 PeV and 0.4 PeV deviated from the data with confidence levels of 68%, 90% and 95% respectively [5].

The PeVatron at the Galactic Centre was seen to be co-located with an unidentified source, HESS J1745290, in the same region. Nevertheless, there was no concrete evidence of an intrinsic link between the two sources. It is postulated that the HESS J1745290 source could have experienced a cut-off due to absorption by the IR radiation in this region [5]. From Figure 2.3 it can be seen that this is indeed the energy range where IR absorption is dominant.

Figure 2.5 shows this spectrum measured by H.E.S.S. in its bottom panel [5]. The red curve (exaggerated 10 times for ease of visibility) shows the diffuse flux

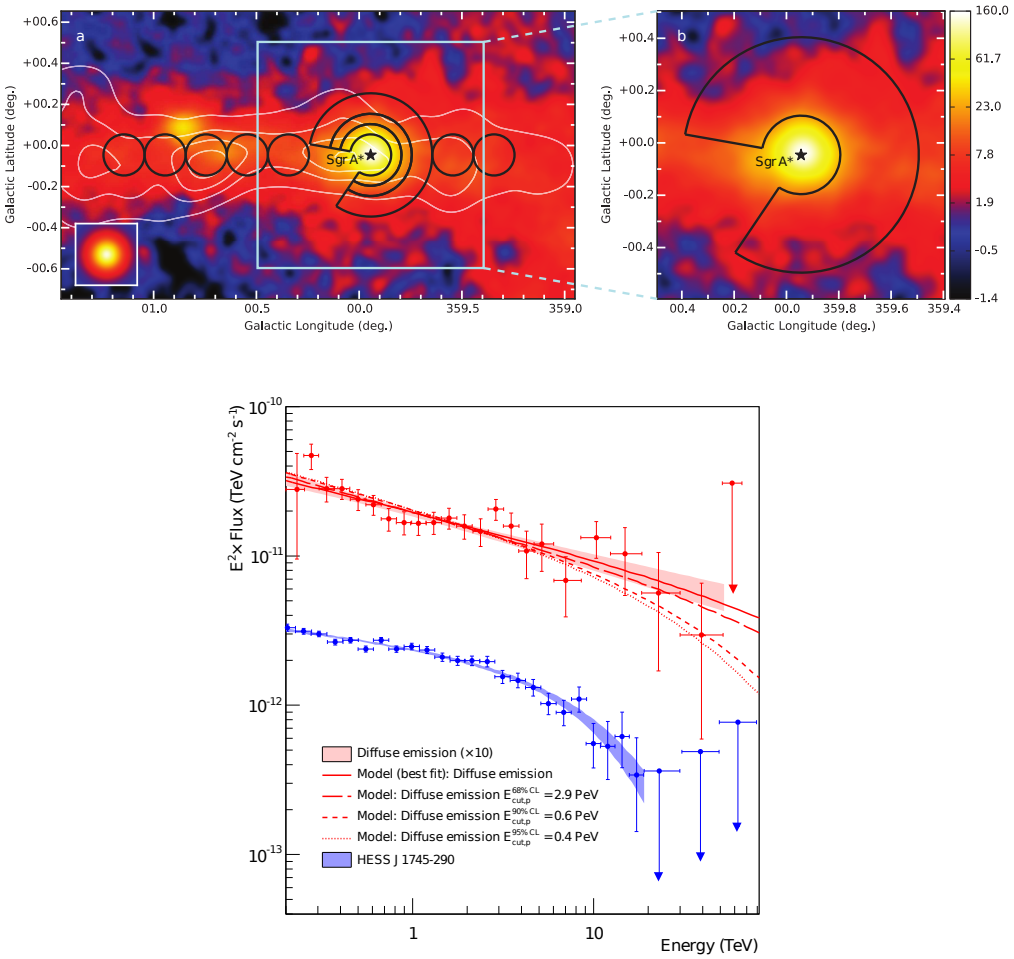

Figure 2.5: Observations of the Galactic Centre by H.E.S.S. is given in the top two panels. The observed counts in each pixel is given by the colour scale. The right panel shows the zoomed in part near to the black hole. The contour in this panel shows the region used to calculate the diffuse flux. The bottom panel shows the measured spectrum by H.E.S.S. The diffuse flux (times 10) is given by the red dots, along with the fits performed on this data. The blue dots show the spectrum followed by HESS J1745290, which has a clear cut-off at 10 TeV [5].

that is measured near to the Galactic Centre. The figure shows that the best fit is a spectrum with no cut-off. Also shown are the fits for cut-off at 2.9 PeV, 0.6 PeV and 0.4 PeV. The spectrum obtained for HESS J1745290 is also shown by the blue data points. This spectrum has a clear cut-off at 10 TeV and a spectral index of 2.14 [5].

On scrutinising this spectrum, one can speculate if this gamma-ray spectrum of the PeVatron extends up to PeV energies. That is, if the accelerator is energetic enough to produce gamma rays with PeV energies, or not. At PeV energies, the flux could be so low that H.E.S.S. itself cannot measure it due to its low duty cycle and smaller area on the ground. Therefore, we require better methods to look for PeV gamma rays from the Galactic Centre.

The IceCube Neutrino Observatory, at the South Pole is at an advantageous position for observing the Galactic Centre. The centre of the Milky Way is visible throughout the year at this location. This gives a chance for having a continuous

observation of the Galactic Centre. Due to the existing experimental setup of IceCube, it becomes easier to have add-ons to enable the observation of PeV gamma rays from the Galactic Centre. Details of the IceCube Observatory is given in the following chapter.

CHAPTER 3

The IceCube Observatory

The IceCube Neutrino Observatory is located at the geographic South Pole. This detector has been designed to measure atmospheric and astrophysical neutrinos in the energy range of several tens of TeV to a few PeV [6]. It has been successful in detecting neutrinos of astrophysical origin with the highest energies measured so far. The detector has been operational since the year 2007.

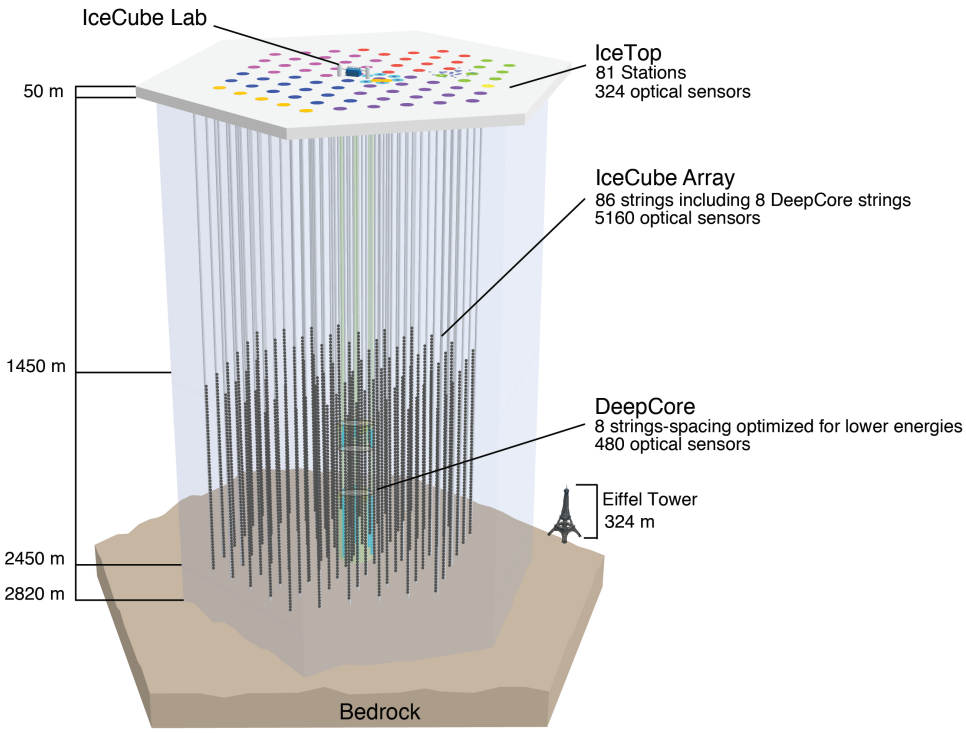

Figure 3.1: An illustration of the IceCube detector, with an overall volume of 1 km^3. For comparison, the Eiffel tower is also shown in the figure. The image is shown in [28].

A schematic of the 3-dimensional IceCube detector array is given in Figure 3.1. The detector consists of 86 strings that are drilled into ice. The strings are loaded with digital optical modules (DOM) that are used to collect the Cherenkov light emitted when a charged particle (muon, electron or tau) is produced through the

interaction of a neutrino in ice [29]. Along with this, other through-going charged particles (mainly muons) from air showers also produce Cherenkov light inside the ice, which can be detected by the DOMs. The strings have an average spacing of 125 m. Of these, 8 strings at the centre are closely spaced with a mean spacing of 70 m (DeepCore) [30]. The main in-ice detector starts at 1450 m from the surface and extends down to 1 km [6]. The DeepCore, on the other hand extends only between 2100 m and 2450 m below the surface of the ice, with optical modules that are more densely packed (7 m spacing) than the main IceCube strings (17 m). On the surface of the ice, there is also an array of cosmic-ray detectors, called IceTop. They measure air showers from these cosmic rays and can therefore act as a veto for the in-ice detectors [28]. The next section discusses IceTop in further detail.

3.1 IceTop

The IceTop array consists of 81 stations of ice-Cherenkov tanks. Each station is made up of 2 such tanks. The location of each station is near a hole of an IceCube string (except for station 81). These stations have an average spacing of 125 m. There is also an in-fill array of stations with smaller spacing ($\approx$ 70 m distance). These infill stations are located close to the IceCube Lab (ICL), where all the data is centrally collected. The whole array has an area of 1 km^2 [28]. The image of a station and the schematic of the IceTop array is shown in Figure 3.2.

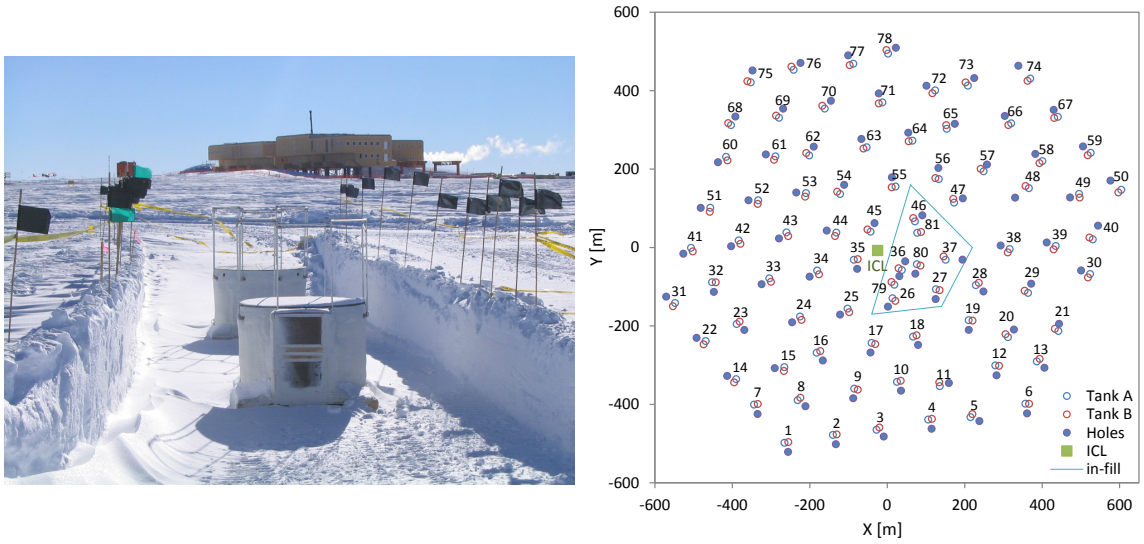

Figure 3.2: The left panel shows one of the IceTop stations, with its two tanks (from [31]). The right panel shows the array geometry of IceTop (from [28]). The blue dots show the positions of the IceCube strings and the open circles show the tank positions. The in-fill stations are also marked.

Each tank in a station contains two optical modules: one high-gain and one low-gain module. Each DOM consists of a Hamamatsu photomultiplier tube and its electronic board. This module collects the Cherenkov light that is produced in the tank when a charged particle passes through it. On collecting light from multiple tanks within a given time window, one can say that an air shower has been detected. The tanks are 6 mm thick, have a height of 1.1 m and have an inner diameter of

1.82 m. These tanks are made with cross-linked polyethylene and are filled with frozen water up to a height of 0.9 m. Out of the 162 tanks, 150 have a reflective coating of zirconia inside them. The rest of the tanks are lined with Tyvek [28].

The signals collected by the DOMs are converted into the units of *vertical equivalent muon* (VEM). This is the charge deposited by a single muon that is oriented vertically, in the tank. When the DOM measures a signal, it is considered as a *hit*. For the high-gain DOM, the threshold above which the signal is measured corresponds to 20 mV and for the low-gain DOM, this is 4 mV. When both the tanks in a station have registered a hit, it is called a *Hard Local Coincidence* condition and the resulting hits are called HLC hits. If there is only one tank in a station that has a hit, this is called the *Soft Local Coincidence* (with SLC hits) [28].

The IceTop array is triggered when there are 6 HLC hits registered in the entire array. This corresponds to 3 stations. Such a condition is imposed to reduce the amount of noise that would be otherwise mistaken as hits from an air shower. This three-station condition has an energy threshold of about 300 TeV for an air shower. If three stations within the infill are triggered, air showers with energy as low as 100 TeV can be detected.

IceTop, along with the in-ice detectors of IceCube provides with a 3-dimensional detector setup that can measure cosmic rays air showers. while the surface component measures the electromagnetic and the low energy muons (GeV range) produced in the air shower, the highly energetic (TeV range), forward-directed muons produced in bundles during the first interaction of the air shower can be measured by the in-ice part. This unique measurement can help in the study of hadronic interactions. IceTop acts as a veto for the in-ice neutrino detector. If a track that is measured by the in-ice detector is accompanied by air shower signatures on IceTop, this event is considered rejected by IceCube for neutrino analysis (as they will be muons produced in the air showers). IceTop acts as a veto from energies starting from 300 TeV. To conduct studies of the properties of air showers, IceTop selects events with a higher energy. These events fall within the energy range of $10^{15} - 10^{17}$ eV. IceTop also acts as a gamma ray telescope, since it is located at an elevation of 2835 m above sea level, which is close to the shower maximum for air showers within the energy range of measurement. Further details of this is given in section 3.3.

The cosmic ray energy spectrum that is measured by IceTop for 3 years of data (June 2010-May 2013) is shown in Figure 3.3. The figure also shows the spectrum obtained for a sub-sample of the events that were observed by both IceTop and IceCube in coincidence [32].

3.1.1 Snow accumulation

The ambient condition at the Pole affects the measurements made by the detector array. At the South Pole, there is an increasing coverage of snow on top of the detectors. This snow accumulates upon drifting from 20 degrees northeast towards the array. An average of 20 cm of snow is accumulated on top of the detectors each year [33]. By 2016, some of the IceTop tanks have been covered by 2.5 m of snow. The amount of snow on top of the detector array in the years 2010 and 2016 is shown in Figure 3.4. Due to this snow accumulation, the signal received by the tanks are attenuated. This mainly affects the electromagnetic components of the

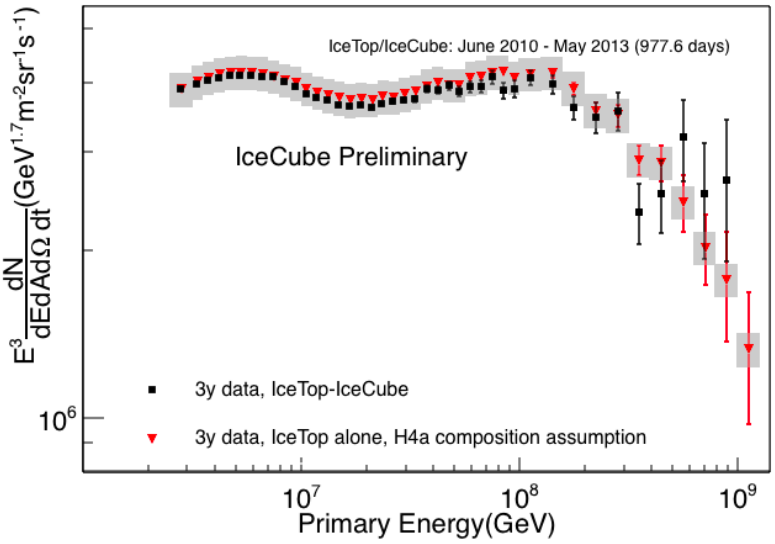

Figure 3.3: The cosmic-ray spectrum obtained from 3 years of IceTop data is shown by the black squares. Also shown is the spectrum obtained by IceTop and IceCube coincident analysis (red triangles). The grey shaded region shows the systematic errors. The plot is published in [32]

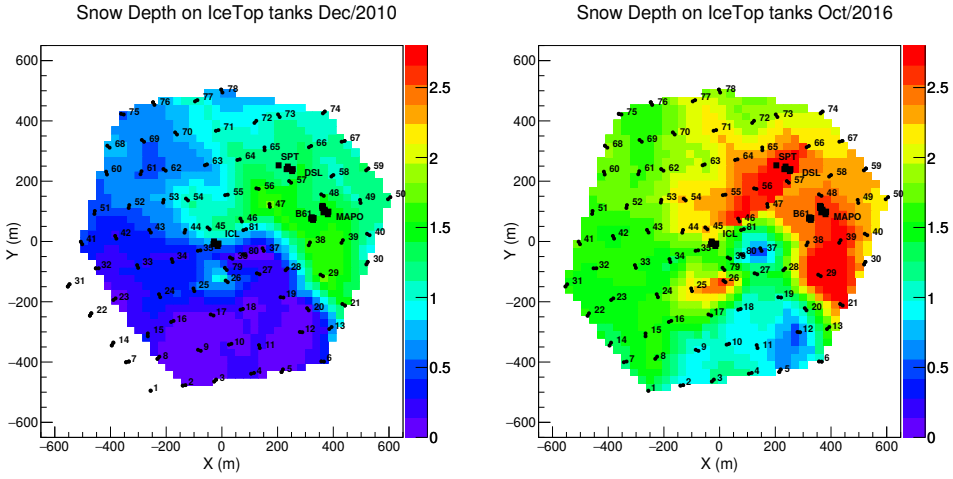

Figure 3.4: The snow that is accumulated on top of the IceTop tanks in the years 2010 and 2016. The snow increases by an average of 20 cm per year. Modified from [33] (credits: IceCube collaboration).

shower. The muons pass unhindered through the snow and are detected by the tanks. This introduces an uncertainty in the calibration of S_{125} vs energy (see section 3.1.2). This snow accumulation is also increasing the energy threshold of air-shower detection every year.

3.1.2 Simulation and reconstruction of air showers

The IceTop simulation scheme uses air showers that are produced with CORSIKA [34]. These showers are simulated using FLUKA [35] and SIBYLL-2.1 [36] as the low and high energy hadronic interaction models respectively. The showers simulated

in this manner are then passed through a software framework that is developed exclusively for IceCube. This IceCube software utilises GEANT4 [37] in order to implement the response of the IceTop tanks into the simulation [28]. Information of the snow that is measured on top of each tank, at the South Pole, is also included in the simulations. Thereby, the attenuation of signals due to snow accumulation is properly taken into account in the simulations.

The reconstruction scheme of IceTop has been developed with the help of the showers simulated in the above manner. The reconstruction scheme within the software framework separates the signals into HLC and SLC pulses (based on the information of the number of tanks in a station that have successfully registered a hit), and also performs a time and charge calibration of the signals. Once this is done, the signals are available in units of VEM. The software then applies a likelihood-based regression for obtaining a fit to the lateral distribution of the shower. The lateral distribution function of IceTop describes the shower size at different distances from the shower axis. The shower size at a distance of 125 m from the shower axis is used as a standard variable, within the scope of IceTop, that is used to determine the energy of the primary particle that produces the air shower. This shower-size parameter is called S_{125} and has been calibrated for different energy ranges. This is done for showers with a zenith angle range of $0° - 36°$. The reconstruction also determines the position of the core and the zenith and azimuth angles of the air shower. These parameters are finally used for the analysis of all the simulated and measured data of IceTop [28].

3.2 The IceTop enhancement

As discussed in section 3.1.1 the IceTop array is covered by snow increasingly, every year. An enhancement of IceTop is envisioned in order to revive the electromagnetic components of the air shower that are lost due to the snow accumulation. For this, a homogeneous array of scintillators are planned to be deployed within the same area as that of the IceTop tanks. The current discussion foresees an array of scintillators consisting of 37 stations, with each station formed with 7 scintillators [38]. This array is expected to lower the energy threshold to hundreds of TeV [39].

Currently, there are two stations with 7 scintillators each, that are co-located, at the South Pole. These two stations have two different data-acquisition systems and are used for prototype measurements and for optimisation of the setup in the conditions at the Pole [38]. A schematic of the planned array of scintillators and the prototype detectors at the Pole are shown in Figure 3.5.

Along with the scintillator array, prototype tests of imaging air-Cherenkov telescopes are also ongoing. These telescopes, called IceAct, are also built for the detection of air showers. They consist of SiPM-based cameras that can measure the Cherenkov light in the atmosphere, produced by an air shower. Currently, there are two IceAct telescopes at the Pole, that are used for optimisation and for test measurements. Even though they have a low duty cycle, these telescopes are expected to measure air showers with an energy of lower tens of TeV [40].

The scintillator and air-Cherenkov detectors for the enhancement of IceTop are considered as forerunners to a future large-scale surface array, that will act as a veto array for IceCube-Gen2. IceCube-Gen2 is the planned extension of IceCube that aims at the measurement of high energy neutrinos from the southern sky. It is expected to

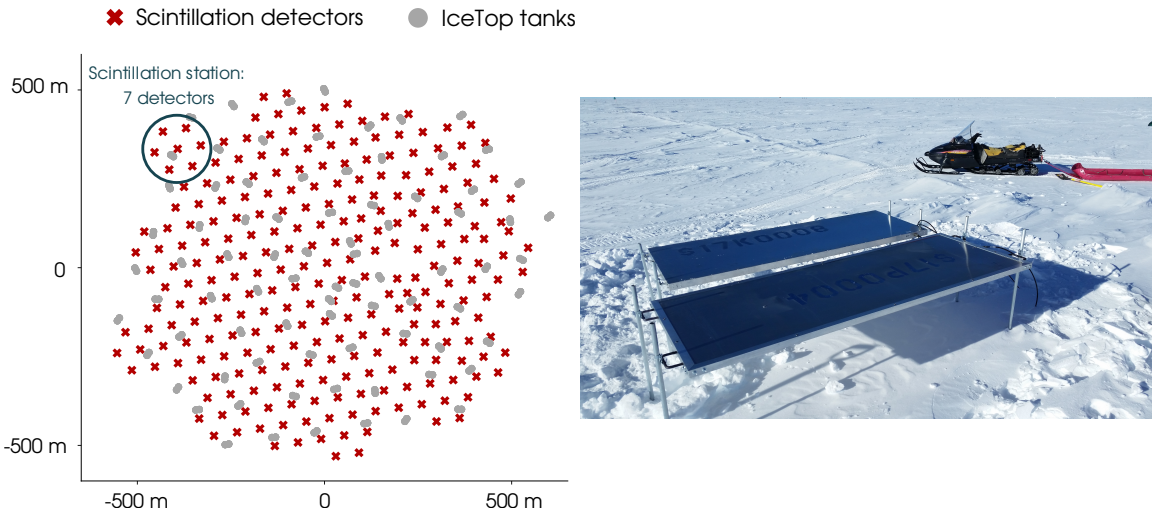

Figure 3.5: The current version of the array design of the scintillators, that is implemented in the simulations, is given in the left panel. The red crosses are the scintillators and the grey dots are the existing IceTop tanks [39]. The right panel shows two of the prototype scintillators at the South Pole (credits: IceCube collaboration).

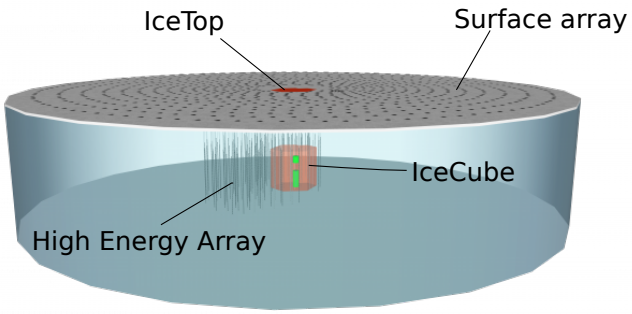

Figure 3.6: A schematic of IceCube-Gen2 along with a possible large-scale surface array. The figure is adapted from [41].

have a volume of 10 km^3, i.e. 10 times that of IceCube. A large surface array with an area of around 75 km^2 is also under discussion as a part of IceCube-Gen2 [41] [42]. The current surface enhancement therefore helps in the R&D work for the future array. An idea for an in-ice radio array, as a part of IceCube-Gen2, that can detect neutrinos with energies of $10^{16} - 10^{18}$ eV also exist (Gen2-radio) [22]. A schematic view of a possible next generation detector, IceCube-Gen2, is given in Figure 3.6.

The enhancement of IceTop with scintillators provides with an ideal time window to consider additional radio antennas along with these detectors. This will enable us to have a hybrid detector setup at the South Pole, that can be used for improved air-shower measurements. We can also benefit from sharing the data acquisition, that will reduce the costs considerably. Details of the prospects of such an antenna array is given in section 4.5 of chapter 4.

3.3 The hunt for PeVatrons with IceCube

Several efforts to identify Galactic PeVatrons with IceCube already exist. One method involves the measurement of the neutrino fluxes from possible sources in the northern sky. The results published in [2] claim that IceCube could help in identifying the sources in the Milagro sky map to be PeVatrons or not, with sufficient data. Another method to search for PeVatrons with IceCube is to look for the muons generated in gamma-ray showers, which starts occurring for showers with an energy of a few hundreds of TeV. This can be performed in the southern sky with IceCube. It may be possible to distinguish these events from the background cosmic rays for a sufficiently bright gamma-ray source [3]. The definition of a PeVatron for these searches is different from that in this thesis. The above searches define PeVatrons as those sources producing charged cosmic rays of PeV energies. On the other hand, this thesis defines PeVatrons as sources that are energetic enough to produce PeV gamma rays (and therefore cosmic rays up to nearly 10 PeV), as mentioned in section 2.2.

The above-mentioned PeVatron searches with IceCube aim at explaining the contribution of such PeVatrons to the knee of the cosmic-ray spectrum. It was also mentioned in the previous chapter that IceCube also searches for sources of PeV gamma rays from the Galactic Plane, using the known catalogue of gamma-ray sources from H.E.S.S. A positive discovery of such sources will also reveal PeVatrons in our Galaxy. Currently, there are upper limits to such possible sources within the field of view of IceCube (zenith angle $< 37°$) [4].

Observing PeVatrons in the southern sky using the above mentioned methods used by IceCube will restrict the visible sky to that within the nearly-vertical zenith angle range. This cannot be overcome due to limitations in the detector volume. Hence, Galactic Centre observations with the help of down-going muons or with other existing gamma-ray analyses is restricted, since it is visible at a zenith angle of $61°$ from the South Pole. Using a surface radio array that is integrated with IceCube can overcome this drawback and enable us to search for PeV gamma rays from the Galactic Centre, due to the larger field of view of radio arrays. Further details of this are given in section 4.5 of the following chapter.

CHAPTER 4

The Radio Detection Technique

This chapter describes the general physics of extensive air showers in section 4.1 and moves on to make comparison between air showers produced by cosmic rays and gamma rays. The chapter further moves onto the detection methods of air showers. In particular, we concentrate on radio detection: its emission mechanism, its properties, modelling of radio emission, and experiments that use this technique. The focus is finally moved onto a future radio air-shower array at the South Pole, which is the main topic of this thesis.

4.1 Extensive air showers

Cosmic rays and gamma rays, upon entering the Earth, interact with its atmosphere and produce an avalanche of particles - called extensive air showers. The primary particle interacts with the elements in the atmosphere and produces secondary particles, which will further interact to produce more particles. This process recurs resulting in a cascade of particles that can be measured on the ground.

The secondary particles consist of electromagnetic components like electrons, positrons and photons; hadronic particles like protons, neutrons, pions, kaons, and other nuclear fragments; and muons along with their corresponding neutrinos and anti-neutrinos. The muons and other hadronic particles result from the hadronic interactions of the primary and secondary particles with the hadrons in the Earth's atmosphere. A majority of the charged pions and kaons that result from such interactions are short lived and therefore do not reach the ground. Instead, they decay into muons and neutrinos, which then arrive at the ground. The neutral pions, on the other hand, decay into two photons and contribute to the electromagnetic part of the shower. Protons, neutrons, and the high-energy pions that are produced in such hadronic interactions will further interact with the atmosphere to produce other hadrons. The different components of an air shower are given in Figure 4.1.

The electromagnetic components are mainly fed through interactions like bremsstrahlung where the charged electron loses energy and releases a photon, and pair production where photons annihilate to produce electrons and positrons. These processes repeat for large distances, thereby increasing the number of electromagnetic particles in the shower. Such an increment in the number of particles occurs until a critical energy is reached, after which no further particles are produced. This region in the shower has the maximum number of particles and is

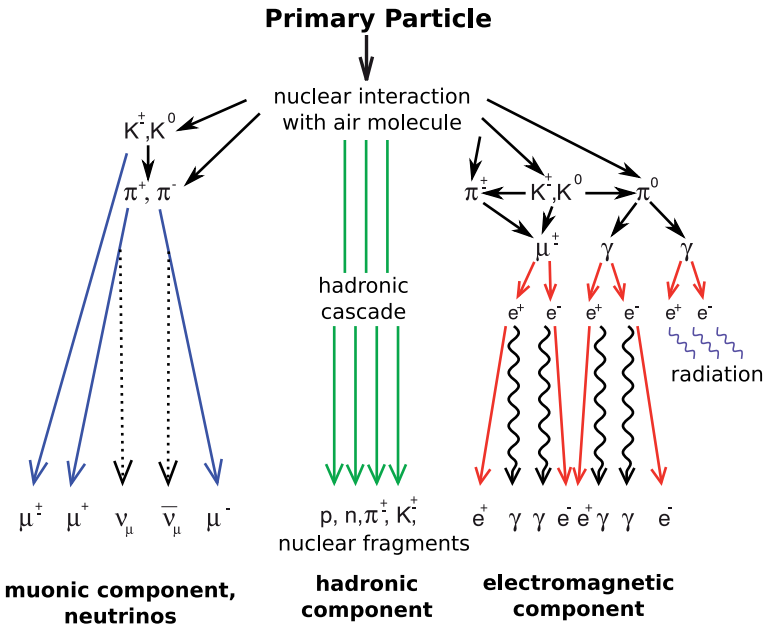

Figure 4.1: The particles that are produced in an air shower can be grouped into muonic, hadronic and electromagnetic components. The illustration is adapted from [43].

therefore called the shower maximum. Beyond this, as the shower proceeds, the number of particles along its longitudinal length decreases. This is due to the loss of energy suffered by the lower energy particles as they move further through the atmosphere. The electromagnetic component constitutes the major particle population within the air shower and thereby represents 90% of the energy of the primary particle.

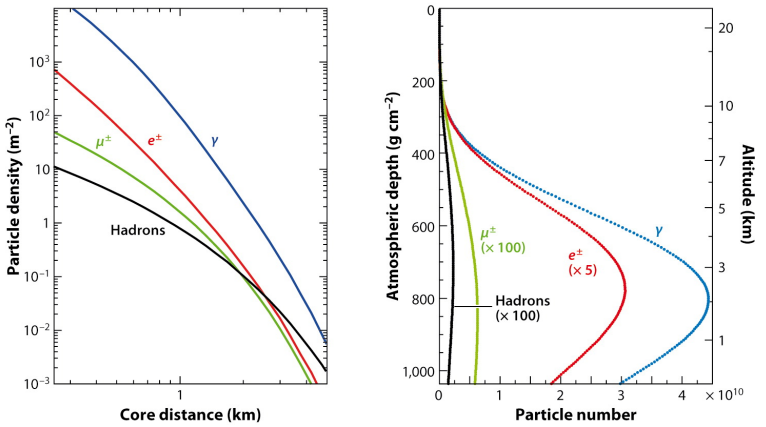

Figure 4.2: The lateral (left) and longitudinal (right) distribution of different particles in a proton shower of energy 10^{19} eV. The figure is adapted from [44].

The propagation of the electromagnetic components in the air shower can be represented using the model proposed by Heitler [46]. This model can in general be extended to hadronic showers also. The Heitler model describes the different stages of the air shower. Within this model, each electromagnetic particle of a shower undergoes an interaction and thereby divides into two other particles. These next

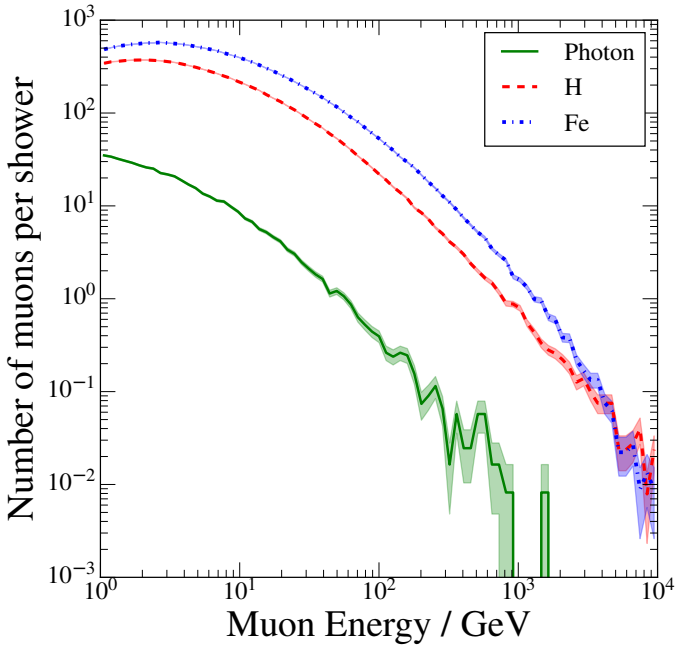

Figure 4.3: The spectra of muons for gamma ray, proton, and iron showers of 1 PeV energy simulated with CORSIKA showers using SIBYLL 2.1. The figure is from [45].

generation particles are assumed to share the energy between them equally. The length for which the particle moves freely before collision is represented by λ. After n generations of processes for an atmospheric depth of X, the number of particles will be

$$N = 2^n = 2^{(X/\lambda)} \tag{4.1}$$

and the energy of each particle in this generation will be

$$E_n = \frac{E_0}{2^{(X/\lambda)}} \tag{4.2}$$

where E_0 is the initial energy of the primary particle. As explained above, this process continues until the critical energy is reached ($E_c \approx 87$ MeV for electromagnetic particles). The depth of shower maximum, after which the number of particles decreases, is therefore given by

$$X_{\max} = \lambda \frac{\ln(E_0/E_c)}{\ln 2} \tag{4.3}$$

A similar proportionality relation between the number of particles at the shower maximum and the primary energy, and the depth of shower maximum and the logarithm of the primary energy can be used for hadronic showers also.

The profile of the different components of a cosmic-ray air shower is given in Figure 4.2. The left panel shows the particle densities of different components at various distances from the core. This is the average lateral profile of proton-induced showers of energy 10^{19} eV. The right panel shows the longitudinal distribution of such average showers. As shown in the figure, a major portion of the shower maximum consists of the electromagnetic particles. Therefore, it is justified to consider the maximum of the electromagnetic cascade as that of the entire shower.

4.1.1 Cosmic-ray showers vs. gamma-ray showers

The type of the primary particle heavily affects the contents of the air shower and the depth of shower maximum. Gamma-ray showers, in general, have much lower muonic content than cosmic-ray showers. Figure 4.3 shows the relative number of muons with different energies for various particle types (from [45]).

The figure shows the average case for 1 PeV gamma-ray, proton and iron showers that are vertical. It can be seen that gamma-ray showers on an average have one order of magnitude less muons than hadronic showers. Therefore, a common strategy to identify gamma rays is to look for muon-poor showers.

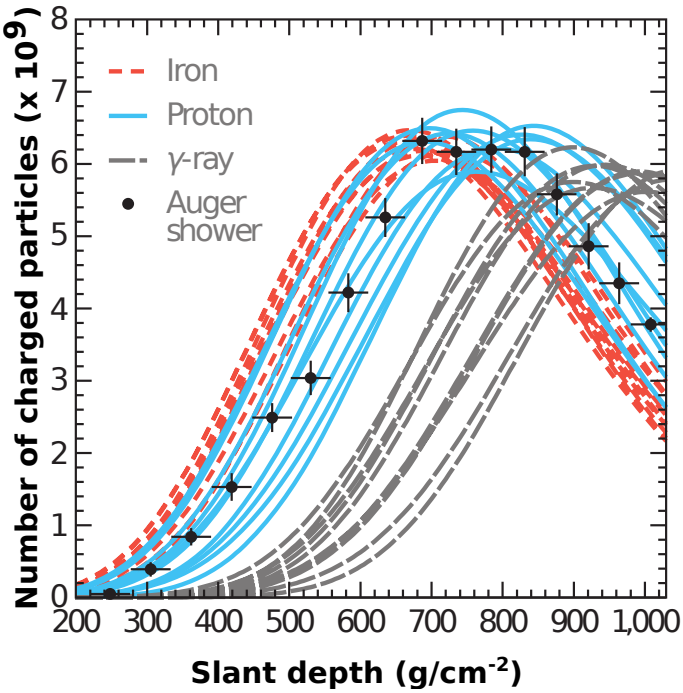

Figure 4.4: The depth of shower maximum for 10 proton, iron and gamma-ray showers of energy 10^{19} eV. Also shown is a shower from the Pierre Auger Observatory (figure from [47]).

Gamma-rays showers normally develop deeper in the atmosphere than hadronic showers of the same energy. Figure 4.4 shows the depth of shower maximum of proton, iron, and gamma-ray showers compared to one shower of similar energy that was measured by the Pierre Auger Observatory [48][47]. It can be seen that iron has a shower maximum earlier in the atmosphere than protons. Gamma rays have a shower maximum at larger slant depths than proton showers. Iron showers have the least amount of fluctuations in the longitudinal shower development among the three species. Gamma and proton showers show much a much more significant amount of fluctuations.

The fraction of calorimetric energy deposited in the atmosphere for different particle species (gamma, proton, iron) at various energies is given in Figure 4.5. This corresponds to the electromagnetic energy of the shower. The fraction of the total primary energy that is deposited in the atmosphere (calorimetric energy) is almost unity for showers induced by gamma rays. As the energy of the gamma rays

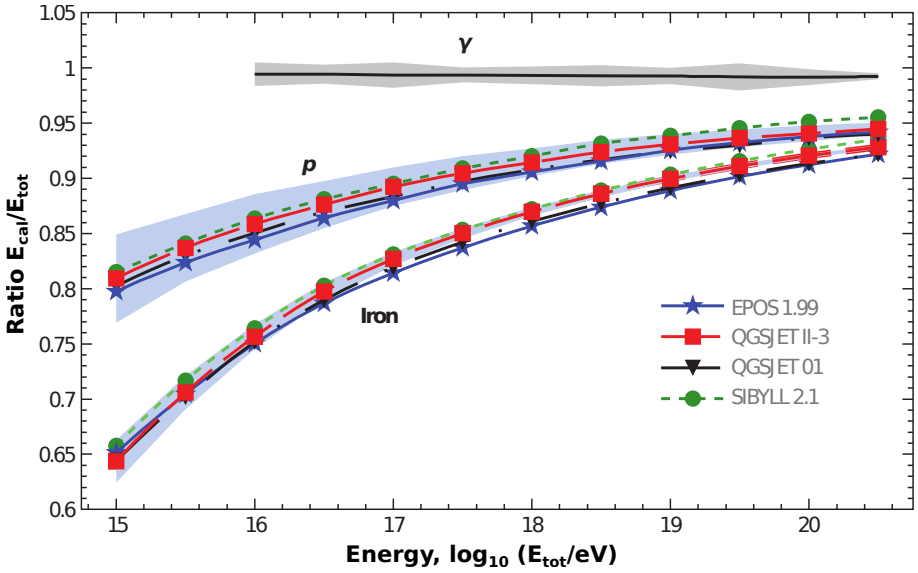

Figure 4.5: The fraction of the total primary energy deposited in the atmosphere is nearly unity for gamma rays. Protons and iron impart some energy to neutrinos and muons, which do not deposit energy in the atmosphere (figure from [47]).

increases, there is a slight decrease in the total electromagnetic energy, due to the increase in the hadronic cross section (which produces the muons). This is however almost two orders of magnitude lower than the electromagnetic cross section, which therefore overpowers for gamma rays at all energies. This is the reason for the almost constant behaviour of the fraction shown in the figure, for gamma rays. Proton and iron showers lose a considerable fraction of their total energy to particle species like neutrinos and muons, that deposit only negligible amount of energy in the atmosphere. However, as the energy of the primary increases, the number of generations that the shower goes through will increase. This in turn increases the total electromagnetic fraction of the shower. This is the reason for the increase in the $E_{\mathrm{cal}}/E_{\mathrm{tot}}$ ratio as the energy of the proton or iron primary increases.

4.1.2 Detection methods

Extensive air showers can be detected using different methods. A common strategy is to use particle detectors on the ground to measure the signatures left by these showers. Some examples of such particle detectors are scintillators and water/ice-Cherenkov detectors. The fluorescence light emitted by the interaction of the particles of the shower with the atmosphere is utilised by some measurement techniques, while some others rely on the Cherenkov light emitted in the atmosphere. Such Cherenkov telescopes are commonly used for ground-based detection of air showers from gamma rays. Certain experiments also use the radio emission from air showers to detect the signatures of the primary cosmic particles approaching the Earth. A schematic of the different methods that are used for air-shower detection is shown in Figure 4.6.

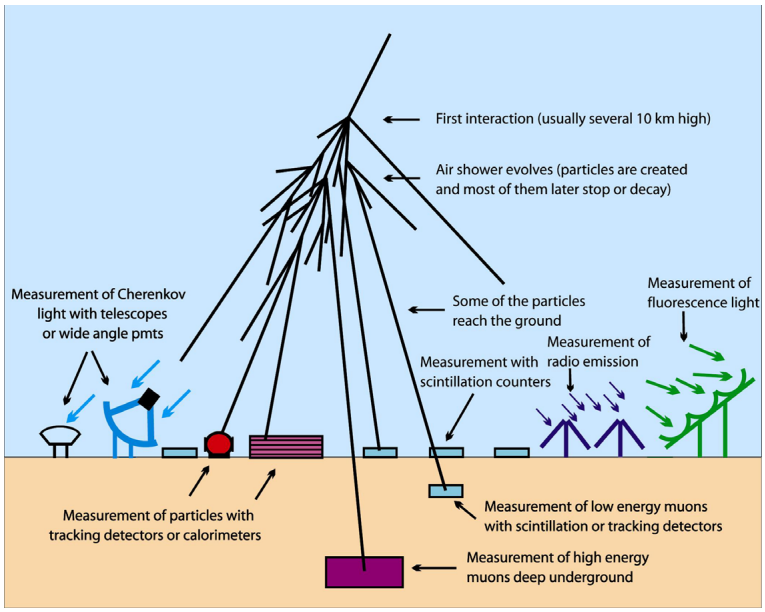

Figure 4.6: A schematic of the different methods used for the detection of air showers. The figure is adapted from [43].

4.2 Radio emission of air showers

Radio emission from extensive air showers was first detected in 1965 using dipole antennas whose signals were read out with an oscilloscope [49]. Following this, there was a spur of activity in this field until the mid-1970's. After this, the activities in this field declined. By the early 2000's, there was an increased interest in the field of radio detection of air-showers. The advent of modern digital technology boosted the ease of taking measurements of radio signals, compared to the pre-1970's era. Today, the field of radio detection of air showers has developed much beyond the state in 1965. The radio detection technique is now successfully used for the measurement of cosmic rays with energies above $10^{16.5}$ eV.

The mechanism of radio emission in air showers depends on the varying charge distribution in the shower. That is, electrons and positrons in the shower are spatially separated with varying distances. The main reason for this separation is the deflection in the magnetic field of the Earth. This results in a time varying current existing between the electrons and positrons. These currents emit electromagnetic radiation that add up coherently from a few MHz to hundreds of MHz. This emission mechanism is called the geomagnetic emission [52]. It is polarised linearly, along the direction of $\vec{v} \times \vec{B}$, where $\vec{v}$ is the direction along the shower axis and $\vec{B}$ is the direction of the magnetic field. This results in an amplitude contribution, from the geomagnetic effect, that is proportional to sin α, where α (the geomagnetic angle) is the angle between the magnetic field and the shower axis. The emission mechanism and the polarisation is shown in Figure 4.7a and 4.7c.

The other mechanism by which radio emission occurs is called the charge excess emission or the Askaryan effect [53][54]. The development of the shower in the atmosphere results in the ionisation of the medium. The heavier ions are left behind while the lighter electrons are swept along with the shower front, as shown in Figure 4.7b. This excess charge along the shower front grows with the shower and dies

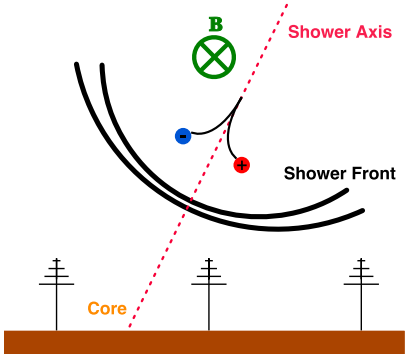

(a) Geomagnetic emission

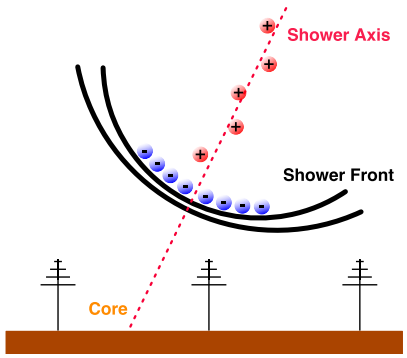

(b) Charge excess emission

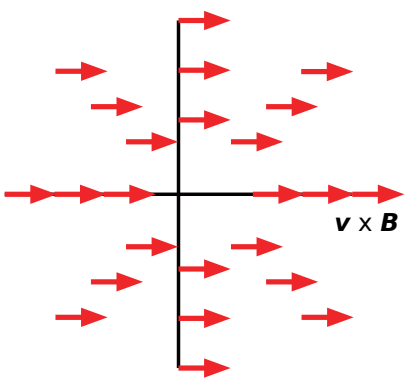

(c) Polarisation of geomagnetic emission

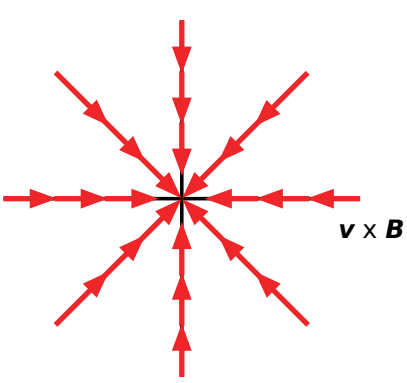

(d) Polarisation of charge excess emission

Figure 4.7: The mechanism of geomagnetic and charge excess emission is shown in (a) and (b). The direction of polarisation of the geomagnetic emission in the shower is perpendicular to the direction of the shower ($\vec{v}$) and the direction of the magnetic field ($\vec{B}$) and is linearly polarised (c). The charge excess emission is radially oriented with respect to the shower axis (d). The figure is adapted from [50] and [51].

along with it, therefore resulting in time varying currents. The polarisation of this emission is radially oriented with respect to the shower axis as shown in Figure 4.7d. The total emission received on the ground from the entire air shower is a net effect of both the emission mechanisms. The total amplitude depends on the location of the antenna. The antenna located on the positive $\vec{v} \times \vec{B}$ axis will have less net amplitude than a corresponding antenna located on the negative $\vec{v} \times \vec{B}$ axis. This results in an asymmetric radio footprint.

The geomagnetic effect is the dominant emission mechanism in air showers. The electromagnetic radiation produced due to the Askaryan effect corresponds to only 5-20% of the total radio emission on the ground. This relative strength between both emission mechanisms depends on the location (which corresponds to the magnetic field: an increase of magnetic field increases the relative contribution of the geomagnetic effect) and also the orientation of the shower axis with respect to the magnetic field (which changes the geomagnetic angle α). On the other hand, the charge excess effect is the dominant mechanism with which radio emission occurs in dense media like ice. Experiments that rely on the Askaryan emission in dense media are mainly focused on the detection of high-energy neutrinos, as discussed in section 4.4.

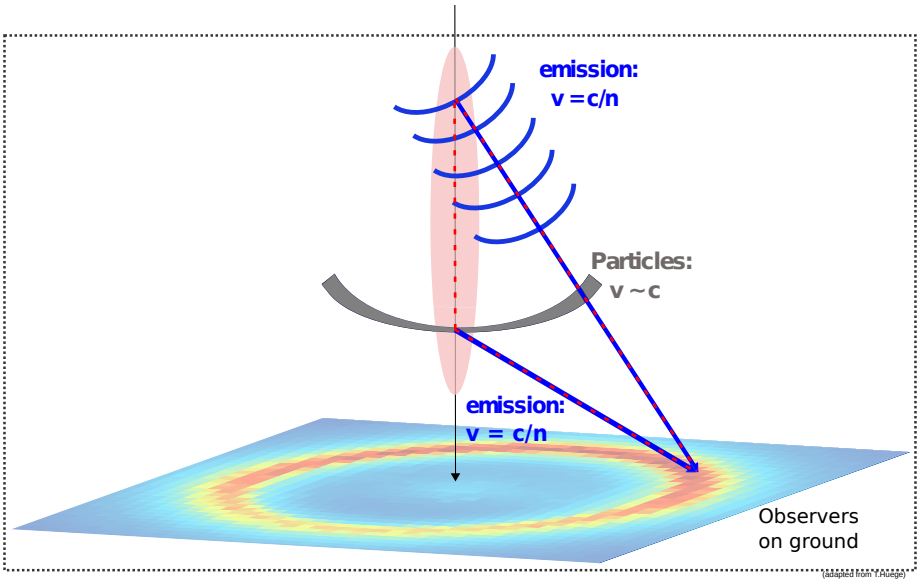

Figure 4.8: Cherenkov emission for a vertical shower. The observers on the ground will see a ring-like formation. The illustration is shown in [56].

4.2.1 Cherenkov effect in radio emission

Another phenomenon that occurs in the radio emission of air showers is the formation of a Cherenkov ring when the radio signals arrive on the ground. The atmosphere through which the radio waves travel has a refractive index which is greater than 1, and has varying values depending on the height of the atmosphere. Due to this, the radio waves travel with a velocity that is given by $v = \mathrm{c}/n$, while the particle front moves with a velocity equal to the speed of light. This situation, therefore, is similar to a sonic boom caused by an emitting source moving with a velocity greater than that of the wave in the medium. Such a scenario results in the radio waves being collimated along a cone. This emission is different from the usual Cherenkov radiation, since the emission is not caused by a charge moving faster than light [55]. It will be visible at an opening angle given by $\cos\theta_c = \frac{1}{n\beta}$ where n is the refractive index and β is the velocity of the particle front.

Along the Cherenkov cone, there is a time compression of the radio signals since the radio signals from all parts of the shower arrive simultaneously at the cone. That is, we will receive shorter pulses, in the time domain, along the Cherenkov cone than at other areas along the radio footprint as shown in [55]. This means that the Cherenkov ring becomes visible at high frequencies. The Cherenkov emission becomes evident at frequencies close to a 100 MHz and this emission is coherent up to frequencies in the GHz range. On the ground, this emission will be seen along a ring, which will be called as the Cherenkov ring, hereafter. Along the Cherenkov ring, an amplification of the radio signal is seen at high frequencies. Such a Cherenkov ring is only marginal in the frequency band 30-80 MHz, which is the frequency range used by most of the existing radio air shower experiments, as discussed in section 4.4. An illustration of the formation of the Cherenkov ring is shown in Figure 4.8.

It is anticipated that the Cherenkov ring is sensitive to the position of the shower maximum. At distances close to the shower axis (inside the Cherenkov ring), the

emission is mainly from the later portion of the shower, that is the part after the shower maximum. At distances from the shower axis that is close to the Cherenkov ring, the emission is sensitive to the distance to the shower maximum. At even larger distances, the received emission is mainly from the early part of the shower, and therefore has much smaller amplitudes than at closer distances. Therefore, we can say that by measuring the Cherenkov ring, it is possible to directly correlate to the shower maximum, which in turn is statistically correlated to the primary particle.

4.2.2 Radio emission from inclined showers

It was proposed in the early 2000's that it is probably more advantageous to observe inclined air showers using the radio detection technique [57]. The relativistically moving particles emit radio waves in a forward-beamed conical pattern. This means that the footprint on the ground depends on the distance of the shower to the observation level. The larger the distance to the ground level, the larger is the area that the cone illuminates. For inclined air showers, this distance is larger than for relatively vertical showers.

Figure 4.9 shows an illustration of the formation of the footprint on the ground from radio signals for inclined and vertical showers. Some representative cones from different parts of the showers are shown as dashed lines in the figure. All of these together will result in a hyperbolic wavefront on the ground. The areas subtended by the cones on the ground is larger for the inclined shower than for the vertical shower as shown in the figure.

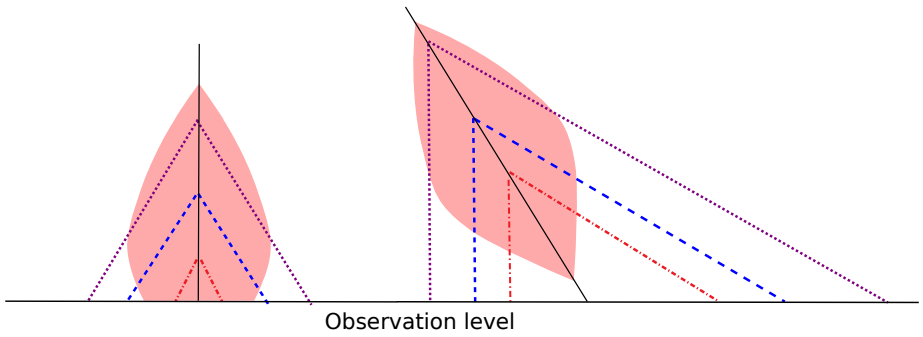

Figure 4.9: The forward-beamed radio emission from each part of the shower moves in a conical manner. On the left is the radio emission from a vertical shower and on the right that from an inclined shower. The dashed lines illustrate a few cones from the shower. The larger geometric distances of inclined showers result in larger area on the ground that receives the radio signals.

This would result in larger radio footprints on the ground for inclined showers as shown in Figure 4.10. The footprint detected on the ground for inclined showers will be elliptical in shape and are impressively large as shown in the figure [7]. Recent studies of inclined air showers by The Auger Engineering Radio Array (AERA) have experimentally proven this [58]. The inclined air showers detected by AERA have energies higher than 10^{18} eV. This feature of large footprints for inclined showers can be used to detect these showers using very sparse arrays of radio antennas. This thereby reduces the cost of the experiment to a large extent.

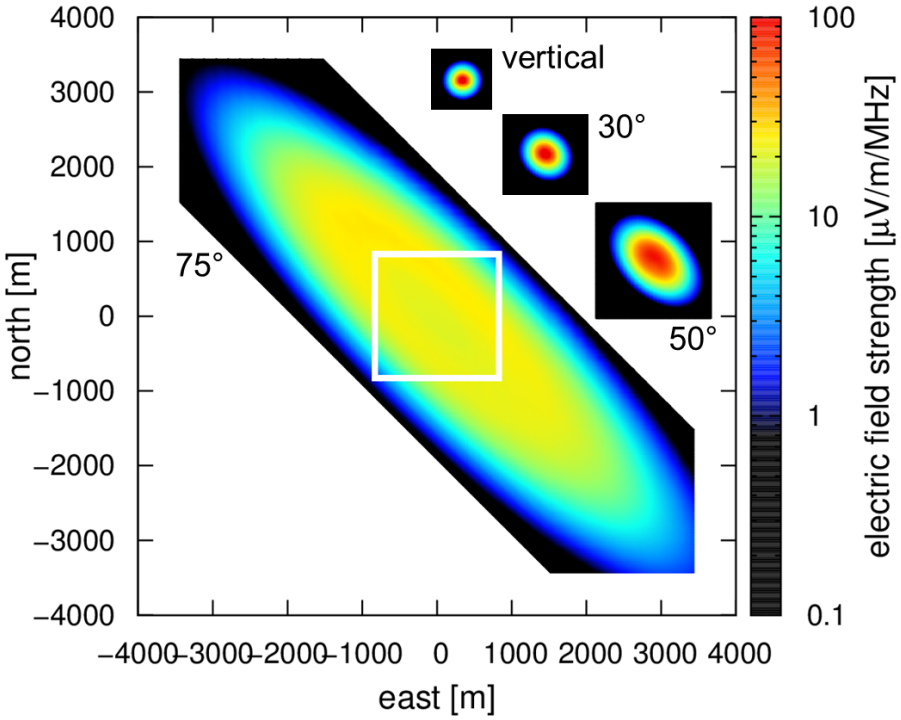

Figure 4.10: The radio footprint of showers with different inclinations. The emission is within the frequency band of 30-80 MHz. There is a very large increase in the shower footprint as the zenith angle increases. The illustration is shown in [7].

4.3 Models for radio emission

There exists a number of models that describe the emission of radio signals from air showers. Some models take up a macroscopic approach while some others have a microscopic approach. MGMR [52] and EVA [59] are two modern macroscopic approaches. They try to express the emission from the air shower particles as drift currents that are caused by the acceleration of the charged particles due to the magnetic field and their deceleration due to the atmosphere. A net effect of the currents is taken up to get a resultant radio signal. Since these models are analytic, they are not computationally intensive. However, since the electric fields are finally added up, there is a risk of double counting. There is also a risk of incorrect description of the signals due to over-simplification of a fairly complex radiation process [60].

ZHS [61] and end point formalism [62] are two modern microscopic approaches that are used widely. These approaches assume each charged particle (electron and positron) to be radiating while in motion and calculate the emission separately from them. These emissions are then added up to have the final signal. Coherence of the signals comes out naturally from this approach. ZHS takes the particle output from AIRES air shower simulation [63] whereas end point formalism takes this from CORSIKA [34]. The combined simulation modules are called ZHAires [64] and CoREAS [65], respectively. While these microscopic approaches describe the emission from the shower well, they are computationally intensive, which limits the number of simulations that can be performed. A comparison of ZHAires and CoREAS showed that the emission predicted by both models converge [66]. In this

thesis, CoREAS is chosen for describing the radio emission from the simulated air showers.

Several experiments have checked for the reliability of the endpoint and the ZHS formalisms for radio emission. LOPES and Tunka-Rex have determined the precision of the endpoint formalism to be within 20% at frequencies from 30-80 MHz[67][68]. The SLAC-T510 experiment, built to determine the validity of the radio emission models, tested the endpoint and the ZHS formalisms. Both of these models were found to describe the measured electric field strength on the antenna to within 5% [56]. Nevertheless, the experiment has uncertainties to nearly 30%. This experiment operated in the frequency range of 200-1200 MHz, and are said to be comparable to measurements in the 10-60 MHz band in air showers (the medium for the electromagnetic shower was polyethylene which therefore has a different refractive index) [69]. Measurements of cosmic rays made at higher frequencies with LOFAR (110-190 MHz) [70] and ARIANNA (100-1000 MHz) [71] also indicate that the data is well described by the emission models.

4.4 Radio experiments

This section discusses some of the radio experiments that are (were) operational in the modern digital era. While some experiments are focused on air-showers, others aim at the measurement of radio emission in dense media. The primary methods and techniques were established with air-shower experiments. It was also more convenient and practical to validate the radio emission mechanisms and test their simulations using air-shower experiments. Some of the common antennas used for radio air-shower experiments are shown in Figure 4.11.

LOPES

The **LO**FAR **p**rototyp**e** **s**tation is the pioneering experiment in the field of radio detection of air showers in the modern age [76]. It was located at Karlsruhe, Germany as an extension to the KASCADE-Grande experiment. In spite of its noisy environment, the experiment provided with the proof-of-principle for the entire field. It also introduced concepts like interferometric detection of radio signals successfully. The frequency band of operation was 43-74 MHz. The LOPES experiment measured the first inclined air shower with the radio technique. The most inclined air shower that was detected by this experiment had a zenith angle of nearly 70° [77].

CODALEMA

CODALEMA (**co**smic-ray **d**etection **a**rray with **l**ogarithmic **e**lectro**m**agnetic **a**ntennas), also one of the first radio air-shower experiments, has been operational since 2003 in France at the Nançay Radio Observatory [78]. It is a km^2 array of autonomous antennas and also has a denser array of antennas that are triggered by scintillators. The antennas operate in the frequency band 20-200 MHz. The first self-triggered antennas were successfully implemented by this experiment. This self-triggered array employed methods for the rejection of man-made noise based on the periodicity of emission of the noise pulses and its pulse shape analysis. With this, a few air shower events were successfully identified [79].

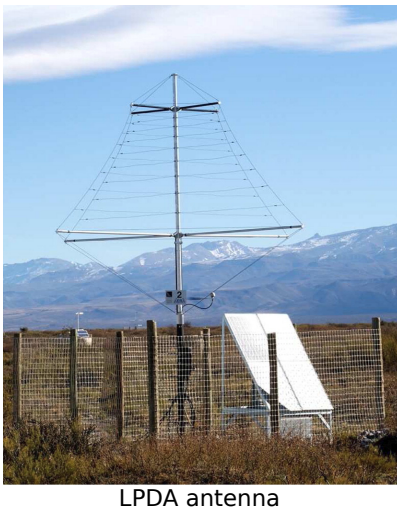
LPDA antenna

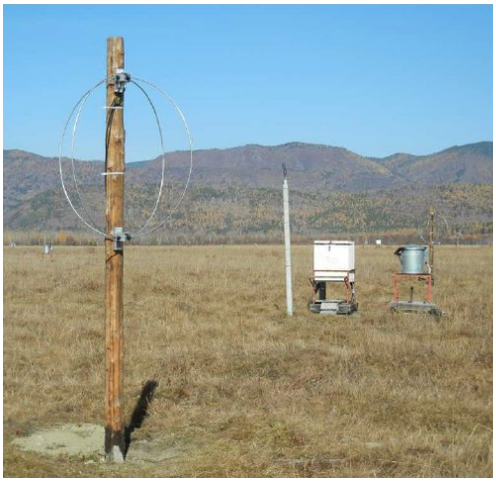
SALLA antenna

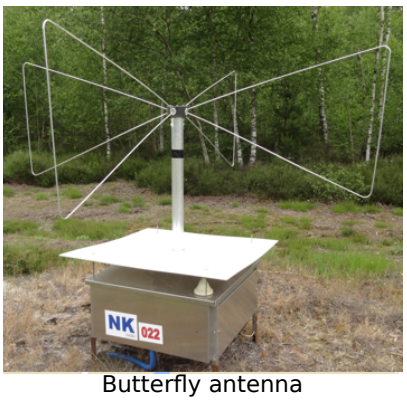

Butterfly antenna

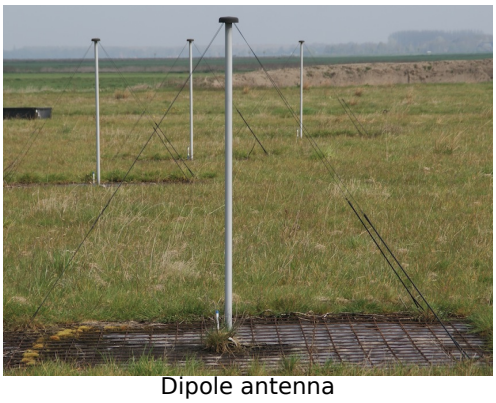
Dipole antenna

Figure 4.11: Some of the types of antennas used for air-shower experiments. An LPDA (logarithmic periodic dipole antenna) used by AERA [72], a SALLA antenna used by Tunka-Rex [73], a butterfly antenna used by CODALEMA [74] and a v-shaped dipole antenna used by LOFAR [75] are shown.

LOFAR

The **Lo**w **F**requency **Ar**ray, based in Netherlands, is aimed at observing astronomical sources, and for observing cosmic ray air showers [80]. It has 40 stations that are spread all over Europe and has a dense core in Netherlands. It consists of antennas that work in the frequency range of 30-80 MHz (low band antennas) and additional antennas that are beam-formed (the signals are delayed to be read at the same time from all antennas, thereby giving rise to an interferometric addition and amplification) and operate in the frequency range of 110-240 MHz (high band antennas). The low band antennas are triggered with scintillators. Air shower measurements are mainly done with the low band antennas. The best resolution for the depth of shower maximum so far is provided by this experiment ($X_{max} \sim 20 g/cm^2$) [81]. With the help of this, LOFAR was able to estimate the mass composition of cosmic rays in the energy range of 10^{17}-$10^{17.5}$ eV [82]. Recently, a measurement of the Cherenkov ring has been reported by LOFAR using the high band antennas [70]. An image of v-shaped dipole antennas used by LOFAR is shown in Figure 4.11.

AERA

The Pierre Auger Observatory at Malargue in Argentina employs an array of radio antennas for the enhancement of its surface detector array [83]. These antennas are triggered using the water-Cherenkov tanks (surface detectors). The radio array, called the **A**uger **E**ngineering **R**adio **A**rray, spans an area of 17 km^2 with 150 antennas. It has been successful in measuring cosmic rays within the frequency band of 30-80 MHz. AERA uses two types of antennas: a log periodic dipole antenna and a butterfly antenna, which are shown in Figure 4.11. AERA mainly aims at the development and improvement of methods that are used for the reconstruction of shower parameters like the direction, the energy and Xmax. For this, the Pierre Auger collaboration has developed a software framework *'Offline'*, which can be used by other experiments also [84][85]. In the future, a large array with an area of 3000 km^2 is planned to be deployed at the site of the Pierre Auger Observatory, for the observation of inclined showers with EeV energies [86].

Tunka-Rex

The radio extension to Tunka-133 and Tunka-Grande in Siberia (**T**unka-**r**adio **ex**tension) consists of 57 antennas within an area of 1 km^2. It also has 6 additional outer stations that extends the total area to 3 km^2 [87]. It uses very economic antennas (SALLA), that operate in the frequency range of 30-80 MHz. Although these antennas are economic, their internal noise level is high, which raises the threshold energy of detection by 40%, in comparison to other antennas [88]. It has successfully showed a cross-calibration between the depth of shower maximum measured by the radio technique and the air-Cherenkov technique [89].

SKA-low

The **S**quare **K**ilometre **A**rray is a future radio array that will be located in West Australia [90]. It has a low frequency component, called SKA-low, that is planned to operate in the frequency range of 50-350 MHz. It will consist of 70000 antennas located in an area of 0.4 km^2, thereby forming the most dense radio array. The SKALA antenna (SKA-log periodic antenna), which is a combination of LPDA-like and butterfly-like structures, is a state-of-the art antenna developed for SKA-low. This antenna has a low internal noise, with a favourable gain pattern at nearly all zenith angles. Section 4.5.2 shows these features of the SKALA antenna in further detail.

TREND and GRAND

TREND (**T**ianshan **R**adio **E**xperiment for **N**eutrino **D**etection) consists of an array of 50 antennas, deployed over a total area of 1.5 km^2 [91]. This antenna array is located in a radio-quiet valley in Tianshan, China. The antennas are triggered by themselves, with a simple signal-over-noise threshold condition, and operate within a frequency range of 50-100 MHz. Air showers with energies greater than 6×10^{17} eV have been detected by this array.

TREND is considered as the predecessor to GRAND (**G**iant **R**adio **A**rray for **N**eutrino **D**etection) [92]. This is a planned large scale array that will be used for the detection of neutrinos of the highest energies, by using mountains as the medium

of interaction for the neutrinos. Additionally, it can also detect cosmic rays of the highest energies. The initial setup of GRAND (GRANDProto35) will consist of 35 antennas and 21 scintillators in the Tianshan valley, and will be used for prototype measurements and proof of principle. The next stage, GRANDProto300 will consists of 300 antennas over 300 km^2 area. This is expected to be a self-triggered radio array that can measure inclined showers. It is also planned to have water-Cherenkov detectors for the detection of muons, in addition to radio detectors for this stage of the detector array. This will help in the independent measurement of the electromagnetic and muonic components of the air shower. In the final stage, a worldwide array of 2×10^5 antennas over 2×10^5 km^2 is planned, after choosing the best sites in the world for neutrino interaction in mountains [92].

ANITA

ANITA (**An**tarctic **i**mpulsive **t**ransient **a**ntenna) is an experiment that aims at measuring neutrinos that interact in the Antarctic ice [93]. The balloon-borne experiment searches for Askaryan radio emission from neutrinos that travel upwards in the ice. It uses horn antennas that operate in the frequency range of 200-1200 MHz. For successful measurements, the Cherenkov ring of the radio emission has to directly fall on the antennas mounted on the balloon. ANITA has successfully measured cosmic rays with an energy $> 10^{19}$ eV, by measuring their reflected signature on the Antarctic-ice surface [94].

ARIANNA and ARA

Antarctic **R**oss **I**ce Shelf **an**tenna **n**eutrino **a**rray and **A**skaryan **r**adio **a**rray are operating prototype experiments with the objective of measuring radio emission from the interaction of extremely high energy neutrinos in ice [95] [96]. These neutrinos will have energies much higher than the range of IceCube or IceCube-Gen2 (EeV range). While ARIANNA operates with antennas located on the surface of ice, pointing downwards, ARA has antennas that are drilled deep within ice. The prototype phase of ARIANNA consists of 7 stations with 4 downward antennas and 1 upward antenna (LPDA) that operate in the frequency band of 100-1000 MHz. The current ARA prototype station consists of 4 strings with 4 dipole antennas each that operate within 150-800 MHz. Recently, an additional string with phased antennas that are closely spaced (with 1 m distance between them) was added, to improve the trigger performance [97]. In the future, it is planned to build a large Radio Neutrino Observatory at the South Pole combining the advantages of both the approaches.

RASTA

Radio **A**ir-**S**hower **T**est **A**rray was an effort to establish the feasibility of radio detection of air showers at the South Pole [98] [99]. Under the umbrella of this proposal, 6 fat-tube dipole antennas, developed for ARA, were deployed in trenches (0.5 m deep) that were filled with snow. The frequency band was fixed to 30-300 MHz. The antennas took background measurements at the South Pole, which were found to be very low, and consistent with the expected levels of Galactic noise (see chapter 5). A few runs with a calibration pulser was also used to test the ability of

the deployed antennas to identify the signals produced by the pulser, at South Pole [100].

4.5 A radio air-shower array at the South Pole

As mentioned in the previous chapter, the IceTop array is planned to undergo an enhancement using scintillators. With this goal, 14 prototype scintillators are currently at the Pole. Additional radio antennas along with the planned scintillator array will improve the air shower measurements considerably. This can allow us to have a hybrid detector setup at the Southern hemisphere.

It will be highly advantageous to tap into the existing DAQ system of the scintillators, and plug in the radio antennas to this. This can reduce the costs of the radio array considerably. Since there are already prototype scintillators at the Pole, it is an ideal opportunity to test radio antennas also along with it. It is expected to have a few antennas at the South Pole in the Austral summer of 2018/2019 for prototype measurements. This thesis considers a layout of the radio array with 81 antennas on an area of 1 km^2, i.e. one antenna per IceTop position, since the layout of the scintillator array is not yet finalised. This section describes the advantages and the scientific potential of a radio air-shower array at the South Pole, as discussed in [101].

4.5.1 Scientific prospects of the radio array

A surface array of radio antennas in close cooperation with the existing and the future particle detector arrays at the Pole could potentially increase the accuracy for the detection of air showers. It will enable the exclusive measurement of the total electromagnetic components of the air shower. When used in combination with the particle detectors, we can use this for the separation of the muonic and electromagnetic parts of the shower.

Mass composition

Radio detection has the advantage of being able to measure the direct effects of the longitudinal shower development using measurements at different parts of the footprint. A measurement of the Cherenkov ring will provide us with an opportunity to directly measure the shower maximum. The starting vertex of the Cherenkov cone is closely related to the depth of shower maximum. Therefore, this information, along with the information of the signal strength at the Cherenkov ring, will help in probing the shower maximum. This will in turn help in the identification of the particle species.

IceTop is losing its sensitivity to the electromagnetic component from air showers with time, due to the increasing levels of snow that is accumulated on top of the detectors. This is already described in section 3.1.1. These electromagnetic components can be recovered with the help of the radio antennas, which act as excellent calorimeters for this part of the shower. In this manner, we can use the radio antennas for measuring the electromagnetic part and the IceTop tanks, the scintillators, and the in-ice detectors for measuring the muonic part. Such a setup will give a unique way of measuring the particle species of the air showers. It was already shown in [102] that a combined measurement of the muons and the radio

emission from air showers is highly beneficial for mass-composition studies. This will help in determining the mass composition of the showers and will provide valuable information of the composition near to the knee, and beyond, of the cosmic-ray spectrum.

Anisotropy and model improvements

Using this kind of a combined scheme for measuring the composition of air showers on an event-by-event basis will be extremely useful. The presence of a weak anisotropy at energies below 2 PeV [103] and above 8 EeV [104] is observed, while the flux is nearly isotropic at PeV energies. It is also observed that Galactic cosmic rays in this energy range are closer to a heavy composition [105] while extragalactic cosmic rays below 10^{19} eV are mainly expected to be light in composition [106]. Therefore, very detailed mass information is required to study anisotropies in the PeV energy range. The use of the surface radio array can be advantageous for such a study. The radio antennas can measure the electromagnetic component and the particle detectors on the surface, along with the in-ice detectors can measure the muonic contribution which directly gives a hint for the physics of hadronic interactions at high energies. Such a measurement will also help in understanding particle physics in the forward direction. This will therefore be advantageous for the improvement of the existing models of air-shower physics.

Inclined air showers

A hybrid detector array would especially be advantageous for the detection of inclined air showers at the South Pole. IceTop-analyses of air showers includes only those showers approaching the detector array within an inclination of less than 40°. Even though IceTop is capable of measuring inclined air-showers that have its core within the array, albeit at higher energies than the vertical showers, these are not dealt with in the analysis. The addition of radio antennas will significantly improve the detection of these inclined showers. As mentioned in section 4.2.2, inclined showers leave a very large elliptical radio footprint on the ground [7]. This can be used to our advantage. It is widely known that the particles reaching the ground from inclined showers are mainly muons. This, combined with the complete information of the electromagnetic components from radio measurements will be extremely useful for mass composition studies.

Improvement of the veto

The radio antennas will be able to measure signals from air-showers that have a core even outside the detector array. Since radio arrays do not rely on the particles approaching the ground, even air-shower signals from far off can be detected by the antennas. This is especially useful for increasing the veto-coverage of the surface array, and thereby increase the effective area of IceCube in the southern sky. In addition to this, such a radio array on the surface can act as a veto for the future in-ice radio detectors that aim at the detection of extremely high energy neutrinos (Gen2-radio, ARA, ARIANNA).

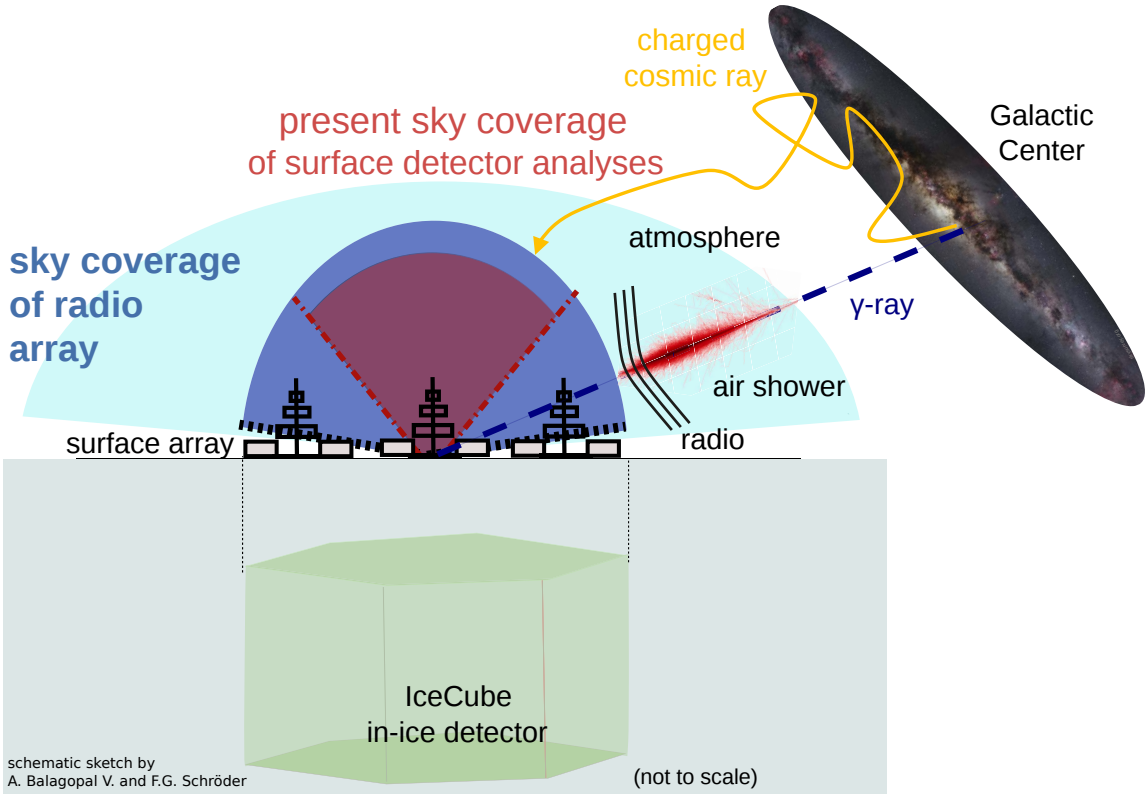

Figure 4.12: A schematic of the scientific scope of a proposed surface radio array at the South Pole. This radio array can be used along with the existing surface detectors (IceTop), its future enhancement with scintillators, and the in-ice detectors to form a hybrid array. The surface-radio array will increase the sky coverage for the detection of air showers, improve air-shower measurements and also enable the search for PeV gamma rays from the Galactic Centre. The figure is adapted from [101].

PeV gamma-ray search

Finally, it will also help in the detection of PeV gamma rays from the centre of the Milky Way [107]. The location at the South Pole is very unique on Earth since it provides a 24/7 exposure to the Galactic Centre. The Galactic Centre is always located at an elevation of 29° (zenith angle $\theta = 61°$). This means that PeV gamma rays that enter the atmosphere from this direction will produce air showers, which can be discovered from the South Pole. Due to its high inclination, such potential PeV showers will only leave a few particles on the ground, since majority of them will be absorbed by the atmosphere. This means that particle detectors on the ground will not be able to effectively reconstruct such showers, due to the low number of hits. On the other hand, the radio emission from this shower will survive and can be detected using antennas on the ground. It is already known that inclined showers leave a large footprint on the ground, which can be used to our advantage.

However, the state-of-the art radio experiments have successfully detected air showers only with an energy above $10^{16.5}$ eV. Therefore, it is crucial to lower the energy threshold of the technique of radio detection of air-showers. With this goal in mind, the work within this thesis has successfully determined a method for lowering the energy threshold. This method for lowering the energy threshold for

radio detection of air-showers down to ≈1 PeV will be discussed in detail in the following chapters. A schematic of the scientific potential of the radio-extension of the surface array at IceCube is given in Figure 4.12.

4.5.2 Test antennas at the South Pole

Based on the work of this thesis, two prototype antennas will be deployed at the South Pole in the Austral summer of 2018/2019. SKALA antenna, which is a state-of-the-art antenna that has been developed for the SKA-low experiment in Australia [108] will be used for these test measurements. The antenna has low internal noise and high gain even at large zenith angles [108], which makes it ideal for the detection of inclined showers. It operates within the frequency band of 50-350 MHz. The existing DAQ system of the scintillators at the South Pole will be connected to the antennas [109]. Tests using a freezer system have already shown that the LNA at the foot-point of the antenna has a stable gain within the operating frequency band at low temperatures [109].

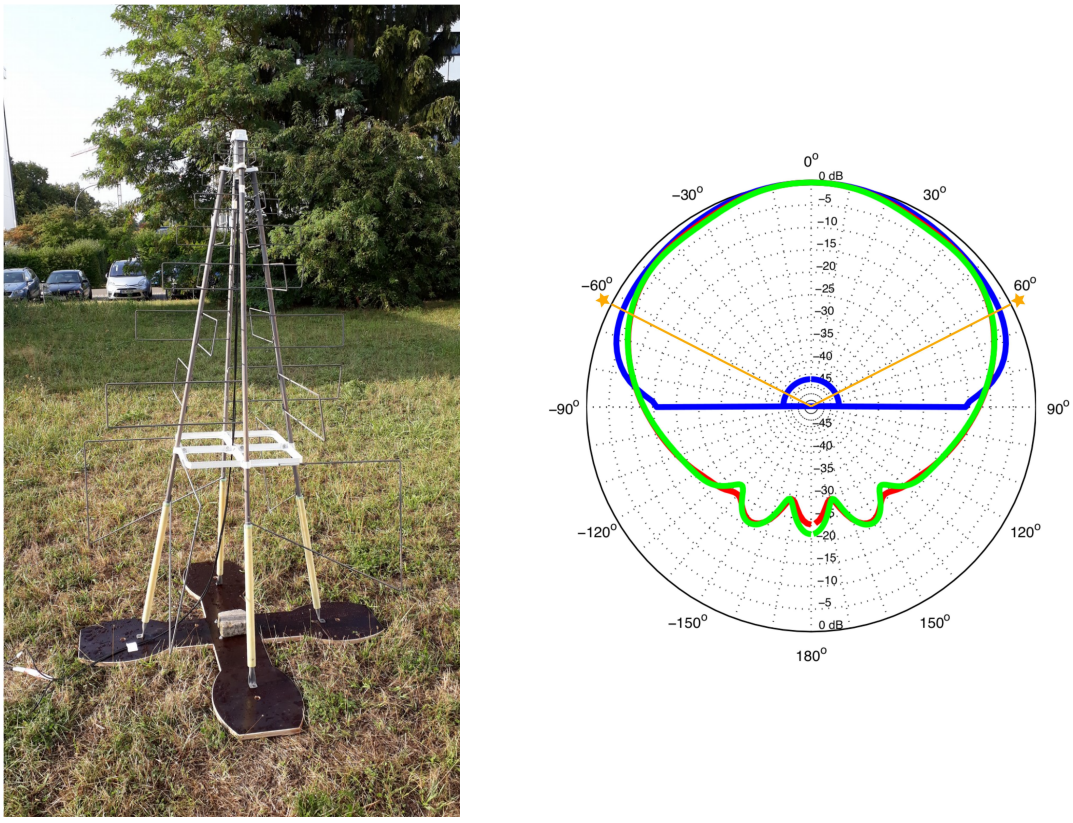

Figure 4.13: A SKALA antenna (version-2) at Karlsruhe is shown in the left panel. The right panel shows a simulation of the directivity of the SKALA antenna (version-1). The blue curve shows the antenna kept over infinite ground, the red curve shows the directivity for the antenna on soil and the green for the antenna on mesh on top of the soil. Also shown is the zenith angle of 61°, where the Galactic Centre is at the South Pole. The figures are shown in [109]. The directivity is adapted from [108].

The SKALA antennas will be used for measuring the ambient conditions at the South Pole. Their durability and stability in the South Pole conditions will be determined during this test season. The current noise conditions at the South Pole,

the effect of snow on radio signals, and the prevention of snow accumulation on the antennas are some of the tests that will be done with these prototypes. A picture of a SKALA antenna at Karlsruhe is shown in Figure 4.13. This is the version-2 prototype of the SKALA antenna, which will be used for the test measurements at the South Pole. Also shown in Figure 4.13 is the gain pattern of the version-1 of the SKALA antenna.

CHAPTER 5

Study of Noise for Radio Measurements

One of the major challenges for the detection of radio signals from air showers is the irreducible background noise, from which the signal should be distinguished. This is particularly difficult for PeV showers since the amplitude of the radio signals are comparable with the signals from the background at these primary energies. Thus, in order to detect the radio signals from PeV showers, the radio background is studied in detail. This chapter deals with the noise for radio measurements and its treatment in the simulations.

5.1 Sources of noise

The power of the radio background at any given time depends on the location at which the measurement is taken. The total radio noise detected at any location on the Earth is due to various factors that can be both external as well as internal. These noise sources can either be transient or steady in nature. Depending on the location, the external sources of noise can either contribute significantly to the total noise, or not.

The internal factor of the total noise—here called the thermal noise of the antenna—arises due to the antenna characteristics, the electronic noise, etc. This thermal noise is irreducible for a given antenna design. The external sources of noise range from Galactic noise through man-made noise to noise produced by atmospheric events. The relative prominence of each source of external noise at different frequencies is shown in Figure 5.1, which is based on the sources of radio noise given by ITU (International Telecommunication Union) in [110].

In the figure, the curve A represents the noise generated by atmospheric sources i.e. radiation from lightning. During thunderstorms the production of large electric fields are seen in the atmosphere, which largely affects the radio signals from air-showers. Man-made noise (RFI) normally produces very narrow band pulses, that look very similar to radio pulses from air showers. These can be easily mistaken for air-shower signals and one needs to be very careful while measuring in such an environment, in order to avoid false signals. An average range of the man-made noise in both city and radio-quiet zones are shown by the curve B in the figure. Apart from this, there will also be contributions from the celestial sources in the

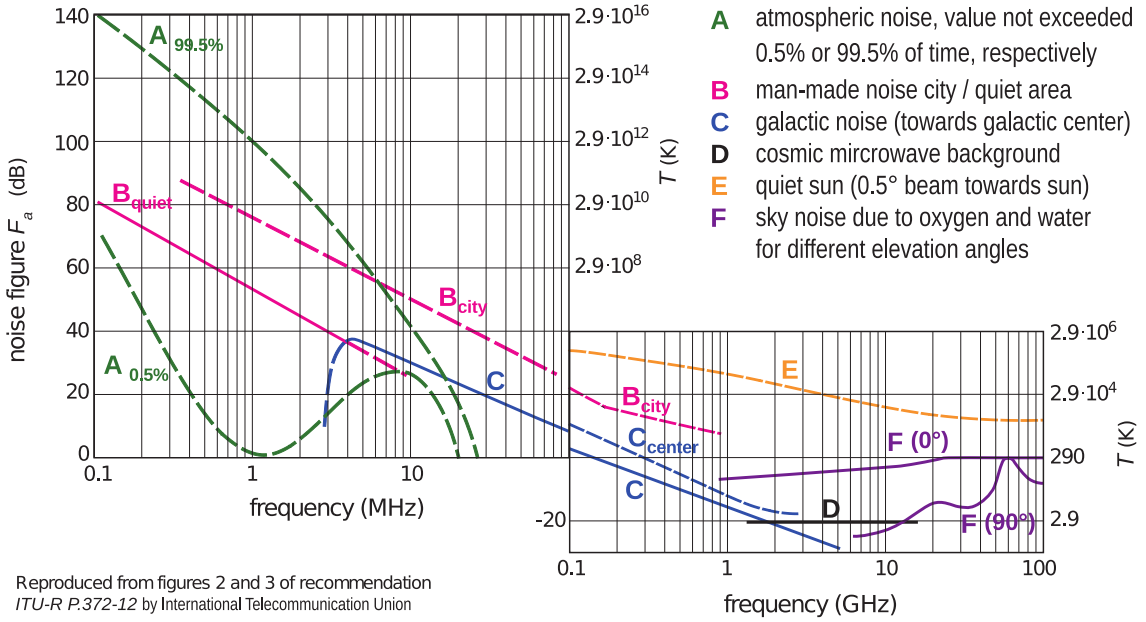

Figure 5.1: Radio noise from various sources at different frequencies. Here, F_a is a figure of the noise power within a given bandwidth. This figure is reproduced in [88] from the recommendations given by ITU in [110].

Galaxy, which contributes largely and continuously to the noise seen in air-shower experiments. The average Galactic noise at different frequencies from regions of the sky close to the Galactic Centre and away from the Galactic Centre are shown by the curve C in the figure. The cosmic microwave background (CMB), which acts like a black body with a temperature of 2.7 K acts as a source of noise in the GHz frequency range. This does not affect air-shower experiments as they normally operate in the MHz range. The level of noise from the CMB can be seen in the curve D in the figure. The sun, which also acts similar to a black body emits radio waves, which contribute significantly to experiments which have their antenna beams focused in this direction (curve E). For example, the sun falls in the field of view of the ANITA experiment and hence is a major source of noise. The sun acts as a significant source of noise only in the case of antennas that are highly beamed within a small angle, and if the sun falls directly within this field of view. Finally, there are also emissions from atmospheric gases which act as a source of noise in the GHz frequency range (curve F), and is therefore insignificant for air-shower experiments. We can also have contributions from external thermal noise. By choosing an antenna with a gain pattern that points upwards, it is possible to reduce the impact of this external thermal noise (e.g. there is $\approx$ 200 K thermal noise of the ice at the South Pole compared to the low $\approx$ 2.7 K thermal background of the sky).

The contributions to noise from various sources shown in Figure 5.1 is only an average behaviour. The real behaviour at each location on Earth depends on the particular environment of the location. This will be discussed in more detail in the following section. At the South Pole, the external contribution mainly comes from the Galactic noise. The contributions from the other external factors are expected to be much lower in comparison. This has already been observed by previous radio-measurement efforts at the South Pole [24].

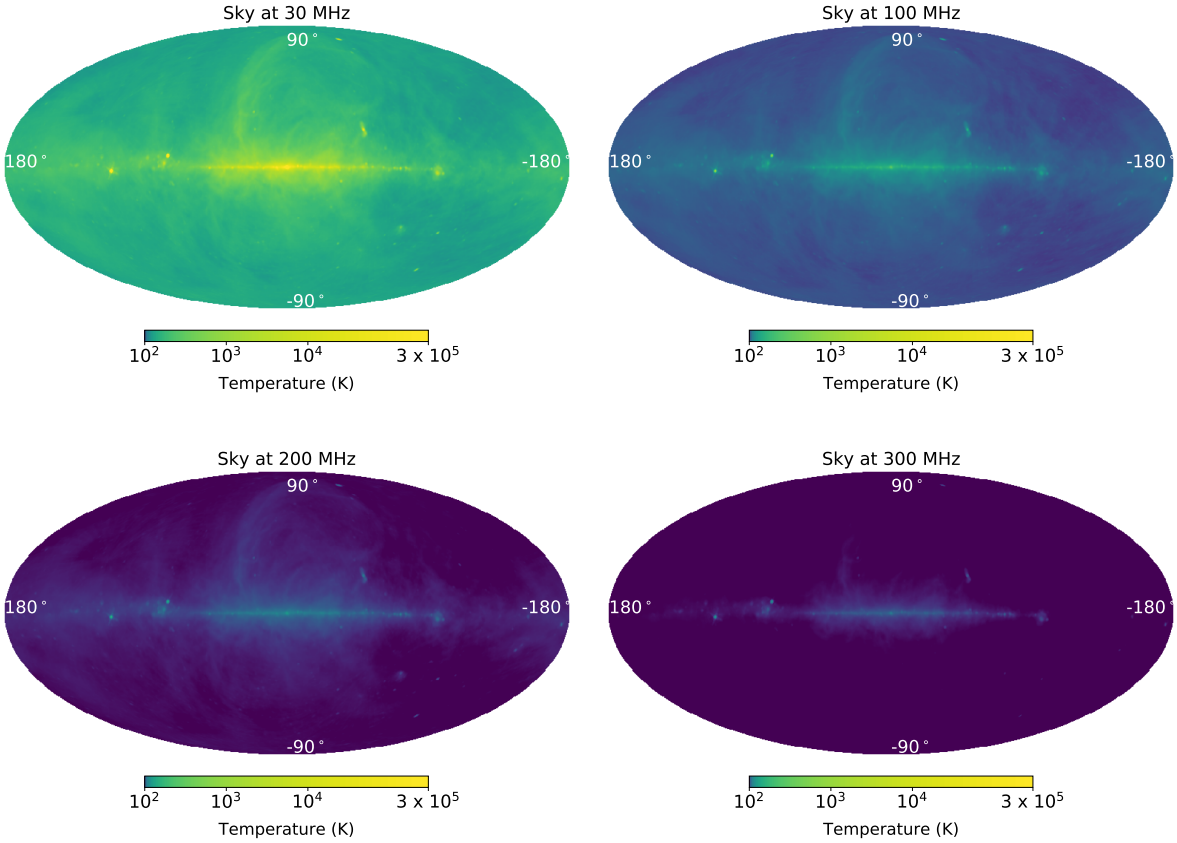

Figure 5.2: Galactic noise maps in units of temperature (K) generated at different frequencies generated using the Global Sky Model (GSM) [111]. The plot is shown in the Galactic Coordinate system. It can be seen that the noise is in general higher at the Galactic Plane. An average of this noise is received at the antenna foot-point. The noise temperature decreases with frequency.

5.2 Galactic Noise

The noise from the Milky Way is produced by various active sources in our galaxy, undergoing different kinds of (violent) processes. These sources have varying levels of emissions, in units of temperature. Moreover, the temperatures change with the frequencies. As we move to higher frequencies, the temperature goes down. This can be seen in Figure 5.2. An average of the radio emissions from these sources is observable at any given time and any given frequency. The average value will change depending on the part of the sky that is visible during the measurement time. That is, the measured radio noise also depends on the local sidereal time. At a given sidereal time, the more the galactic plane is visible the higher will be the background. This is obvious from Figure 5.2 as the temperature at the Galactic Plane is higher than that at other locations in the Galaxy, at all frequencies.

There are three generally known models that describe the radio noise from the celestial sources (here mentioned as Galactic noise) at different frequencies. These are the Cane model [112], Global Sky Model (GSM) [111] and LFmap [113]. All of these models function by applying a fit to measurements of radio noise. The Cane model takes information from radio-radiation surveys that measured the South and

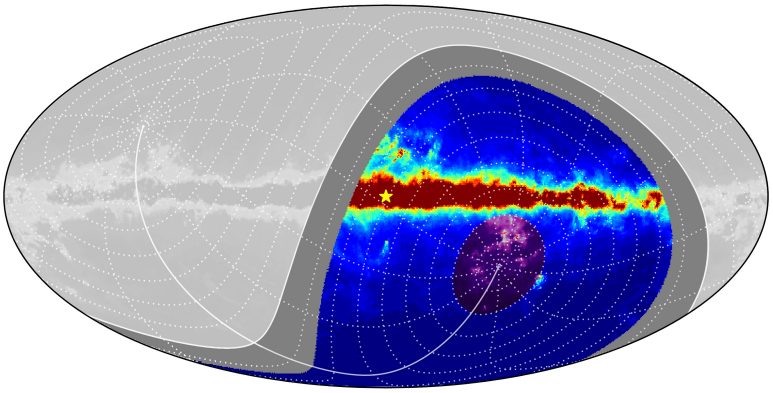

Figure 5.3: The sky that is visible from the South Pole at all times. The colourful region covers the zenith angle range from 0°-75°. The dark gray band implies the sky visible above the horizon, but with high values of zenith angles (75°-90°). The light gray band shows the northern sky. The location of the Galactic Centre is given by the yellow star. The plot is taken from [115].

North Galactic Poles of the sky and gives an average fit of the form:

$$B(\nu) = B_{\mathrm{g}}(\nu)\frac{1 - \mathrm{e}^{-\tau(\nu)}}{\tau(\nu)} + B_{\mathrm{eg}}\mathrm{e}^{-\tau(\nu)} \tag{5.1}$$

where $B(\nu)$ is the noise expressed in terms of brightness, $B_{\mathrm{g}} = 2.48 \times 10^{-20} \times \nu^{-0.52}$ is the galactic contribution to the total brightness, $B_{\mathrm{eg}} = 1.06 \times 10^{-20} \times \nu^{-0.80}$ is the extragalactic contribution and $\tau = 5.0 \times \nu^{-2.1}$ is the optical depth of absorption. For details of the conversion of brightness to temperature, see section 5.3. (For further details of the Cane model, see [112]). GSM and LFmap are models that fit the most accurate sky surveys at various frequencies. These models are more detailed than Cane and give directional-dependent radio emission from the sky.

The same portion of the Milky Way is visible from the South Pole at all times. This is shown in Figure 5.3. Thus, the Galactic radio noise is mostly constant at all sidereal times at the South Pole. Hence, it is safe to consider an average noise model for the South Pole and we do not have to rely on detailed models like GSM or LFmap.

In this study, we use the simplified and average model of diffuse Galactic noise developed by Cane as shown in equation 5.1. It has already been shown by measurements from RASTA and ARA that the Cane model describes the Galactic noise measured at the South Pole with a reasonable accuracy [114][24]. For a comparison between the Cane model and GSM, see appendix A. Figure 5.4 shows the average brightness from Galactic sources given by the Cane model as a function of frequency.

The total noise

The brightness at various frequencies extracted from the model is converted into temperature and is used for determining the Galactic contribution to the total noise. In addition to this Galactic noise, the contribution from the thermal component

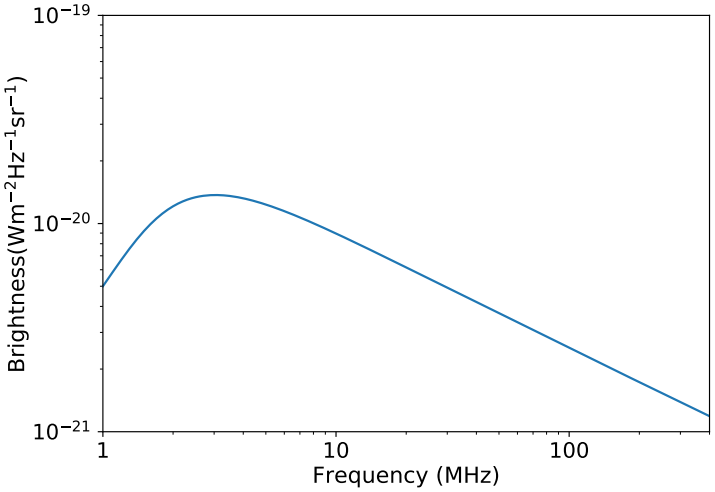

Figure 5.4: Brightness of the Galactic radio background radiation given by the Cane model [112] as shown in [107]. This entire emission can be considered as that of a black-body.

should also be taken into account. A thermal noise of 300 K is mainly considered in this study. With a very simple hardware, the thermal noise contribution could even be more than 300 K. Much lower noise levels of a few tens of K can be achieved by dedicated hardware optimisation. This thermal noise is added to the Galactic noise to give the total expected radio noise at the antenna foot-point in units of temperature. Further details about converting this to the noise measured by the antenna is given in the next section. Here, we do not consider other transient sources of noise since they are expected to be low at the South Pole.

Figure 5.5 shows the average Galactic noise from Cane, the thermal noise and the resulting total noise at different frequencies. This is shown for high (300 K) and low (40 K) thermal noise levels. We can see that the average Galactic noise diminishes as the frequency increases, as expected from Figure 5.2. A cross-over frequency is seen for both cases, above which we become mainly limited by the thermal noise. For the 300 K thermal noise case, this is $\approx$ 150 MHz and for the 40 K thermal noise case the cross-over frequency is $\approx$ 320 MHz. Beyond this cross-over frequency, we have a nearly constant level of noise, which gets added on as we make the frequency band wider.

5.3 Generating a noise trace

As mentioned in the section above, the Cane model provides the Galactic noise in units of brightness ($B(\nu)$), as a function of frequency. Assuming the source of Galactic noise to be a blackbody and hence using the Rayleigh-Jeans law, we can relate the brightness to its brightness temperature.

$$B(\nu) = 2\mathrm{k_B}T\frac{\nu^2}{c^2} \qquad [\mathrm{Wm^{-2}sr^{-1}Hz^{-1}}] \tag{5.2}$$

where $\mathrm{k_B}$ is the Boltzmann's constant and T is the brightness temperature.

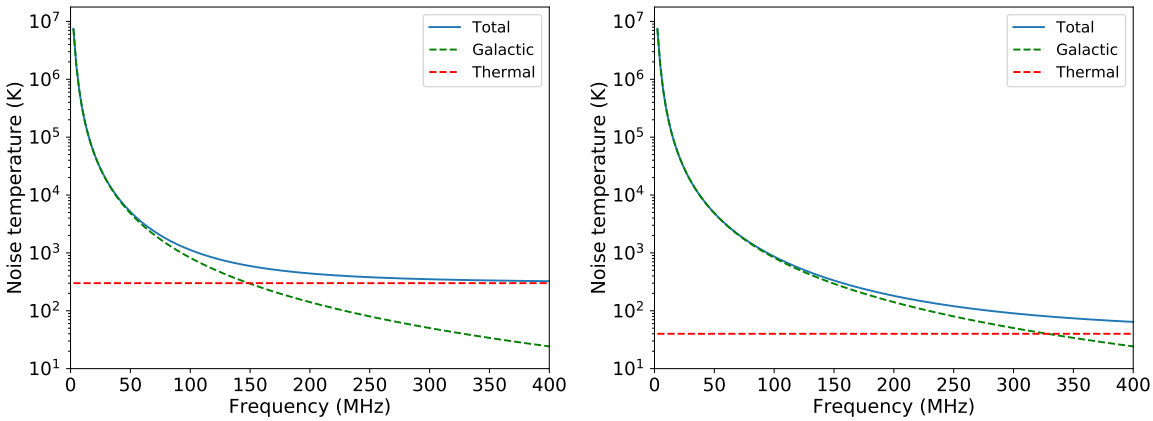

Figure 5.5: Total noise temperature as a function of frequency with (a) 300 K thermal noise and (b) 40 K thermal noise. This left plot is from [107].

We can add thermal noise due to the electronics of the receiving system to the brightness temperature in order to obtain the total noise temperature.

$$T_{\rm tot} = T_{\rm brightness} + T_{\rm thermal} \tag{5.3}$$

The electromagnetic power of the noise obtained in the frequency band $\delta\nu$ from solid angle $\mathrm{d}\Omega$ by an antenna of effective area of $A_{\rm eff}$ is,

$$P_\nu(\theta,\phi) = \frac{1}{2} B(\nu)\mathrm{d}\Omega\ A_{\rm eff}(\theta,\phi)\ \delta\nu \tag{5.4}$$

Here, a factor of $1/2$ has to be added in order to account for the fact that the antenna can extract power only from one of the polarisations of the incoming electromagnetic wave. The effective area can be related to the gain of the antenna as

$$\mathrm{A_{eff}}(\theta,\phi) = \frac{\mathrm{G}(\theta,\phi)\times\lambda^2}{4\pi} \tag{5.5}$$

One can then integrate over θ and ϕ to obtain the total received power within the band $\delta\nu$.

$$P_\nu = \frac{1}{2} 2\mathrm{k_B}T \frac{\int G(\theta,\phi)\mathrm{d}\Omega}{4\pi}\ \delta\nu \qquad [\mathrm{W}] \tag{5.6}$$

Alternatively, one can derive the voltage developed on the antenna arm from the Poynting flux of the received radio noise. The Poynting flux per unit frequency is obtained by integrating the brightness over the solid angle.

$$\begin{aligned} S &= \int B(\nu)\mathrm{d}\Omega \qquad [\mathrm{Wm^{-2}Hz^{-1}}] \\ &= \frac{2\mathrm{k_B}\nu^2}{c^2}\int T(\theta,\phi)\mathrm{d}\Omega \end{aligned} \tag{5.7}$$

The Poynting flux within the frequency interval of $\delta\nu$ is then,

$$\begin{aligned} S_\nu &= S\delta\nu \qquad [\mathrm{Wm^{-2}}] \\ &= \frac{2\mathrm{k_B}\nu^2\delta\nu}{c^2}\int T(\theta,\phi)\mathrm{d}\Omega \end{aligned} \tag{5.8}$$

Again, the Poynting flux extracted at the antenna is $S_{\mathrm{rec}} = \frac{S_\nu}{2}$ for reasons of polarisation matching. We can relate the Poynting flux to the electric field delivered to the antenna as,

$$|\overrightarrow{S}| = \frac{1}{2n\mathrm{Z}_0}|\overrightarrow{E}|^2 \tag{5.9}$$

where $\mathrm{Z}_0 = 376.7303$ Ohm is the vacuum impedance. Taking the refractive index of air to be 1, the amplitude of the electric field at the antenna because of the Galactic noise can then be obtained from the Poynting flux as,

$$\begin{aligned} |\overrightarrow{E}| =& \sqrt{S_{\mathrm{rec}} 2\mathrm{Z}_0} \qquad [\mathrm{V/m}] \\ =& \sqrt{\frac{1}{2} 2\mathrm{Z}_0 \frac{2\mathrm{k_B}\nu^2\delta\nu}{c^2} \int T(\theta,\phi)\ \mathrm{d}\Omega} \end{aligned} \tag{5.10}$$

Thus, the voltage developed at the antenna is

$$V(\nu) = \overrightarrow{E} \cdot \overrightarrow{l_{\mathrm{eff}}} \qquad [\mathrm{V}] \tag{5.11}$$

where l_{eff} is the effective height of the antenna, that is related to the effective area by the following equation.

$$|\overrightarrow{l_{\mathrm{eff}}}(\theta,\phi)| = 2\sqrt{\frac{A_{\mathrm{eff}}(\theta,\phi) Z_{\mathrm{ant}}}{Z_0}} \tag{5.12}$$

with Z_{ant} being the impedance of the antenna. Since we have already taken into account that the polarisation should match, we can multiply the modulus of the field and the modulus of the antenna height to obtain the voltage. Of course, this simplification cannot be done for a noise model with directional dependence. The received voltage is now given by

$$V(\nu) = \sqrt{2\mathrm{Z}_0 \frac{\mathrm{k_B}\nu^2\delta\nu}{c^2} \int T(\theta,\phi)\ |\overrightarrow{l_{\mathrm{eff}}}(\theta,\phi)|^2\ \mathrm{d}\Omega} \tag{5.13}$$

Since the model used has the temperature to be independent of θ and ϕ, $T(\theta,\phi) = T$ can be taken out of the integral.

The amplitude extracted from the model has no phase information of the incoming noise. We can add random phases to the amplitude since the noise indeed behaves randomly.

$$V(\nu) = V(\nu) \times \exp(-i\varphi) \tag{5.14}$$

φ is a random number that is generated between 0 and 2π.

Finally, we can convert the amplitude to the time domain using Inverse Fourier Transform:

$$V(\nu) \longrightarrow V(t) \tag{5.15}$$

Naturally, Parseval's theorem should be satisfied in the frequency and time domains once these transformations are done. This can be utilized as a sanity check of this procedure. In this manner, the expected noise for a given frequency band

can be expressed as time traces. Of course, this is only an average behaviour of the noise. One can also assume variations in the extracted amplitude about this average noise. Such variations are not considered here since we are interested only in the average behaviour of the measurable noise.

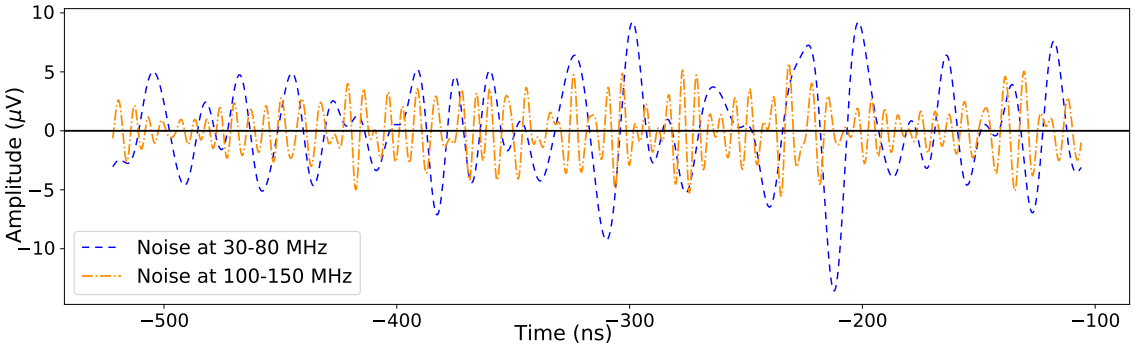

Figure 5.6: Time traces of the total noise (Galactic + thermal) generated at two different bands with equal bandwidths of 50 MHz. The time trace in the standard band 30-80 MHz is represented by the blue dashed curve. The time trace in the band 100-150 MHz is shown by the orange dotted-dashed curve. Both traces have a thermal noise of 300 K.

Figure 5.6 gives an example of such traces produced at two bands: 30-80 MHz and 100-150 MHz. It can be clearly seen that between these bands, with the same bandwidth of 50 MHz, the higher frequency band has lower noise. This is a direct consequence of the lower Galactic noise at higher frequencies.

In the following chapters, the total radio noise will be treated as described in this chapter. At all places, a thermal noise of 300 K is considered, unless otherwise specified.

5.4 Validation of the noise model

In order to cross-check the validity of the assumption of Galactic noise from Cane, the predictions are compared with the measured noise at AERA and Tunka-Rex sites. For this comparison, time traces of the measured noise are taken and the corresponding frequency spectra are obtained with Fourier transforms. This is done for data taken over 24 hours of time. The absolute values of these frequency spectra over one day's time are then averaged. By doing this, all Galactic contributions over the sidereal time of a day is taken care of, and averaged. This average noise in the frequency domain is compared to the Galactic noise predictions from the Cane model, which is also an averaged model. In order to make this comparison, the antenna responses of the respective antennas are included in the predicted noise (see equation 5.13). Along with the comparison in the frequency domain, the time traces of the measured noise and the predicted noise are also compared.

Figure 5.7 shows such a comparison for a sample of events for an LPDA antenna used at AERA [116]. The left panel shows the average frequency spectrum of 24 hours of noise measured with the blue curve. This average noise spectrum is seen to show distinct spikes. These correspond to the RFI at the site of the experiment, that have not been notch-filtered. The spectrum obtained after cutting out these RFI peaks is shown in red. The noise prediction from Cane, after including the response

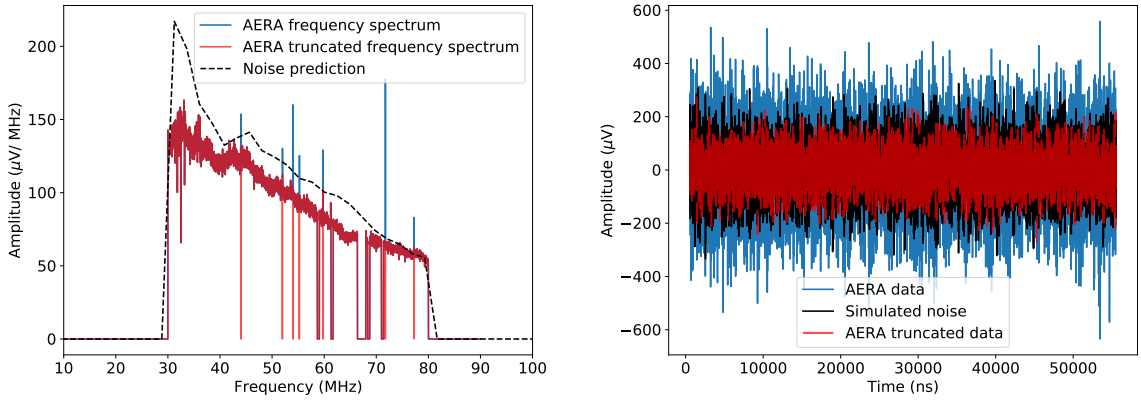

Figure 5.7: Cross-check of the noise treatment with AERA data (data from [116]).

of the LPDA antenna is given by the black dashed curve. We can see that the red curve agrees well with the predicted noise from Cane. A distinct spike at the low end of the frequency band is seen for the predicted noise. The absence of this in the measured spectrum (red curve) may be due to the effects of the high-pass filter. The predicted noise used a constant thermal noise of 300 K, which can explain the slight offset between the black curve and the measured red curve at frequencies less than $\approx$ 65 MHz. That is, the thermal noise over here for the LPDA can be slightly lower. Above 65 MHz, the measured and predicted curves match remarkably. This could be attributed to an actual thermal noise close to 300 K for the LPDA at these frequencies. Studies on the LPDA conducted at the Pierre Auger Observatory indeed confirms this behaviour of the thermal noise [117].

The time traces of the measured noise can also be compared with the predicted noise. This comparison is shown in the right panel of Figure 5.7. The raw data from AERA is represented by the blue time-trace. The black time-trace shows the predicted noise, obtained with the Cane model. Clearly, there is a difference in the amplitude of both the traces. However, an inverse Fourier transform of the truncated frequency spectrum (red curve in the left panel) can also be used for this comparison. This time trace is represented by the red curve in the right panel. We see that once the RFI noise is removed, the measured time trace also matches with the black curve, which corresponds to the predicted noise. Therefore, we can conclude that both the frequency-domain and time-domain comparisons show that the noise predictions of the Cane model agrees well with the average measurements of noise with the LPDA at the AERA-site.

A similar comparison is done for the noise measurement at the site of Tunka-Rex using the SALLA antenna [118]. Figure 5.8 shows this comparison. The right panel shows the frequency spectrum comparison. The solid red curve is the absolute value of the average measured frequency spectrum. This is compared to the predicted noise by Cane, shown by the black dashed curve. We see that the predicted noise is underestimated compared to the observed noise. Also shown are the curves corresponding to 2 times the prediction and $\sqrt{2}$ times the prediction. Close to the edges, the measured noise is 2 times the prediction, while at the middle of the measured band, it is closer to $\sqrt{2}$ times the noise prediction. This behaviour is expected since the SALLA antennas are in general noisy. It is known to have a

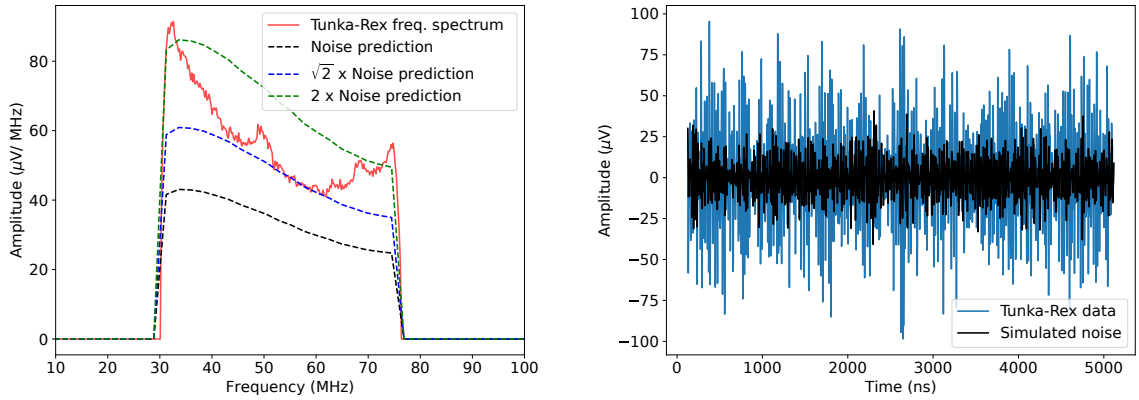

Figure 5.8: Cross-check of the noise treatment with Tunka-Rex data (data from [118]). The thermal noise of the SALLA antenna is more than the Galactic noise by a factor of $\sqrt{2}$ to 2. This causes the measured noise to lie between the green and blue dashed curves in the left panel.

large internal noise due to which the noise roughly increases by a factor of 2. The features of the SALLA antenna measured at the site of the Pierre Auger Observatory confirms that the thermal noise of the SALLA antenna is the dominant source of noise at all frequencies [117]. Therefore, the time traces of the measured noise (right panel of Figure 5.8) also have much larger amplitude than the prediction from the Cane model.

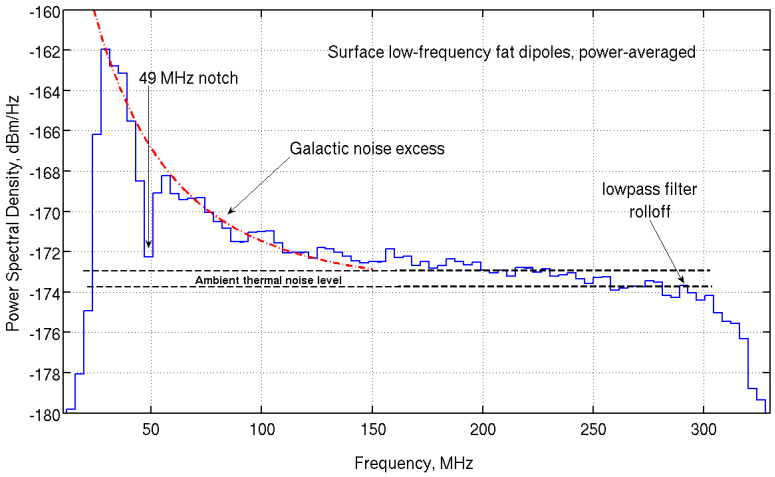

Figure 5.9: The power spectral density of the total noise measured by an ARA dipole antenna (measurements taken on the surface of the ice). The measured noise is compatible with the Galactic noise at frequencies below $\approx$ 150 MHz. Above this, the thermal noise is seen to dominate the total noise. The figure is shown in [24].

Measurements of the noise conditions done with the ARA dipole antennas at the South Pole also showed that a major portion of the noise can be described well by the Galactic noise predictions from the Cane model [24]. Figure 5.9 shows the total noise measured by ARA, along with a comparison to the expected level of Galactic noise. Therefore, with these three confirmations from three independent

experiments, we can safely use the Cane model for the purpose of this study.

5.5 Conclusion and remarks

The treatment of noise used in this study is explained in this chapter. The noise traces, containing Galactic and thermal components, generated by the method described here are used for further studies in this thesis. Once noise measurements at the South Pole are available, these can be included in the simulation scheme and can be compared with the simulated noise.

In this chapter, the thermal noise is considered to be constant at all frequencies. This is the simplest assumption that is possible. In reality, this depends on the antenna itself that is used for the measurement. A study conducted for AERA reports the fraction of the internal noise (thermal noise) that contributes to the total noise measured by three antennas: LPDA, Butterfly and SALLA [117]. This study reports the SALLA antenna to have the highest level of internal noise, which overpowers the Galactic noise in the entire band (22-82 MHz). This thermal noise for the SALLA antenna was seen to vary with frequency. For LPDA, the fraction of thermal noise is 25% at frequencies lower than 50 MHz, and is seen to exceed this fraction for frequencies higher than 50 MHz. The Butterfly antennas were seen to have low internal noise, and is nearly constant over the entire frequency range. New state-of-the-art antennas like SKALA has very low and nearly stable levels of thermal noise [108]. Between 50 MHz and 100 MHz, the thermal noise of this antenna fluctuates between 40 K and 60 K. From 100 MHz to 450 MHz, this antenna has a stable thermal noise of 40 K. Therefore, we can conclude that whether the thermal noise remains a constant or not varies from antenna to antenna. Nevertheless, it is safe to consider such a constant thermal noise for the purpose of our study.

CHAPTER 6

Frequency Band Studies for Lowering the Energy Threshold

This chapter mainly deals with the studies published in [107] [119] and [120].

The previous chapter described the noise considered for this study. Since we now understand the behaviour of noise, the behaviour of the radio signals from air showers can be looked at, in order to distinguish them from the noise. This chapter mainly deals with such a distinction between signal and noise by looking at signal-over-noise ratios to facilitate the observation of PeV showers.

6.1 Simulation of air showers and radio signals

In order to conduct the study, simulations of air showers and the resulting radio signals from them were done. The simulations were performed using CoREAS [65], which is the radio extension of CORSIKA [34]. CORSIKA generates the secondary particles produced by the air shower and CoREAS uses the distribution of these particles in the Earth's magnetic field to give the radio signals observed on ground as the final output. The radio output in the east-west (magnetic), north-south (magnetic) and vertical directions are obtained from CoREAS.

For a major part of this study, CORSIKA-7.4005 with hadronic interaction models FLUKA-2011.2c.2 and SIBYLL-2.1 [36] was used. Simulations produced for later studies used CORSIKA-7.5700 with SIBYLL-2.3 [121]. There was no significant change in the radio signal due to this (since the main difference between the versions is in the muonic content of the hadronic interactions). A total of 1579 simulations have been done for this study. The simulations used the atmosphere of the South Pole (South Pole atmosphere for Oct. 01, 1997 provided in CORSIKA as ATMOD 13) with an observation level of 2838 m above the sea level. The antennas were also placed at a height of 2838 m above sea level. The axis of the magnetic field at the South Pole is inclined at an angle of 18° with respect to the vertical, with an intensity of 55.2 μT. This is incorporated in the simulations. All the showers have been simulated using the thinning option (with a thinning level of 2.7×10^{-7}). A coordinate transformation between CORSIKA and IceCube coordinate system was necessary since the IceCube coordinate system is oriented based on the geographic North-South and the CORSIKA coordinate system is oriented based on the projection of the magnetic North-South on the ground. The antenna positions were rotated

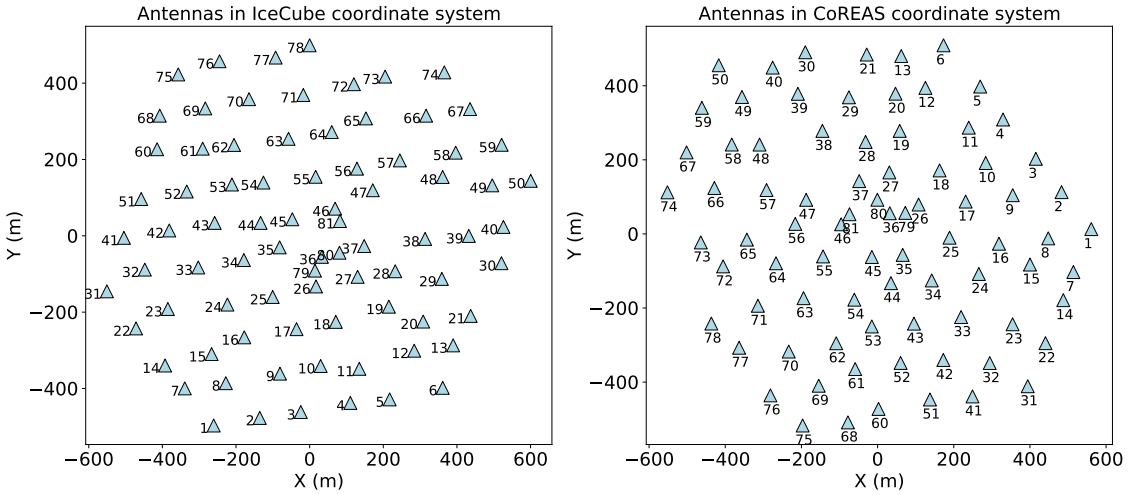

Figure 6.1: Simulated array of antennas in IceCube and CoREAS coordinate systems. A rotation by 119° is done to transform from IceCube to CoREAS system. The triangles represent the antenna positions, where one antenna is placed between the two Cherenkov tanks of each IceTop station.

by an angle of 119° for this transformation from IceCube to CORSIKA coordinate system.

Showers generated by gamma-ray primaries with energies ranging from 0.6-10 PeV are generated for the study of the radio signals. For initial studies, the azimuth angle was fixed to $\phi = 0°$ in CoREAS coordinate system. This resulted in the shower axis being oriented anti-parallel to the Magnetic North. This setting gives a geomagnetic angle (angle between the shower axis and the magnetic field) of 79° for a shower with a zenith angle of 61°. The zenith angle is fixed to 61° for a major portion of the simulations since this is the inclination of the Galactic Centre at the South Pole. The core position was set at the centre of the IceTop array, i.e. at (0,0) for majority of the simulations. Also, for comparison purposes, proton showers with the same settings were simulated.

The simulated antenna array consisted of 81 antennas, each located at the centre of an IceTop station [28]. This array had an average antenna spacing of around 125 m. A much more densely spaced inner infill array of antennas is also simulated with a spacing of approximately 90 m. Such infill stations are present for the IceTop stations also. The entire array covers an area of around 1 km^2. A schematic of the antenna positions in both IceCube and CoREAS coordinate systems is shown in Figure 6.1.

The signals obtained from CoREAS (μV/m) are then folded through the response of an antenna which gives the signal in units of μV. This is now the signal that is generally measured at the antenna foot-point in experiments. The antenna used in this study is a simple half wave dipole antenna with a resonance at 150 MHz which was simulated using NEC2++ [122]. For more details see Appendix B. The signals from the east-west and north-south components are considered to be the entire signal measured by the antenna. Here, the z-component is neglected since most of the antennas in air-shower experiments do not measure the z component. Also, for the South Pole, the small angle between the magnetic field and the vertical, produces a smaller z component of electric field as compared to the x and y components, even

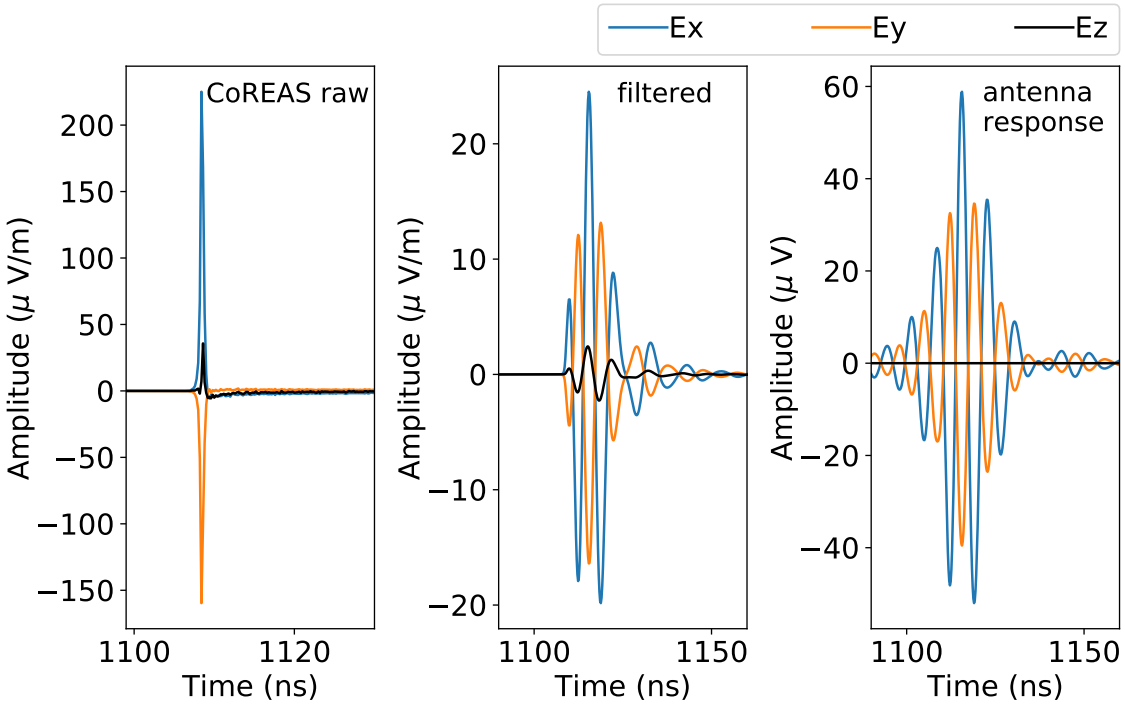

Figure 6.2: The signal chain (for pure radio signals from air showers) used in the simulations for an example antenna for a sample shower with $\theta = 61°$ and $\phi = 36°$. The left panel shows the raw CoREAS signal, the middle panel shows the filtered signal (here 100-190 MHz) and the right panel shows the signal after applying the antenna response. Note the different scalings on the y-axis.

for the air showers with high inclination. An example signal that is produced by this simulation chain is shown in Figure 6.2.

6.2 Signal behaviour

Before comparing the radio signals to the expected noise, it is necessary to understand the nature of the radio signals from air showers that is expected at the South Pole. A typical way of inspecting the signals from a shower is by the inspection of the lateral distribution. This shows the spatial variation of the signal received by the antenna array. Figure 6.3 shows the different simulated amplitudes delivered to 81 antennas, where the antennas are placed as shown in Figure 6.1. The amplitudes received by such an array from gamma ray and proton induced showers are shown. The zenith angle is fixed to $61°$ and the azimuth to $0°$ ($\alpha = 79°$). For illustration purposes, the frequencies are split into bands with a width of 70 MHz each, and range from 30 MHz to 380 MHz. The proton showers have lower amplitudes than gamma-ray showers since they have lower electromagnetic content. The plot shows the mean amplitude along with the spread about the mean with 30 simulated showers for gamma ray and proton primaries. It can be seen that the lateral distribution for these showers change when the observation frequency is varied. At frequencies above 100 MHz, we start to see the Cherenkov ring at distances close to 100-200 m. At very high frequencies like those above 300 MHz, the emission becomes extremely localised, giving non-zero values of the amplitude only on the Cherenkov ring.

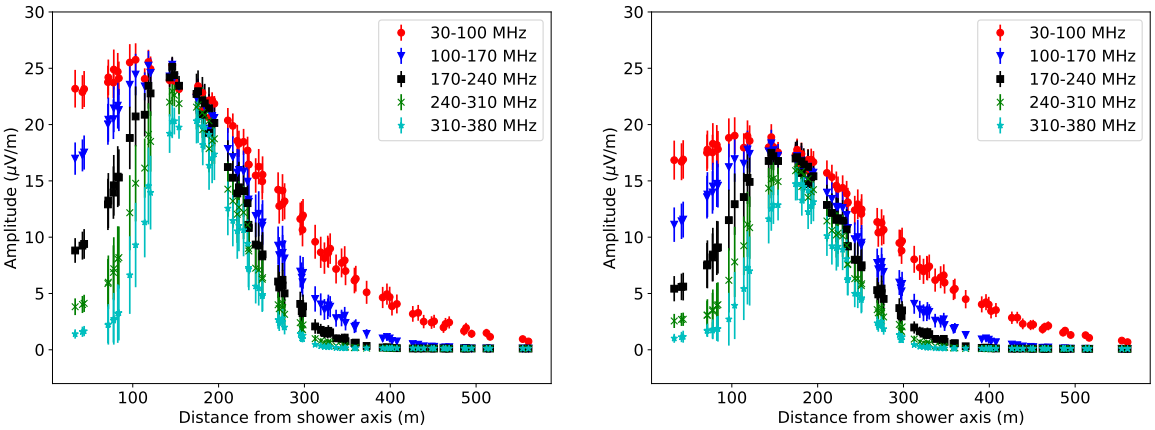

Figure 6.3: Lateral distribution of radio signals (without noise) obtained from simulations for 10 PeV gamma-ray (left panel) and proton (right panel) showers with $\theta = 61°$ and $\alpha = 79°$. The amplitudes are filtered to bands with a width of 70 MHz and range from 30 MHz to 380 MHz.

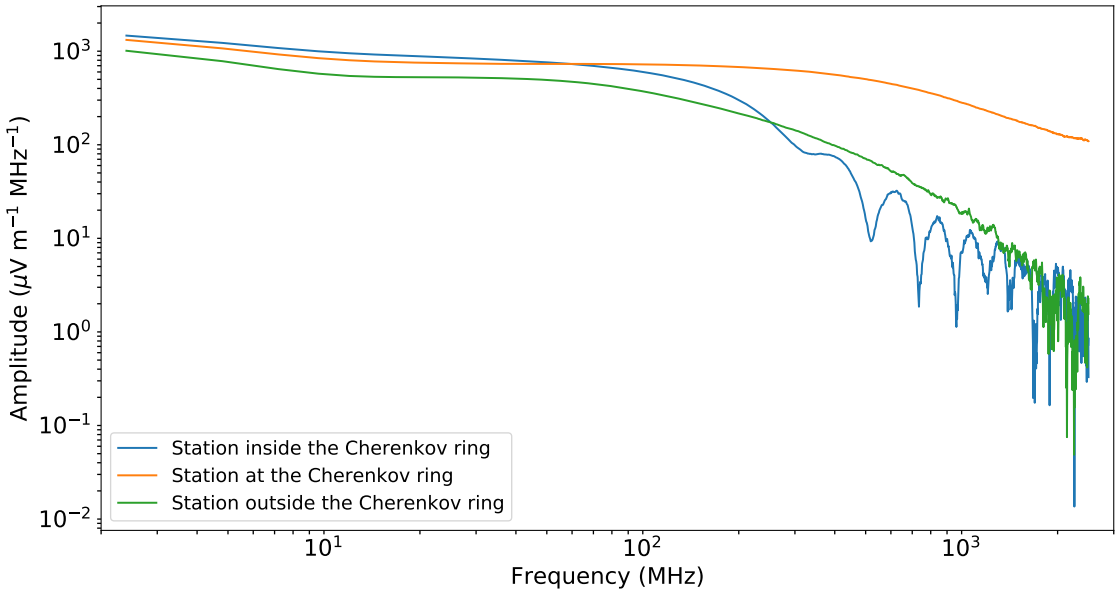

Figure 6.4: Frequency spectrum of the emission of radio signals at different positions. Here, the emission is shown for a gamma-ray shower of 61° zenith angle.

That is, the radio signal dies out gradually at every other location at such high frequencies.

This is also clearly seen in Figure 6.4 which shows the signals at three antenna positions in the array: one inside the Cherenkov ring (station number 80, distance to axis ≈ 45 m), one at the Cherenkov ring (station number 55, distance to axis ≈ 146 m) and one outside the Cherenkov ring (station number 21, distance to axis ≈ 236 m). The figure shows such a spectrum for a shower produced by a gamma ray of $\theta = 61°$. For a shower with a different zenith angle, the distances at which signals with such spectra can be seen will be different.

It is clear from Figure 6.4 that at the Cherenkov ring, the signal is nearly constant

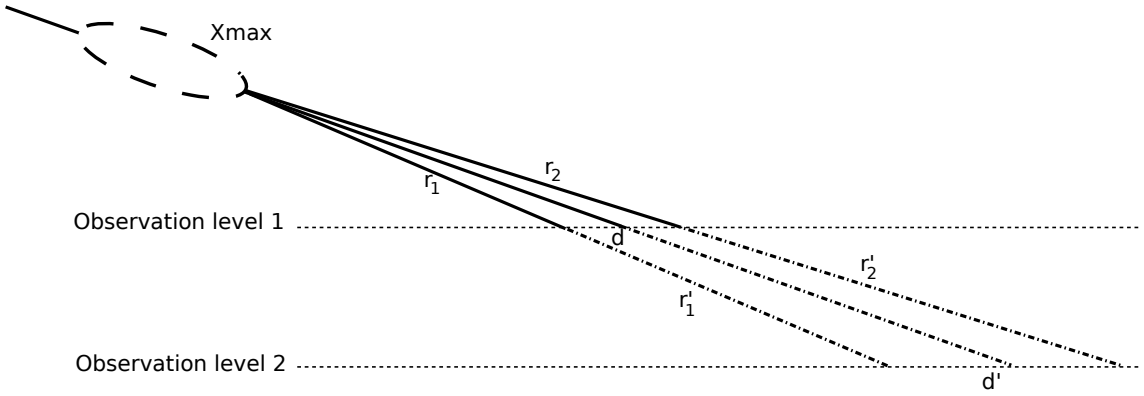

Figure 6.5: Illustration of the effect of the observation level on the early-late effect for inclined showers. Observation level 1 is closer to the shower maximum than observation level 2. Due to its relative proximity, the difference in the amplitudes at the ground level at distances r_1 and r_2 is low. The same amplitudes will acquire non-negligible differences between the positions r_1' and r_2', at observation level 2.

and coherent throughout the entire frequency range that is shown in the figure (a few MHz to a few GHz). The nature of the signal inside and outside the Cherenkov ring is different. In these regions, the signal goes down at higher frequencies. That is, the signal is fairly constant up to 100 MHz, and beyond this the amplitude starts decreasing. The fluctuations at very high frequencies arise due to numerical noise in the simulations. The net radio signal for a wide frequency band (e.g. 50-350 MHz) at any distance is the result of a direct additive effect of the amplitudes at all the underlying frequencies.

In Figure 6.3, the asymmetries in the lateral distribution due to the early-late effects of radio emission is negligible. The early-late effect arises because the part of the shower closer to the ground reaches the antennas earlier than the part of the shower farther away from the ground. This effect is seen only in inclined air showers. For such inclined air showers, if the observation level is high, this geometrical affect is not noticeable in the signals on the ground. This is illustrated in Figure 6.5. For the same shower, Observer level 1 will have smaller differences in the amplitude ($\propto r^{-1}$) at the early and late part of the shower on the ground when compared to Observer level 2. Since the South Pole is at an observation level of 2835 m above sea level, it has no significant early-late effect (especially for the zenith angle of interest) and therefore, this is not seen in the lateral distribution in Figure 6.3. For comparison, the Pierre Auger Observatory is at an observation level of $\approx$ 1600 m above sea level, and will therefore see the early-late effect for inclined showers, as described in [123].

6.3 Comparison of signal and noise

The signals obtained from CoREAS are filtered to the desired frequency bands before applying the antenna response. This response is applied in the frequency domain. The resulting signal in units of $\mu\mathrm{V/MHz}$ is passed through an inverse Fourier transform to obtain the time series signal. This process is done for all the 81 antennas in the array.

Signals extracted like this can be compared with time traces of noise produced as described in chapter 5. Here, the signals used for such an initial comparison are those of a gamma-ray shower of 10 PeV energy and inclined at an angle of 61°. A comparison of the signal time traces to the time traces of the noise is shown in Figure 6.6. For the purpose of such a comparison, we look at the quantity signal-to-noise ratio (SNR), defined over here as

$$\mathrm{SNR} = \frac{S^2}{N^2} \tag{6.1}$$

where S is the maximum of the Hilbert envelope of the signal and N is the rms noise in the specified frequency band. The amplitude of the Hilbert envelope provides the magnitude of the analytic signal. This gives a smooth curve that follows the extremes of the signal [124]. From air-shower experiments, we know that if the SNR value is greater than 10, it will be possible to detect this signal, for externally triggered antenna arrays [125] (self-triggered arrays typically have a higher threshold). Therefore, SNR > 10 is the condition for detection within the context of this thesis.

The signal and noise traces are filtered to 30-80 MHz in the left panel of Figure 6.6. This is the frequency band used for measurement by most of the air-shower experiments. This gives an SNR value of ≈ 35 for an antenna at a distance of 107 m from the shower axis (station 54). This is an antenna that lies at the Cherenkov ring. The right panel shows the case when the antenna is filtered to the band 50-350 MHz. This is the frequency band of operation for the Square Kilometre Array (SKA) in Australia [126]. In this band, the signal is considerably amplified and the noise level is also lower than that in 30-80 MHz. This results in a higher level of SNR (≈ 1055).

Thus, it is clear that the signal-to-noise ratio improves considerably as we move to higher frequencies, as is expected from the behaviour of the Galactic noise. The suppression of the Galactic noise beyond 150 MHz is visible in the time traces of the noise. It becomes obvious that moving on to higher frequencies will enable us to have a higher level of signal-to-noise ratio (SNR), provided the antenna falls within the footprint of the shower. This is especially the case for the antennas that fall on the Cherenkov ring.

Although it is clear from Figure 6.6 that using frequency bands that are higher than the standard band (30-80 MHz) will help us in enhancing the signal-to-noise ratio, the exact band that should be used for maximising the chances of observation still has to be investigated. The following section addresses this issue and is focused on finding the optimal frequency band for radio measurements of air showers.

6.4 Optimising the observing frequency band

As discussed in the previous section, the usage of higher frequencies will enable us to improve the SNR considerably. Despite this knowledge, the optimal band that gives a high level of SNR throughout the entire antenna array has to be investigated. It is intuitive that using really large frequency bands may not help in obtaining a high SNR throughout the antenna array. This is because, cutting to frequency bands that are too wide may cause an excess of noise to appear in the time trace; especially at high frequencies, we are just adding on a constant thermal noise. On the other hand, the signal strength starts declining remarkably at frequencies above 200 MHz

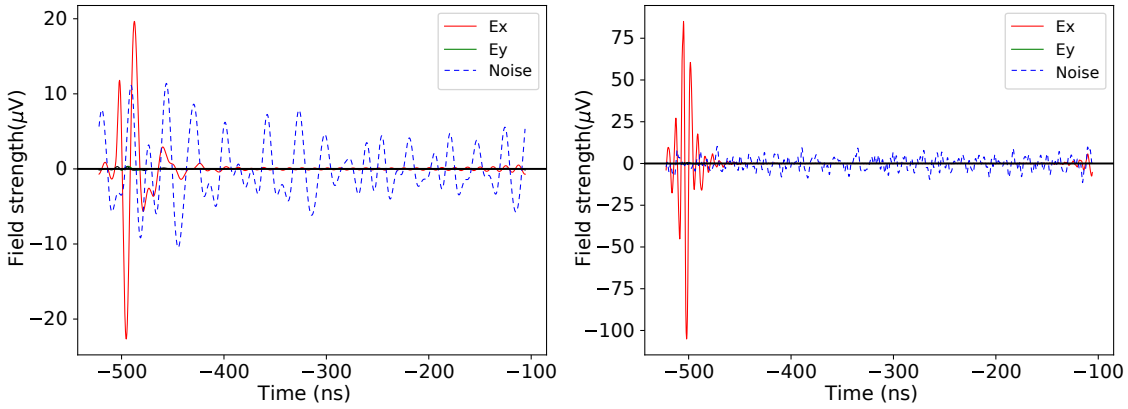

(a) 30-80 MHz, (SNR ≈ 35)

(b) 50-350 MHz, (SNR ≈ 1055)

Figure 6.6: The signal and noise simulated for a station located on the Cherenkov ring, with a distance of 107 m from the shower axis. The signal-to-noise ratio is much higher at 50-350 MHz than at 30-80 MHz. Here, the shower is oriented in such a manner that there is only the Ex component. The Ey component is almost negligible for this orientation of the shower.

at regions other than that of the Cherenkov ring (see Figure 6.4). Thus, a balance has to be found between the two.

Experimentally, we can indeed take measurements in wide-band frequencies, and thereafter filter into the required frequency range digitally. But this will increase the cost of the experiment considerably. The usage of higher frequencies will require a greater sampling rate (Nyquist law) and hence will require a better communication facility, memory, ADC, etc. Therefore, here, we conducted a detailed study to estimate the frequency range that will give a maximum signal-to-noise ratio (and thereby maximise the detection probability).

In order to study the SNR in the entire array, we inspect three regions of the shower footprint. These are the areas on the Cherenkov ring, inside the Cherenkov ring, and outside the Cherenkov ring. For maximising the probability of detection in the entire antenna array, it is desirable to have a high value of SNR in all of these regions. Therefore, the SNR in each individual region is closely studied. Of course, for an array with an average spacing of 125 m, it is not so crucial to have signal in the antennas outside the Cherenkov ring, for inclined showers. It is much more important in the case of arrays with much larger spacing, e.g. GRAND [23] or the upgrade of the Pierre Auger Observatory [86].

The SNR is studied in all of the possible frequency bands that can be used for the measurement of air showers. A gamma-ray shower with an energy of 10 PeV and with a zenith angle of 61° is used for this. For this, a heat map of the SNR in different frequency bands is made. The frequencies for the heat map range from 30 MHz to 150 MHz for the lower edge of the frequency band and from 80 MHz to 350 MHz for the upper edge of the band. Such a scan is made for antenna stations at each region mentioned above. Stations 45, 54 and 33 are chosen as example stations for the regions studied here. The resulting values of SNR in all the considered bands are shown in Figure 6.7.

The x-axis in the figure shows the lower cutoff frequency of each frequency band

and the y-axis shows the upper cutoff frequency of each band. That is, each cell denotes a frequency band where its lower cutoff frequency is that shown on the x-axis and the upper cutoff frequency is that shown in the y-axis. The obtained SNR in this band is then filled in as a colour scale in this cell. In the figure, the left panels show the SNR obtained when the thermal noise level is 300 K. For comparison, SNR at these frequencies when the thermal noise is low (40 K) is also shown in the right panels, for the same antennas.

From the left panels in Figure 6.7 we can see that the typical frequency band of 30-80 MHz (lower left bins in Figure 6.7) is not ideal for obtaining an optimal level of SNR. The brightest bins in the figure show the ideal frequency band with a maximum value of SNR. Such bright bins are seen for all of the studied regions of the shower footprint. Here, all the bands where a value of SNR less than 10 is obtained are set to the colour white, since this is the typical threshold for detection in an individual antenna station [125].

We can see that taking measurements at frequencies like 100-190 MHz gives a higher SNR. This is the case for all the three regions of the shower. This means that taking measurements in this frequency band will improve the SNR in the entire array. Also, such bands with high SNR become especially crucial, when the energy threshold is attempted to be lowered.

The optimal band remains the same, viz. 100-190 MHz, when the thermal noise level is low (here 40 K). The right panels of Figure 6.7 show the SNR in all the considered frequency bands for antennas 45, 54 and 33 when the thermal noise is 40 K. The major difference seen, when compared to the higher thermal noise case, is that the upper cutoff frequency can be extended to frequency values higher than 190 MHz with no loss in SNR. The optimal lower cutoff frequency essentially remains the same. This is intuitive from Fig. 5.5 as the cross over between thermal and galactic noise components occurs at around 320 MHz for the low thermal noise case. Since the signal also has not completely diminished at this frequency, the SNR is considerably good for these bands (starting from 100 MHz and going to frequencies up to 320 MHz). In the low thermal noise case, the scale of SNR also obviously increases, since the noise level is lower here.

A map of the SNR that is measurable by all the antennas at the optimal frequency band of 100-190 MHz is shown in Figure 6.8a. This was produced by running a CoREAS simulation in parallel mode with 3750 closely spaced antennas using the hadronic interaction model UrQMD instead of FLUKA for the low energy interaction. The black dots represent the 81 antennas considered in the simulations. The antennas considered for the frequency band scan in Figure 6.7 are also marked here. The star shape shows station 54, the pentagon station 45, and the square station 33.

Figure 6.8 also shows the footprints at the bands 30-80 MHz and 50-350 MHz for the same shower, in units of the SNR. It is clear that overall, the SNR rises considerably as we use the optimal frequency band. Even though the band 50-350 MHz has higher SNR at certain areas than 30-80 MHz, it still has a lesser overall SNR than the optimal band. This is due to the higher amount of noise included in this band from both Galactic noise at lower frequencies and the constant thermal noise at higher frequencies.

Such a scan of the frequency bands done for other primaries or other zenith angles also reveals 100-190 MHz as the optimal band. There is only a variation in the scaling of SNR as these parameters change. This results from the change

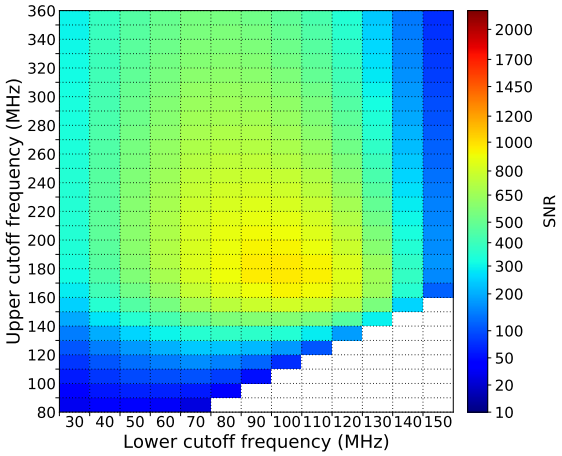

(a) Inside the Cherenkov ring (distance: 34 m), $T_{\mathrm{therm.}}$ = 300 K

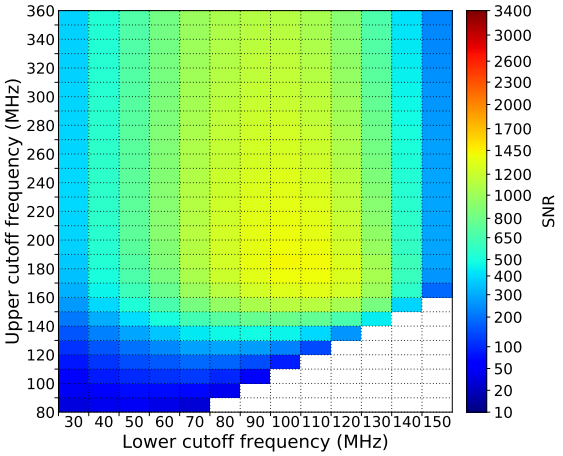

(d) Inside the Cherenkov ring (distance: 34 m), $T_{\mathrm{therm.}}$ = 40 K

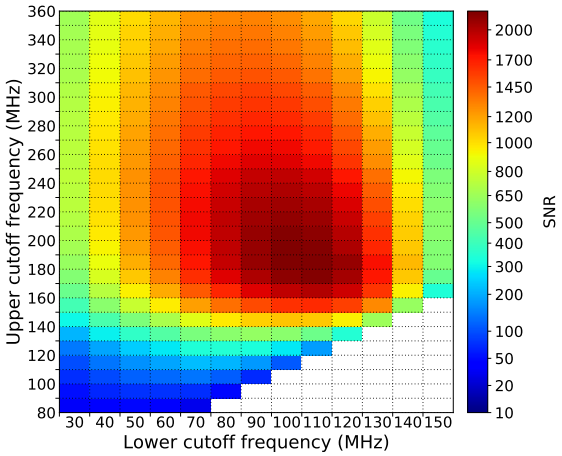

(b) On the Cherenkov ring (distance: 107 m), $T_{\mathrm{therm.}}$ = 300 K

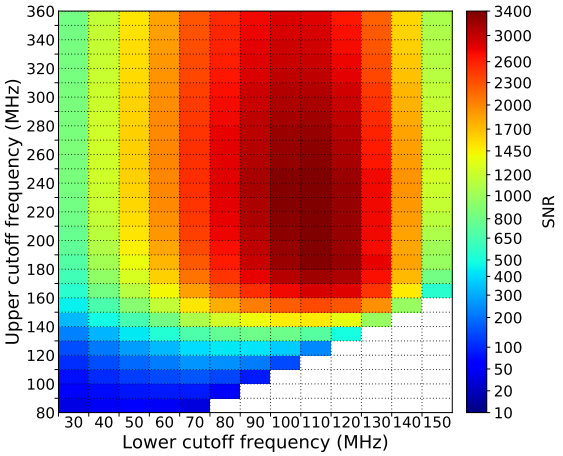

(e) On the Cherenkov ring (distance: 107 m), $T_{\mathrm{therm.}}$ = 40 K

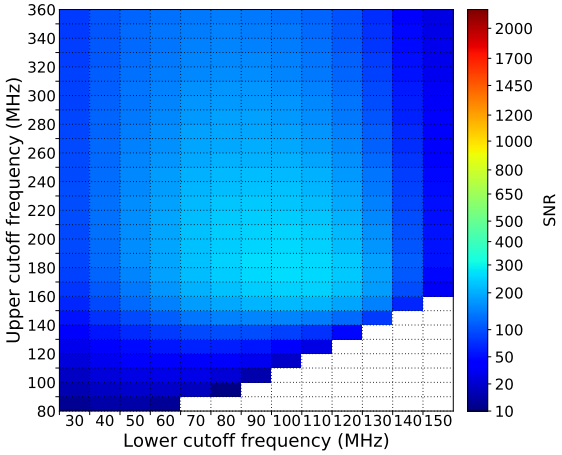

(c) Outside the Cherenkov ring (distance: 246 m), $T_{\mathrm{therm.}}$ = 300 K

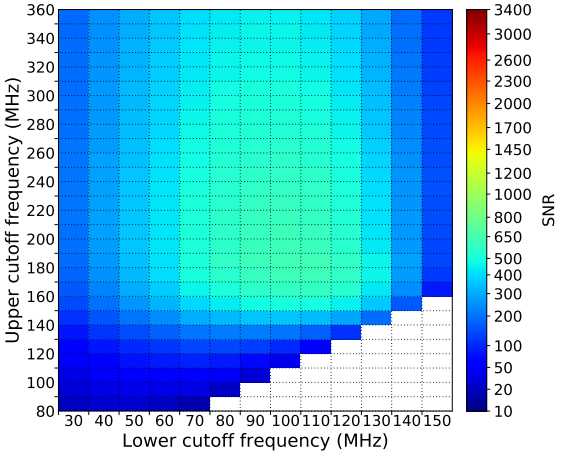

(f) Outside the Cherenkov ring (distance: 246 m), $T_{\mathrm{therm.}}$ = 40 K

Figure 6.7: SNR seen in a typical antenna inside, on and outside the Cherenkov ring respectively, at various frequency bands, for one typical shower induced by a 10 PeV gamma-ray primary with zenith angle = 61° and α = 79°. The left panels represent the SNR when the thermal noise is 300 K and the right panels show the SNR for the same antennas with thermal noise 40 K. Please note the different scaling of the colour bars for both cases.

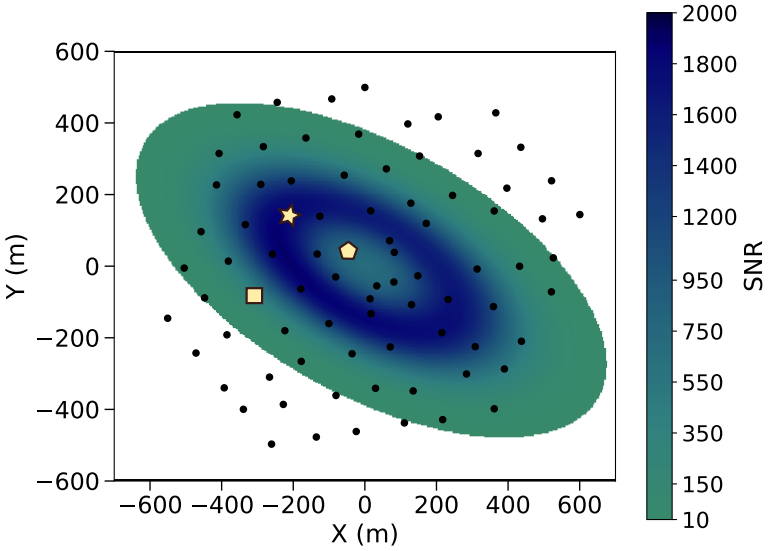

(a) 100-190 MHz

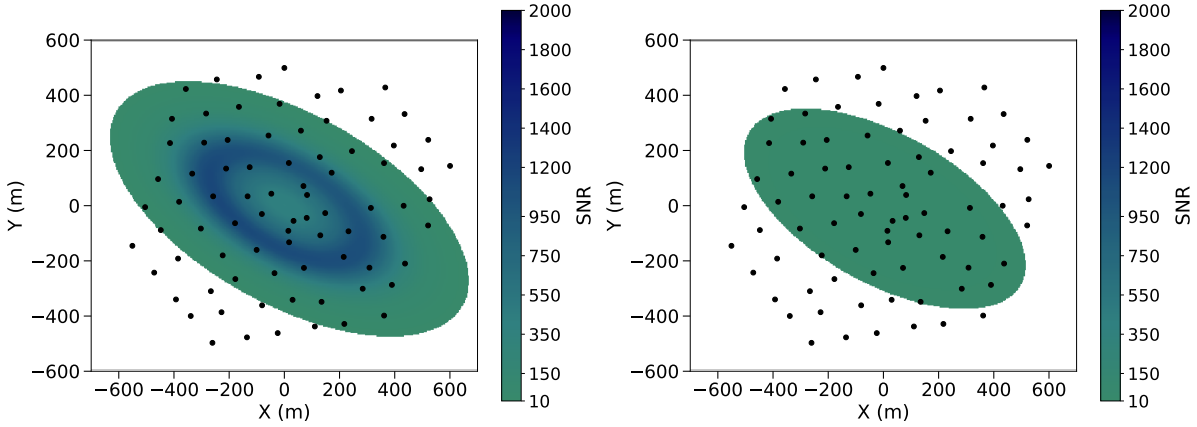

(b) 50-350 MHz

(c) 30-80 MHz

Figure 6.8: SNR map of a 10 PeV gamma-ray shower ($\theta = 61°$) at (a) 100-190 MHz, (b) 50-350 MHz and (c) 30-80 MHz. The black dots represent the 81 antenna positions. In (a) the antenna on the Cherenkov ring used for the frequency band scan is shown by the star shape. The square shape represents the antenna outside the Cherenkov ring and the pentagon that inside the Cherenkov ring.

in the total electromagnetic content (for different primary type) and the different spread of the signal strength on the ground (for different zenith angle). There is a direct correlation between the spread in the diameter of the Cherenkov ring and the inclination of the shower. For illustration, an example of a frequency band scan for an antenna (station 45) which receives a shower from a proton of 60° inclination is shown in Figure 6.9. Also shown in the figure is the frequency scan for station 11 for a gamma-ray shower with an inclination of 70°.

The observed signal-to-noise ratio in the antennas will depend on the energy of the shower, the zenith angle, and the azimuth angle (resulting in varying values of the Geomagnetic angle). The study of SNR in these parameter spaces is described

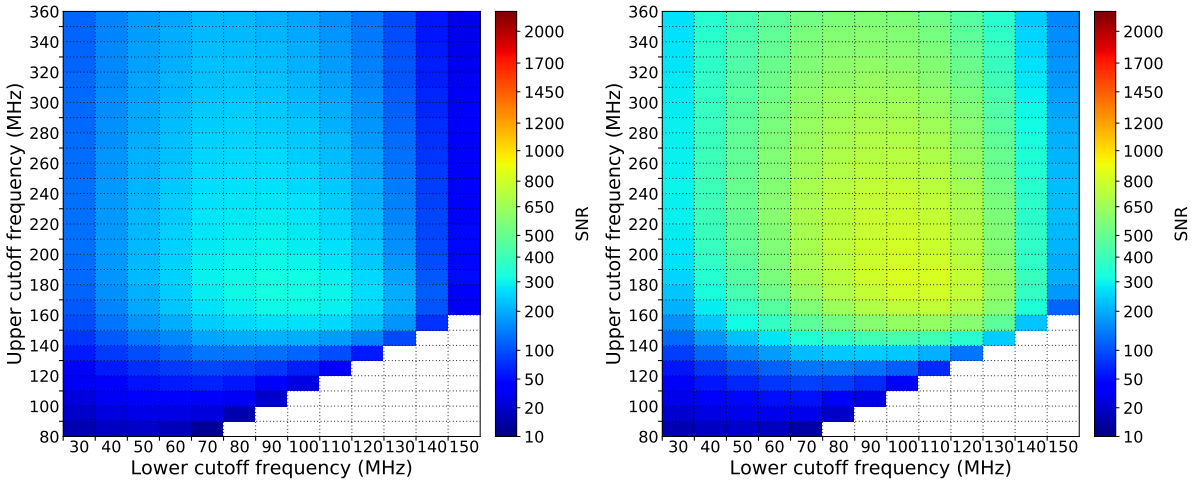

(a) proton, $\theta = 60°, \phi = 0°$, E = 10PeV (b) gamma ray, $\theta = 70°, \phi = 0°$, E = 10PeV

Figure 6.9: Frequency band scan for (a) station 11 for a proton shower and for (b) station 45 for a shower with zenith angle = 70°. The optimal band with maximum SNR is consistent (100-190 MHz) for different primary particles or for different zenith angles.

in the following sections. The variation of the SNR with respect to the changing position of the shower maximum is not taken into account over here.

6.4.1 Dependence on the zenith angle

As discussed earlier, the SNR varies with the zenith angle due to the varying spread of the signal on the ground plane as the inclination changes. This SNR at different zenith angles are shown in Figure 6.10. This evolution of SNR is looked at for antenna stations at various perpendicular distances to the shower axis (which is equivalent to the radial distance of the antennas to the shower axis in the shower plane). Figure 6.10 shows the SNR for the 81 antenna stations for zenith angles ranging from 0° to 70°, for the bands 30-80 MHz, 100-190 MHz and 50-350 MHz. The left panel depicts this for gamma-ray showers of 10 PeV and azimuth angle 0° and the right panel shows proton showers with the same parameters. Like before, an SNR less than 10 implies that the signal will not be detectable and hence this antenna is set to the colour white. Each zenith bin shows one typical shower with the given parameters.

For the standard band of 30-80 MHz, the signal-to-noise ratio is significantly lower than that for the bands 50-350 MHz and 100-190 MHz at all zenith angles. The band 50-350 MHz is comparatively better than 30-80 MHz, and also is able to observe the Cherenkov ring. Nevertheless, the highest level of signal-to-noise ratio is obtained with the band 100-190 MHz for all zenith angles, as expected. This is the case for both proton and gamma-ray primaries.

For showers of greater inclination, the usage of the higher frequency bands are particularly advantageous. If we look at the final θ bin containing a shower with zenith angle 70°, it can be seen that the SNR at 30-80 MHz is at the limit (SNR $\approx$ 10) for gamma-ray showers. Proton showers of energy 10 PeV and zenith angle 70° will

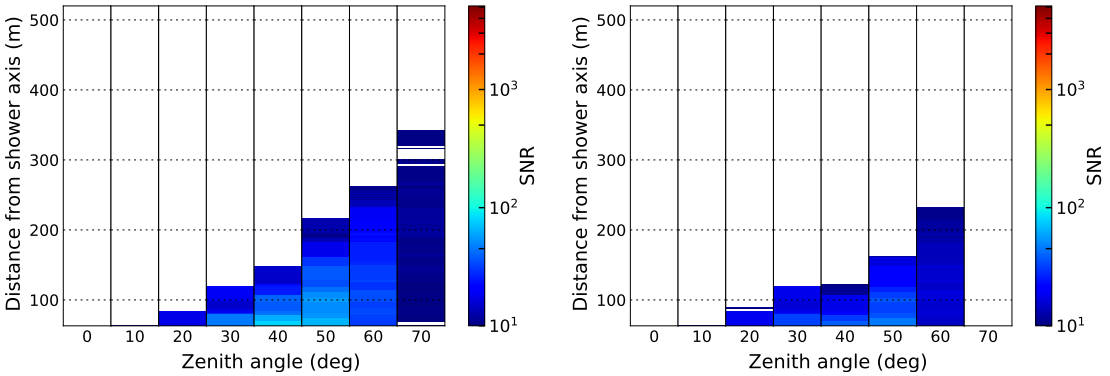

(a) 30-80 MHz

(d) 30-80 MHz

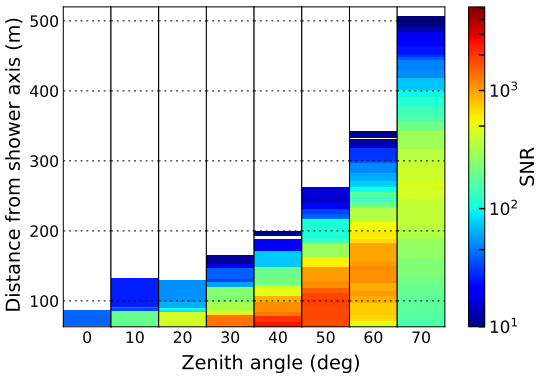

(b) 50-350 MHz

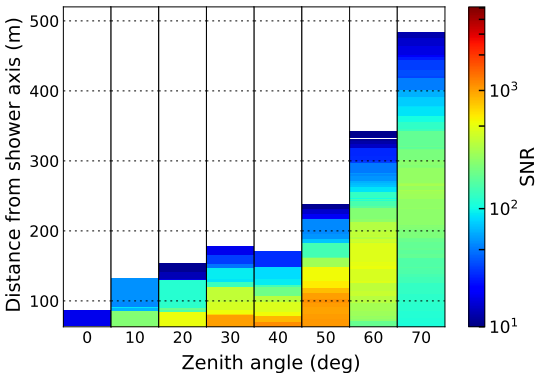

(e) 50-350 MHz

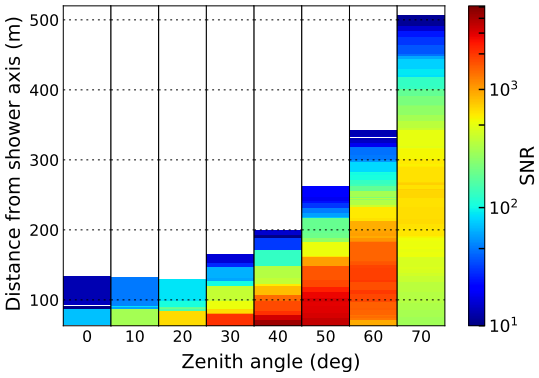

(c) 100-190 MHz

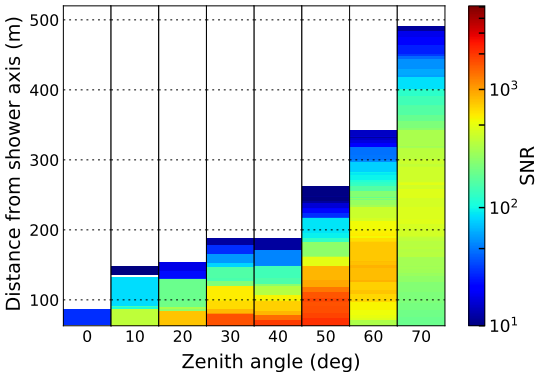

(f) 100-190 MHz

Figure 6.10: Zenith angle dependence of the SNR for showers produced by 10 PeV primary gamma rays (left panels) and protons (right panels) with $\phi = 0$. Each bin contains a typical shower for the respective zenith angle. At $\theta = 70°$ the shower illuminates almost the entire array at the higher frequencies.

not be seen at all in the band 30-80 MHz since they will have an SNR lower than 10. The same proton shower can however be observed if the higher frequency bands like 50-350 MHz or 100-190 MHz (with the highest level of SNR) are used.

The bright regions seen for $\theta > 30^{\circ}$ are the areas where the Cherenkov ring falls on the antennas. These can be seen for the higher frequency bands and are more visible in the inclined showers. Due to the nearly constant opening angle of the Cherenkov ring, the radius of the Cherenkov ring on the ground becomes larger as the shower maximum is farther from the ground. Hence, the distance from the shower axis to the Cherenkov ring changes as the shower becomes more inclined. This is evident from the propagation of the Cherenkov ring signature in the figure. For an observation level of 2835 m above sea level, the average distance at which the Cherenkov ring falls is $\mathrm{d_{Ch}} \approx 250$ m for a shower of zenith angle 70° and is $\mathrm{d_{Ch}} \approx 150$ m for a shower of zenith angle 60°.

At lower zenith angles, a major part of the shower is lost because of clipping effects. If the observer level is situated before the complete radiation energy from the shower is developed, the shower is said to be ''clipped''. This results in a non-observation of the entire shower signal that could potentially be seen at lower observation levels [127]. The high observation level at the South Pole (2835 m) is the reason for the showers getting clipped off. The distance to the shower maximum at the lower zenith angles is about a few kilometres, while that for showers of 70° inclination is in the order of tens of kilometres. That is, for the lower zenith angles, the observation level is closer to the shower maximum, rendering the total radio emission from the shower to be under-developed. This is also the reason for the appearance of the Cherenkov ring only for zenith angles $\gtrsim 30^{\circ}$.

Figure 6.11 shows the longitudinal distribution of a 10 PeV gamma-ray shower and the observation levels at the South Pole when the shower is arriving at various zenith angles. The total energy fluence of the radio signal at the ground increases up to the zenith angle where clipping effects are no longer observed. The shower maximum is located close to a depth of 650-690 g/cm^2. This causes the vertical showers to be clipped since the observation levels are close to 720 g/cm^2 as shown in the figure. For 10 PeV showers the radiation energy is completely developed and the the total radiated energy does not get clipped-off for zenith angles above 50°. At zenith angles greater than 50°, the total energy in the radio footprint remains nearly the same, but the area on the ground increases. This results in a lower power per unit area on the ground, causing a decrease in the observed SNR. The relatively lower signal-to-noise ratio for the 70° shower in Figure 6.10 as compared to the 60° shower is an effect of this.

The distances of the antennas from the shower axis fall within the range of 50 m to approximately 520 m for the configurations given in Figure 6.10. Only the antennas with a SNR > 10 can detect these showers. The antennas with distances of ≈ 100 meters are able to satisfy this condition for vertical showers. For inclined showers, these are the antennas that are even as far away as 500 m. Therefore, this range corresponds to the required minimum spacing to detect these showers. This implies that the array spacing of the antennas should at least be of 100 m for vertical showers. In the case of inclined showers with $\theta \gtrsim 60^{\circ}$ a spacing of 300 m is sufficient to achieve a threshold of 10 PeV at the South Pole.

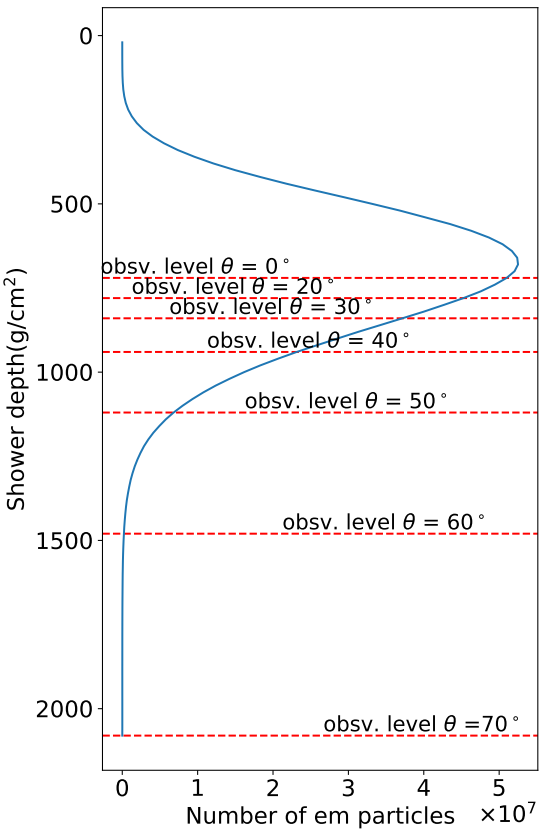

Figure 6.11: Longitudinal development of the electromagnetic components (e^+, e^-, γ) of an example gamma-ray shower of 10 PeV energy. The shower depths at which the observation level is located for showers of different zenith angles are indicated. The more inclined the shower is, the later is the stage at which the antennas observe the shower. Hence, at high inclinations the shower is fully developed by the time it reaches the antennas.

6.4.2 Dependence on the azimuth angle

To investigate the variation of SNR with the azimuth angle, simulations of 10 PeV gamma rays with angles ranging from -180° to 180° were done. As the azimuth angle changes it results in a change in the geomagnetic angle. At the South Pole, the magnetic field is inclined to the vertical direction by 18°. Therefore, a shower of zenith angle 61° changes its geomagnetic angle from 43° to 79° as the shower spans the entire azimuth angle range. This leads to an amplitude variation by a factor of $\frac{\sin(43°)}{\sin(79°)} = 0.7$. Figure 6.12 shows these simulated showers with 12 bins in the azimuth. These showers are filtered to the optimal band of 100-190 MHz. One typical shower with the given parameters is used in each azimuth bin for this study.

It can be inferred from Figure 6.12 that a change in the azimuth angle does not have a large impact on these showers. The strength in SNR does not change drastically as ϕ changes. To estimate the average change in SNR as the azimuth changes, the maximum value of the SNR for each shower is taken. The mean value of the maximum SNR is found to be 1518 for these showers. The maximum value of the SNR varied with a standard deviation of $\sigma_{\mathrm{SNR}} = 264$. That is, with changing azimuth angle there is a variation in the maximum value of the SNR by 17.4% about

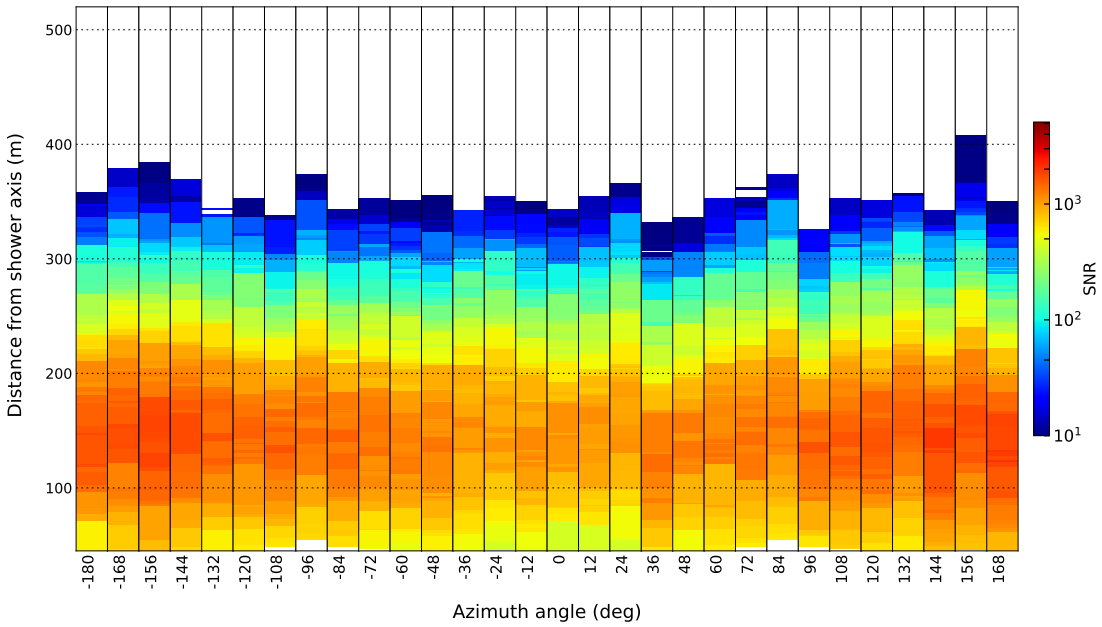

Figure 6.12: Azimuth angle dependence of the SNR for 10 PeV gamma-ray showers with zenith angle fixed to 61°. The figure shows a typical shower in each bin. The variation in the distance arises due to shower-to-shower fluctuations and azimuth angle variations.

the mean. This is the variation for the sample showers used for the study on the azimuth. On top of this, there is also a variation of the amplitude at a fixed azimuth angle due to shower-to-shower fluctuations which comes to 3.7% on an average. This will be further discussed in section 6.4.3.

We can conclude that for inclined air showers at the South Pole, there is not a strong variation of the signal-to-noise ratio as the azimuth angle varies. This is also expected to be the same for more vertical showers since the magnetic field is only having a slight inclination at the Pole, causing the azimuth dependence of the showers to be nearly uniform at all zenith angles. Thus, it is justified to study the effects of other parameters at one particular azimuth angle.

6.4.3 Dependence on the primary energy

The signals that are observed by the antennas scale with the energy of the primary particle. The SNR becomes weaker as the energy of the primary particle decreases. Also, protons produce lower levels of SNR on the antennas, for the same energies as the gamma rays, due to their smaller electromagnetic content.

The signal-to-noise ratio of showers with gamma-ray and proton primaries with energies ranging from 1 PeV to 9 PeV, are shown in Figure 6.13. These are showers with zenith angles of 61°, 40° and 70°, and are filtered to the band 100-190 MHz. One typical shower of the given energy is plotted in each x-axis bin in the figure. Again, antennas with SNR < 10 are set to the colour white. Certain antennas with white colour (SNR < 10) in between the shower are seen for some showers. Such cases arise due to fluctuations in the signals that arrive at the antenna.

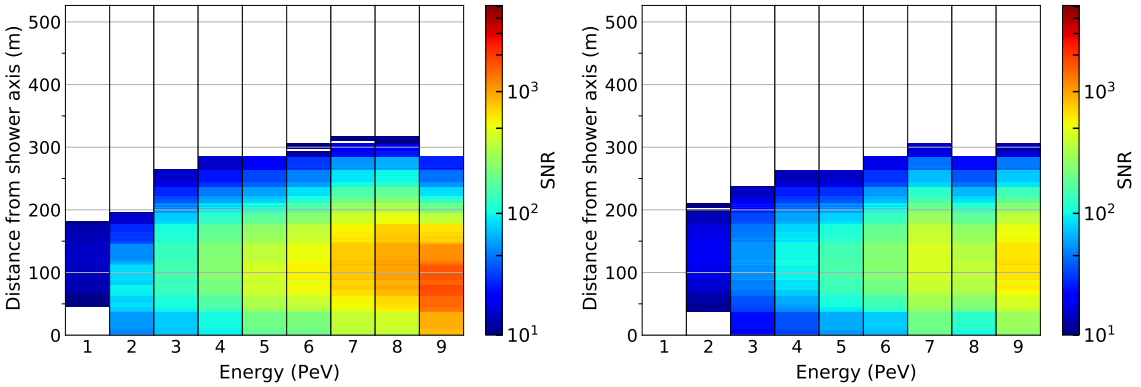

(a) γ-ray, $\theta = 61°, \phi = 0°(\alpha = 79°)$

(d) proton, $\theta = 61°, \phi = 0°(\alpha = 79°)$

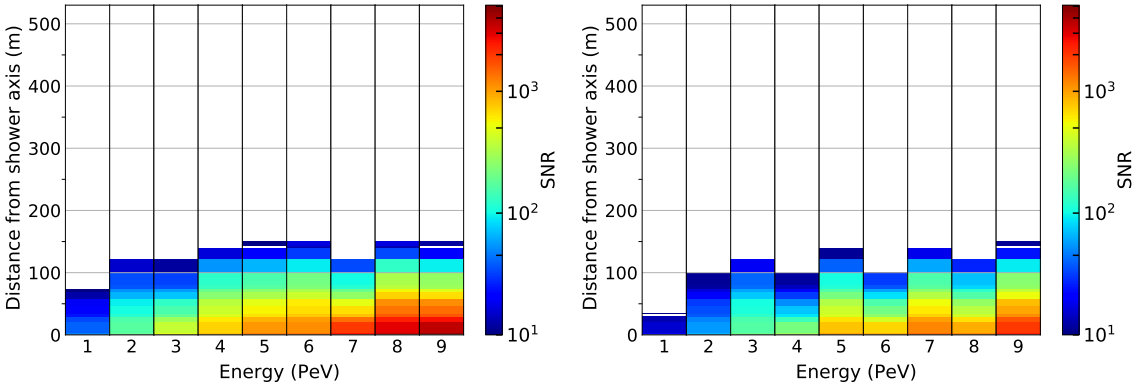

(b) γ-ray, $\theta = 40°, \phi = 0°(\alpha = 58°)$

(e) proton, $\theta = 40°, \phi = 0°(\alpha = 58°)$

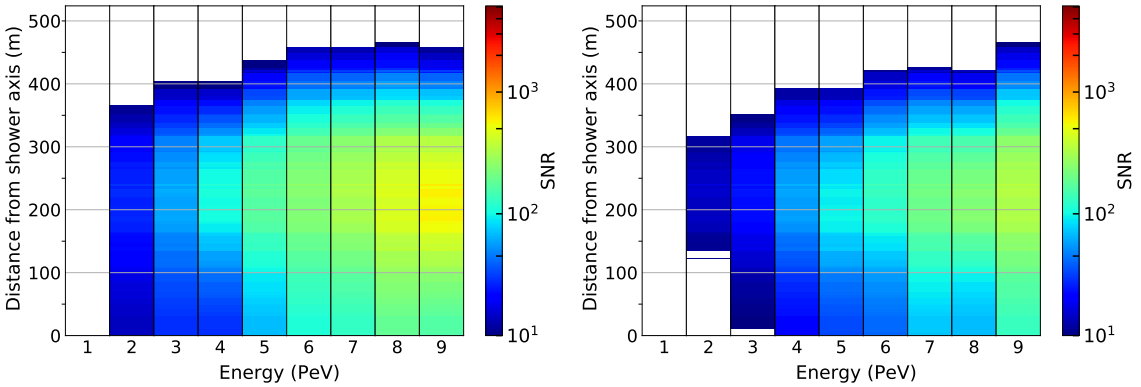

(c) γ-ray, $\theta = 70°, \phi = 0°(\alpha = 88°)$

(f) proton, $\theta = 70°, \phi = 0°(\alpha = 88°)$

Figure 6.13: Gamma-ray induced showers (left panels) and proton induced showers (right panels) at 100-190 MHz. Sample showers at the given energies are shown. Due to shower-to-shower fluctuations, the antennas that have SNR > 10 for the same zenith angle have varying distances. This is more pronounced here for proton showers.

Figure 6.13 clearly shows that the use of the optimal frequency band of 100-190 MHz enables us to lower the threshold of detection down to 1 PeV for gamma-ray showers with a zenith angle of $61°$. For proton showers of $61°$ inclination, it is possible to lower the energy threshold to the level of 2 PeV in the band 100-190 MHz. This is obviously due to the lower electromagnetic content of proton showers than that of gamma-ray showers, which is directly reflected in the radio signal. We require the criterion for detection as a minimum of three antennas in the array with a value of their SNR above 10. With three such antennas, it will be possible to reconstruct the direction of the incoming air shower. For $61°$ air showers, we can achieve this, provided we have at least three antennas within a distance of $\sim 50 - 180$ m from the shower axis. For showers at the threshold energy, this is the area where the Cherenkov ring falls on the antenna array and gives a higher level of SNR.

Figure 6.14 shows the map of the SNR on the entire array for a gamma-ray shower of 1 PeV energy, θ = 61 ° and $\phi = 0°$. The colour scale is the same as Figure 6.8 for direct comparison with a 10 PeV shower of the same orientation. The figure clearly shows that for the 1 PeV shower, it is the Cherenkov ring alone that gives the signals. This means that we need at least 3 antennas on the Cherenkov ring for detection at the threshold energy.

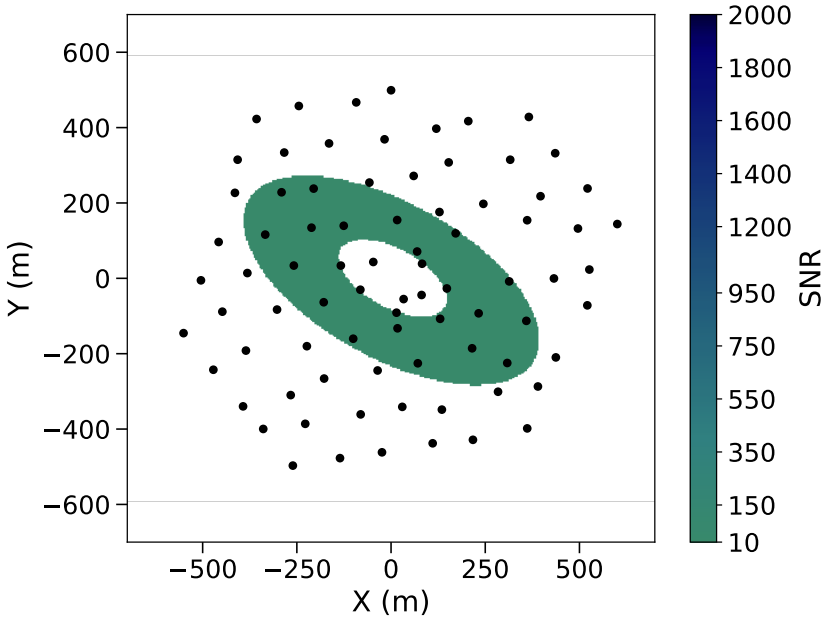

Figure 6.14: SNR map of a 1 PeV gamma-ray shower ($\theta = 61°$, $\phi = 0°$) at 100-190 MHz. The black dots represent the 81 antenna positions. Only the Cherenkov ring is visible at the threshold energy. It is sufficient to have three antennas that falls on the Cherenkov ring, in order to detect the shower. For comparison, the colour scale is set as the same as that in Figure 6.8.

The energy threshold can also be lowered for air showers with zenith angles $40°$ and $70°$ by using the optimal band as shown in Figure 6.13. For gamma-ray showers with $\theta = 40°$, we need at least three antennas within a distance of ~ 80 m from the shower axis. This means that a much denser array is needed in this case. For

proton showers this minimum distance is even lower. In the case of the 70° showers, the minimum energy that can be detected is 2 PeV for both gamma-ray and proton showers. By observing the 2 PeV energy bin of the gamma shower, one can interpret that maybe it is possible to go down to nearly 1.5 PeV for showers with 70°. This is because for the 2 PeV shower we do see antennas with sufficient SNR at stations inside the Cherenkov ring also, implying that the energy can be lowered a bit more. Such a shower was not simulated within the scope of this thesis.

Only sample showers in each energy bin are shown in Figure 6.13. It is important to study the shower-to-shower fluctuations which are inevitable due to the probabilistic nature of the interactions occurring in the air shower. This results in fluctuations in the received amplitude at the antennas of the array. To study these fluctuations, gamma-ray induced air showers with zenith angles of 61° and azimuth angles of 0° were simulated. Due to the large amount of time required for simulating each shower only 11 showers are simulated in each energy bin. Figure 6.15 shows the fluctuations in the maximum SNR and the maximum amplitude for these gamma-ray showers with energies ranging from 1-9 PeV. This is shown in the figure for a frequency range of 100-190 MHz.

It is convenient to look at the the relative standard deviation ($\frac{\sigma_{\text{observable}}}{\text{mean observable}}$) of the SNR and the amplitude for an energy independent estimate of the fluctuations. This relative deviation is calculated in each energy bin and then averaged over. The average value of the relative standard deviation of the maximum SNR of these showers with different energies is seen to be 7.6%. Similarly, a 3.7% variation in the maximum amplitude is obtained. Here, the maxima of the amplitudes are taken as the maxima of the Hilbert envelopes [124] of the signals.

A correlation between the maximum SNR (or maximum amplitude) obtained and the energy of the primary particle is visible in Figure 6.15. The maximum SNR was seen to be proportional to E^2 and the maximum amplitude $\propto E$. The fit to the maximum SNR and maximum amplitude were obtianed as follows.

$$\mathrm{SNR_{max}} = 17.04 \pm 0.43 \times E^{2.03 \pm 0.02} \tag{6.2}$$

$$\mathrm{Amp_{max}} = 8.04 \pm 0.10 \times E^{1.01 \pm 0.01} \tag{6.3}$$

Such a direct relation helps us in estimating the energy threshold for any experiment or for any primary, once we know the constants of the fit. The threshold energy can then be estimated by the relation $\mathrm{E_{threshold}} \propto \sqrt{\mathrm{SNR_{threshold}}}$. Here, $\mathrm{SNR_{threshold}}$ is 10.

6.5 Efficiency of detection

We have seen in the previous section that the energy threshold of gamma-ray detection with air showers from the direction of the Galactic Centre can be lowered to 1 PeV. This result is shown without taking the shower-to-shower fluctuations into account, which may cause variation in the received signal and thereby determine if a shower is detected or not. Therefore, it is necessary to study the efficiency of the detection of such showers produced by PeV gamma rays. Since there are slight variations (17.4%) in the SNR with the azimuth angle, this will also affect the detection rate.

For estimating the efficiency of detection, 170 simulations of gamma-ray induced showers with an energy of 1 PeV and zenith angle of 61° were performed. Random

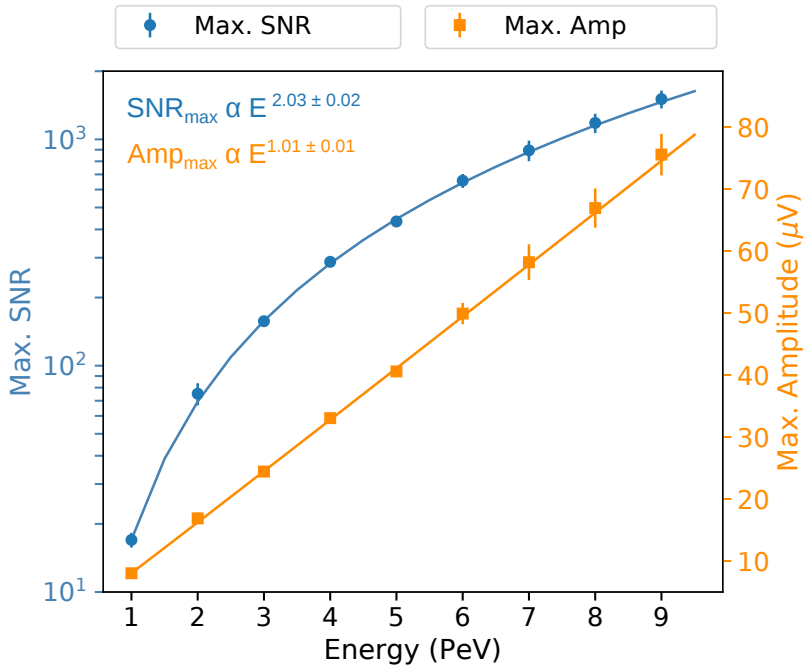

Figure 6.15: The change in the maximum SNR and maximum amplitude with energy for gamma-ray showers with $\theta = 61°$, $\phi = 0°$ and $\alpha = 79°$, in the frequency band 100-190 MHz. The mean values along with the standard deviations arising due to shower-to-shower fluctuations are shown. The best fit to both sets of simulated data points are shown. We see an E^2 nature for the maximum SNR and E^1 nature for the maximum amplitude.

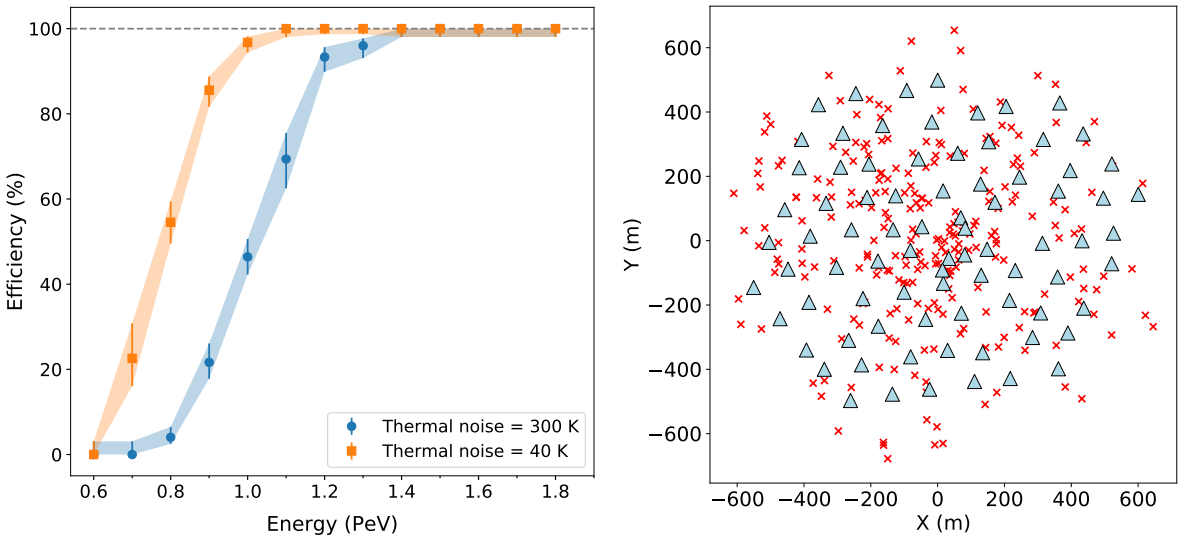

Figure 6.16: The left panel shows the efficiency of detection at different energies. An SNR > 10 in at least 3 antennas is applied as the condition for detection. This is tested for 100 γ-ray showers with $\theta = 61°$ in each energy bin in the frequency band 100-190 MHz. The core positions of the showers simulated for the energy bin of 1 PeV for the efficiency study are shown in the right panel. Showers where the radius of the core falls within 400 m from the shower centre are chosen for the investigation of the efficiency.

azimuth angles and random core positions were chosen for these simulations. The simulated core positions of these showers are shown in the right panel of Figure 6.16. A cut was applied on the simulated sample where it was required that the core positions lie within a radius of ≈ 564 m from the centre of the array. This radius corresponds to an area of 1 km^2. This cut reduced the sample size to 140 events. If more than three antennas in the array have SNR > 10, the shower is considered to be detected. We saw that the efficiency of detection of these 1 PeV gamma-ray shower was 47% for a thermal noise level of 300 K.

This implies that the efficiency reaches 100% at energies higher than 1 PeV. Therefore further simulations of gamma-ray showers ($\theta = 61^\circ$) were done with a binning of 0.1 PeV. These simulations ranged from 0.6 PeV to 1.8 PeV and consisted of 100 simulations in each bin, with random azimuth angles and random cores of radius less that 564 m. These simulations were also used to determine the energy where the efficiency of detection went down to 0%. It was observed that an efficiency of 100% is reached for an energy of 1.4 PeV and that the efficiency goes down to 0% below 0.7 PeV. This is for the case when the thermal noise is 300 K. The same procedure was repeated for a thermal noise of 40 K. This can lower the energy where 100% efficiency is achieved down to 1.1 PeV. The efficiency goes down to zero at 0.6 PeV in this case. The efficiency curve for the simulated showers is shown in the left panel of Figure 6.16. The blue dots show the higher thermal noise case and the orange squares show the low thermal noise scenario.

6.6 Uncertainties of the study

Since the method of frequency-band optimisation described over here relies on the average noise predicted by the Cane model, the local fluctuations of the absolute measurable noise with sidereal time will affect the results. There could also be variations arising from the predicted noise level. The noise model by Cane predicts a level of noise that is slightly lower than the other available sky maps. When compared to noise models like LFmap or GSM, the amplitude of the noise at 110 MHz is seen to be 15-16 % lesser for the noise predicted by the Cane model. The fluctuations due to this second order effect is neglected here.

In this study, we have considered a constant floor of thermal noise, as already mentioned in chapter 5. This may not be the case in actual measurements. It is possible that there are frequency dependent fluctuations of the thermal noise experienced by the antenna. This may cause additional affects in the prediction of the SNR. In the case of a detailed study of SNR for a specific antenna, the frequency dependent thermal noise affects should also be taken in to account. Nevertheless, for state-of-the-art antennas like the SKA-low prototype antenna SKALA, this fluctuation is very low and will not change the results shown here [108]. This antenna has a system noise of about 40 K only [108]. The temperature at the South Pole (which varies between -60^o C and -40^o C) may contribute in the reduction of this antenna thermal noise. This has to be verified with test measurements at the Pole.

It is possible to estimate the uncertainty arising due to CoREAS simulations using the experimental tests made on CoREAS so far. The air shower experiments LOPES and Tunka-Rex determined CoREAS to be accurate on an absolute scale to better than 20% at frequencies up to 80 MHz [67][68]. This means that the uncertainty in the threshold due to the use of CoREAS is likely smaller than 20%.

6.7 Conclusion and remarks

The detection of air showers using the radio technique in the PeV energy range has not been achieved until now. From this study, we see that such a detection is possible if the measurement is taken in the optimum frequency range, i.e. 100-190 MHz, especially with a low noise environment like the South Pole. With this band, it is possible to lower the threshold down to ≈ 1 PeV for gamma-ray showers with a zenith angle of 61°. This is for an antenna array with an average spacing of 125 m at the South Pole. In addition, by using interferometric methods, the very conservative condition of SNR > 10 in 3 antennas can certainly be achieved.

The optimal band at other locations also turns out to be in the same frequency range (see Appendix C). At other experimental sites, the threshold may vary depending on the ambient conditions, namely the atmosphere, the observation level and the magnetic field of the region. The noise conditions of these areas will also affect the measurement.

This method can be used not only for the specific purpose of PeVatron detection, but also for improving air-shower measurements at the South Pole. It can help in the study of mass composition at energies starting from the PeV range, which is the knee region of the cosmic ray spectrum. Furthermore, it helps in improving the veto efficiency of air-showers with IceCube, especially for inclined showers (see section 4.5 of chapter 4).

CHAPTER 7

Expected Number of Events from the Galactic Centre

Having explored the energy threshold for gamma-ray detection with the radio technique in the previous chapter, it is now possible to address the question of the expected flux of gamma rays at PeV energies from the Galactic Centre. This chapter deals with the potential PeV gamma-ray flux from the Galactic Centre, based on the flux observed by H.E.S.S., along with its comparisons with the cosmic-ray flux measured by IceTop. Finally, with such a comparison, the sensitivity of gamma-ray detection from the Galactic Centre is estimated.

7.1 Estimation of the number of gamma-ray events with PeV energies

The gamma rays detected from the candidate PeVatron at the centre of our Galaxy by H.E.S.S. ranges from hundreds of GeV to nearly a 100 TeV. This follows a spectral shape of $E^{-2.32}$ with no preference for a cut-off in the spectrum at these energies. Nevertheless, the existence a cut-off at higher energies can be expected since the source will have a maximum energy up to which it can accelerate particles. The best-case scenario would be the spectrum with no cut-off. In order to estimate the flux at higher energies, an extrapolation of the spectrum observed by H.E.S.S. can be done. Apart from this extrapolation, one should also take into account the absorption of gamma rays in the inter-galactic medium.

7.1.1 Survival Probability of gamma rays

It was seen in Figure 2.2 in chapter 2 that the gamma rays at high energies are highly attenuated as they traverse the universe. The maximum distance up to which PeV gamma rays travel is approximately the distance from the centre of the Milky Way to the sun. Figure 2.3 depicts the total contribution to absorption of gamma rays from the background sources of photon fields. In this study, only the contribution from the CMB is considered, as this is the dominant source of absorption at PeV energies.

Figure 7.1 shows the attenuation length of gamma rays of different energies in the CMB [128] and the corresponding survival probability of the gamma rays in

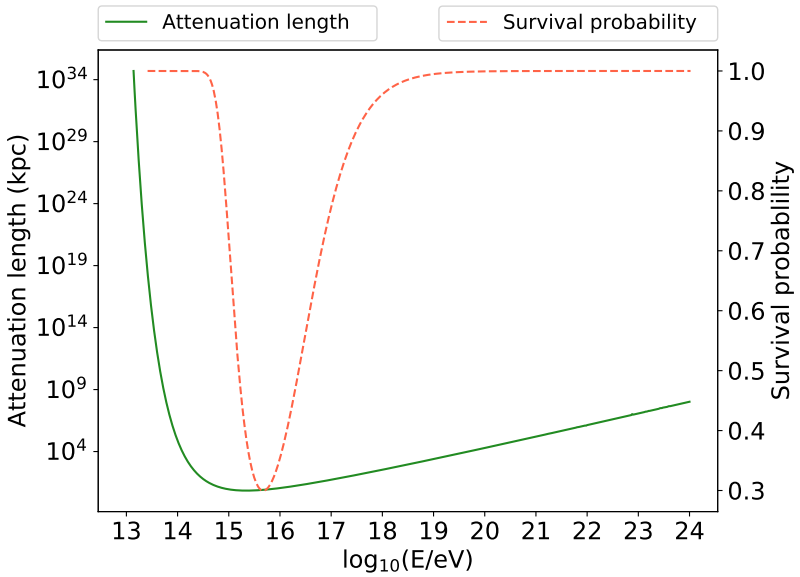

Figure 7.1: Attenuation length and survival probability of gamma rays with different energies on arrival from the Galactic Centre to the Earth. Here, distance to the Galactic Centre is taken as 8.5 kpc.

this photon field, as they approach the Earth from the Galactic Centre. Here, the distance from the Galactic Centre to the Earth is taken to be 8.5 kpc. The survival probability, the probability with which the gamma rays arrive at the Earth after passing through the absorbing media of relic photons, is defined over here as

$$P = \frac{1}{e^{L_{\rm dis}/L_{\rm atten}}} \tag{7.1}$$

where $L_{\rm dis}$ is the distance travelled by the gamma rays (here 8.5 kpc) and $L_{\rm atten}$ is the attenuation lengths of the gamma rays at different energies, as shown by the green solid curve in Figure 7.1. The resulting survival probability of gamma rays is given by the red dashed curve.

7.1.2 Number of events

The spectral form that is used here for the extrapolation of the flux is given by $\frac{dN}{dE} = 1.902 \times E^{-2.32}$. This is the best-case scenario, that is a spectrum without a cut-off. A spectrum with cut-off at energies like 1 PeV, 10 PeV or 100 PeV is also possible. Nevertheless, since we do not know the exact cut-off energy, only the no-cut-off spectrum is discussed here. The other cases with cut-off will be discussed in the following sections.

The extrapolated spectrum can then be multiplied by the survival probability in order to account for the absorption of the traversing gamma rays in the CMB medium. The extrapolated spectrum before and after attenuation are shown in Figure 7.2, along with the data from H.E.S.S.[5].

Finally, the efficiency of detection of the radio array at various energies should also be considered. Therefore, the attenuated flux is multiplied with the efficiency of the antenna array at different energies, derived in Figure 6.16 of the previous chapter. The resulting flux that will be seen by the antenna array is shown by the

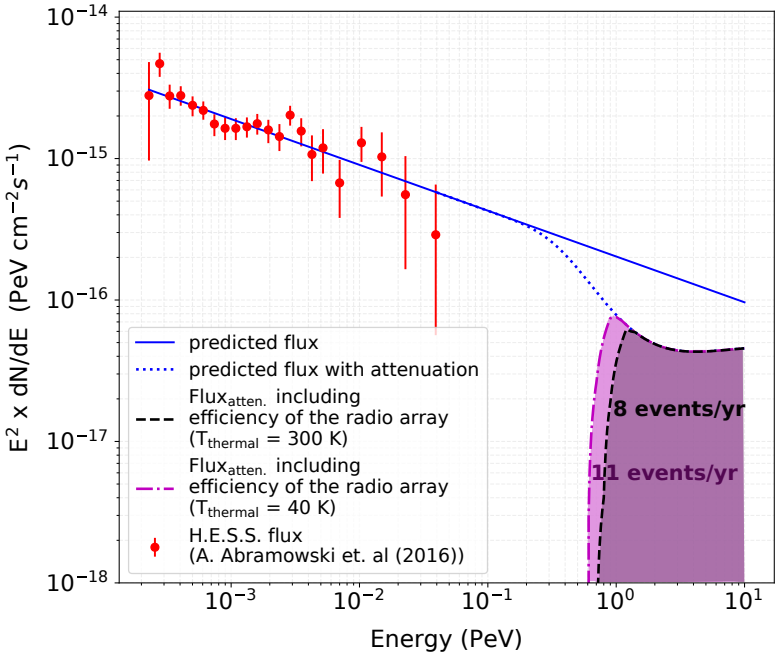

Figure 7.2: Flux as seen by H.E.S.S. [5], with a simple $E^{-2.32}$ extrapolation. The gamma-ray flux will get attenuated due to interactions with the CMB. The detectable flux takes the detection efficiency of the radio array into account. This plot is adapted from [120].

black dashed curve in Figure 7.2. This is the observable flux by the antenna array if the thermal noise is 300 K. For the lower thermal noise case (40 K), where a better efficiency is expected, the flux can be detected starting from slightly lower energies. This is represented by the pink dotted-dashed curve in Figure 7.2.

The number of events that can be expected to be measured from such a spectral shape using an antenna array as used in this study can be obtained by an integration of the pink and black curves in Figure 7.2. The pink curve shows the number of events for the lower thermal noise case (8 events/year) and the black region shows that for the higher thermal noise (11 events/year). This expected event rate is estimated for the period of a year for an array of area 1 km^2. Since the Galactic Centre lies at an inclination of 61° at the South Pole, the area of coverage of the array has to be weighted by a geometric factor of cosine(61°). That is the effective area becomes $A_{\text{eff}} = A\cos(61°)$.

Table 7.1 shows the number of events obtained in this manner above different energies. This is by assuming that the events that are detectable by the radio array will also be triggered. The table shows the number of events directly obtainable from the flux, and the number of these events that can be observed by the radio array—by including the efficiency of detection of the array. The table shows this for energies where there is a non-zero efficiency (0.6 PeV for thermal noise of 40 K and 0.8 PeV for a thermal noise of 300 K). Also shown are the number of events above full efficiency (1.1 PeV for 40 K case and 1.4 PeV for 300 K case).

	$N_{\text{events}}(> E_0)$ (1 yr)	$N_{\text{events}}(> E_0)$ $\times$ efficiency$_{300\,\text{K}}$	$N_{\text{events}}(> E_0)$ $\times$ efficiency$_{40\,\text{K}}$
E_0 = 0.6 PeV (efficiency$_{40\,\text{K}} > 0$)	19	7.9	11.5
E_0 = 0.8 PeV (efficiency$_{300\,\text{K}} > 0$)	11.5	7.9	10.9
E_0 = 1.1 PeV (efficiency$_{40\,\text{K}} = 1$)	7	6.9	7
E_0 = 1.4 PeV (efficiency$_{300\,\text{K}} = 1$)	5.1	5.1	5.1

Table 7.1: Estimated number of events per year obtained from the extrapolation of the attenuated gamma-ray flux, with and without detector efficiency limits.

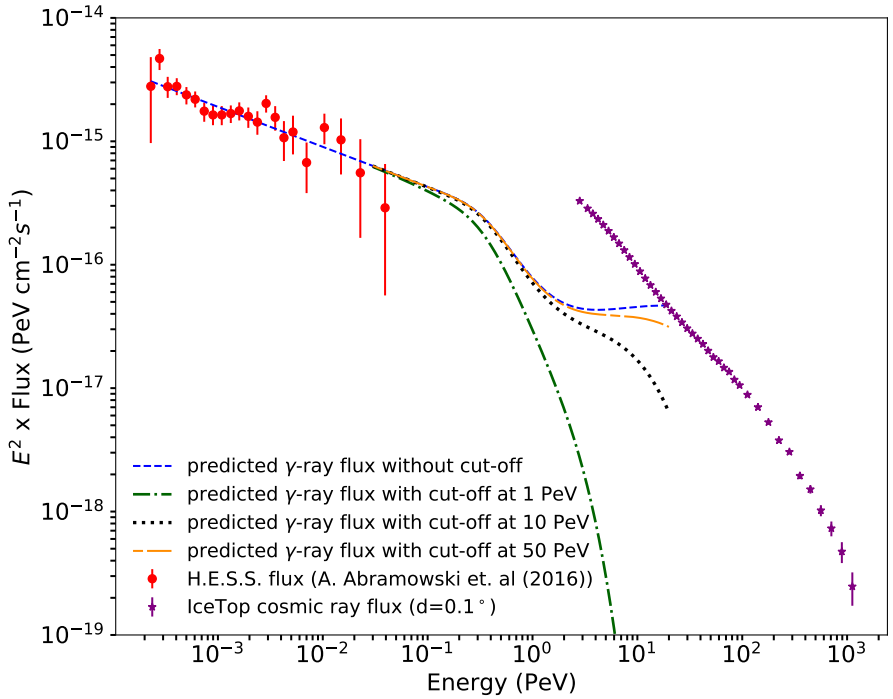

Figure 7.3: The gamma-ray flux with different possible scenarios for the cut-off energy, E_c (1 PeV, 10 PeV, 50 PeV or no cut-off). The flux is described by $\frac{dN}{dE} \propto E^{-2.32} \times e^{-(\frac{E}{E_c})}$. Also shown is the flux of cosmic rays measured by IceTop [129] within a sky of diameter $0.1°$.

7.2 Sensitivity of the radio array

A major source of background for these gamma rays are charged cosmic rays, which also produce air showers similar to those produced by gamma rays. The cosmic-ray flux is much higher in magnitude than the gamma-ray flux, which further adds to the challenge. Figure 7.3 shows the cosmic-ray flux measured by IceTop [129] along with the predictions of the gamma-ray flux (by extrapolating the diffuse flux from the Galactic Centre from H.E.S.S. [5]). These predictions show some of the possible scenarios of the flux: e.g. cut-off at 1 PeV, 10 PeV and 50 PeV along with the no cut-off scenario. The IceTop cosmic-ray flux shown in Figure 7.3 corresponds to that

within a region of sky with a diameter of 0.1°, since this is the best angular resolution achieved so far for a radio air-shower array [130]. This is of course valid only if the source of gamma rays is a point source. For an extended source, a sky with a larger diameter has to be considered, thereby increasing the number of incoming cosmic rays from the same sky as that of the gamma rays. The relative fluxes of the cosmic rays and gamma rays indicates the required rate of rejection of cosmic rays for the identification of the gamma-ray showers. The next section describes the required gamma-hadron separation in detail.

7.2.1 Gamma-hadron separation

In order to detect any of these possible scenarios of the gamma flux, we have to distinguish them from the cosmic-ray showers. That is, the hadronic showers should be rejected to select out the gamma-ray showers. The power of rejection of hadronic showers will determine the significance of the measured gamma-ray showers. That is, the higher the gamma-hadron separation factor, the better is the statistical significance. In the following, gamma-hadron separation factor (Q) is defined as the amount by which the detected number of cosmic rays could be suppressed by a dedicated analysis. We can estimate the required amount of suppression to obtain a significance of 5σ (for a discovery potential) in the observed number of gamma rays. In particular, the integral number of gamma rays and cosmic rays is considered for this.

The uncertainty in the measured number of gamma rays (N_γ)is given by $\sigma = \sqrt{N_{CR}}$, where N_{CR} is the number of cosmic rays above a certain energy. After applying a gamma-hadron separation factor of Q, the uncertainty becomes $\sigma = \sqrt{\frac{N_{CR}}{Q}}$. In order to have a 5σ significance, it is required that

$$N_\gamma > 5\sqrt{\frac{N_{CR}}{Q}}. \tag{7.2}$$

Since both the number of gamma rays and the number of cosmic rays are changing with energy, the required value of Q to satisfy equation 7.2 also changes with energy. Moreover, the required Q factor depends on the flux of gamma rays, and also the amount of thermal noise in the antenna, i.e., it depends on the incoming flux as well as the detector setup.

Figure 7.4 shows the required separation factor for an integral flux above each energy for obtaining a 5σ significance. This is shown for the different possible scenarios of the flux. The left panel shows the Q factor for 40 K thermal noise and the right panel for 300 K thermal noise. Clearly, we need only lower levels of gamma-hadron separation for lower thermal noise, especially at energies lower than 1.3 PeV which is near to the full efficiency of the 300 K thermal noise case. The required Q factor also changes drastically depending on the flux of gamma rays. In the case of the flux with a cut-off at 1 PeV, a separation factor as large as 1000 is needed. However, if the cut-off energy is higher than 1 PeV, such high levels of gamma-hadron separation is not required. Even for a cut-off at 5 PeV, a gamma-hadron separation factor of ≈ 20 is enough. For optimistic scenarios like a cut-off energy of 50 PeV and a spectrum without a cut-off, it is only required to have a separation factor of 10. This is also the case for a median flux with a cut-off energy at 10 PeV. It has to be kept in mind that these required separation factors

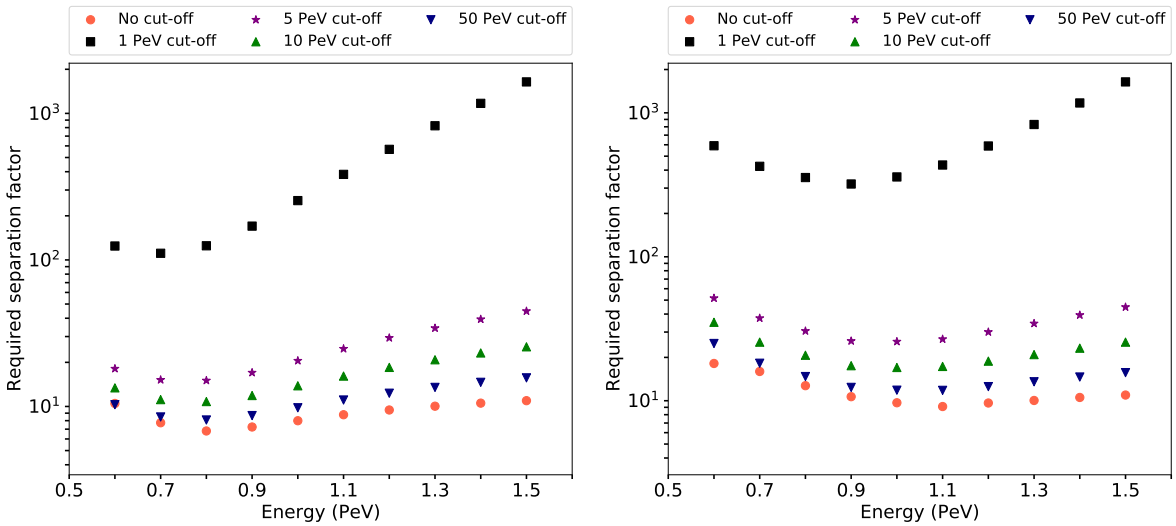

(a) Thermal noise = 40 K (b) Thermal noise = 300 K

Figure 7.4: The required separation factor for 5σ detection with detection efficiency for two cases of thermal noise. The required Q factor changes with energy, and is lower for lower thermal noise (for energies below 1 PeV).

are obtained for a point-source scenario. For an extended source, higher levels of gamma-hadron separation may be needed.

For the low thermal noise case, it seems that the minimum required Q factor is for the integral flux above ≈ 0.8 PeV, for all kinds of fluxes. When the thermal noise is 300 K, this energy goes up to ≈ 1 PeV. By comparing with Fig. 6.16, it can be seen that this is the energy where the efficiency becomes close to 40 %. That is, at this energy the efficiency is high enough that a reasonable number of showers are detected, and at the same time a larger number of gamma-ray events can be observed than the number observable at higher energies.

The rejection of hadronic showers for obtaining the desired level of gamma-hadron separation can be done by using the information of the shower maximum or by using the different muon content of showers from showers of different primaries. One may have to device specific techniques to achieve this. The optimisation of this requires a separate, deeper study which is beyond the scope of this thesis.

7.2.2 Sensitivity for different flux shapes

The sensitivity of the experiment is dependent on both the detection capability of the experiment, as well as the shape of the incoming flux. The experimental contributions are the collection area (which is 1 km^2 over here), the efficiency of detection (described in 6.5), the hadron rejection capability (Q factor), and the time for which the measurement is taken (the longer the measurement, the better the sensitivity).

Apart from these, the spectral index of the incoming flux hugely determines the number of incoming gamma rays and therefore has an effect on how fast a 5σ detection can be achieved. A harder spectrum provides better sensitivity. The sensitivity also changes with the cut-off energy of the spectrum, as long as the cut-off energy is within the detection energy range of the experiment. A cut-off

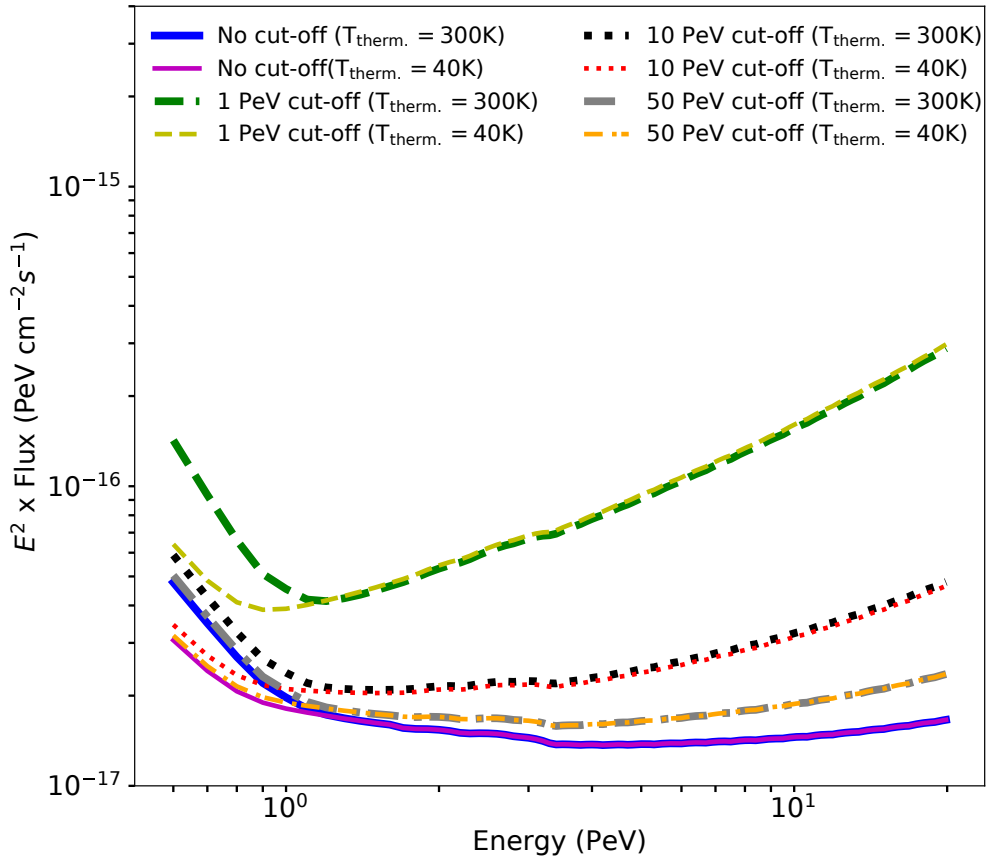

Figure 7.5: The integral sensitivity of the radio array to gamma-ray flux from the Galactic Centre assuming different cut-off energies. These have a spectral index of -2.32, consistent with the observed H.E.S.S. flux. Cosmic-ray flux within a diameter of 0.1° is assumed to be suppressed with a gamma-hadron separation factor of 100. The shown integral sensitivity is for a period of 5 years. Also shown are the cases when the radio array has a lower level of thermal noise, and therefore higher efficiency at lower energies.

at lower energies will result in lesser number of incoming gamma rays, making it harder to achieve 5σ.

For the estimation of the sensitivity, a constant level of separation factor can be assumed. With this, the sensitivity that could be achieved for each injected flux with different cut-off energies is estimated. Here, the following spectral shape of the injected flux is taken.

$$\frac{dN}{dE} = K\Phi = K\Phi_0 \times e^{-(\frac{E}{E_c})} \tag{7.3}$$

where Φ_0 is the spectral shape of the flux observed by H.E.S.S. up to nearly a 100 TeV, E_c is the cut off energy, and K is the corresponding fraction of Φ that gives a 5σ detection. That is, for a given flux of cosmic rays, a given flux of gamma rays (Φ), and for a given Q factor, it is possible to determine the value of K, which gives the required number of gamma rays to satisfy the condition $\mathrm{N}_\gamma/\sqrt{\mathrm{N}_{\mathrm{bkg}}} = 5$. Here, $\mathrm{N}_{\mathrm{bkg}} = \mathrm{N}_{\mathrm{CR}}/\mathrm{Q}$. K then represents the sensitivity as a fraction or percentage of the injected flux. This fractional sensitivity can also be multiplied with the injected flux

(i.e. $K\Phi$). Here, this final multiplied factor is represented as the integral sensitivity above each energy bin.

The integral sensitivity obtained for a period of 5 years with a Q factor of 100 is shown in Figure 7.5 for thermal noise levels of 300 K and 40 K. The injected fluxes are: flux with no cut-off, flux with cut-off at 1 PeV, at 10 PeV and at 50 PeV. The integral sensitivity is calculated for every energy bin with an interval of 0.1 PeV. All excesses above the sensitivity curve can be observed by the radio array, with the respective conditions of efficiency and Q factor.

As expected, the sensitivity is the best for a flux with no cut-off in the spectrum. Also, the higher the cut-off energy, the better is the sensitivity curve and consequently the chances of observing this flux becomes higher. At lower energies, there is a significant improvement in the sensitivity for the low thermal noise case as compared to the one with 300 K—due to the better efficiency at these energies. For example, in the 1 PeV cut-off scenario, the green dashed curve represents the sensitivity if the thermal noise is 300 K. The yellow dashed curve represents that for 40 K. The yellow curve is much lower than the green curve for energies lower than ≈ 1.1 PeV. Beyond this energy, both levels of thermal noise provide the same sensitivities. For all flux scenarios, at an energy of ≈ 1.1 PeV the sensitivity is the same for both cases of thermal noise.

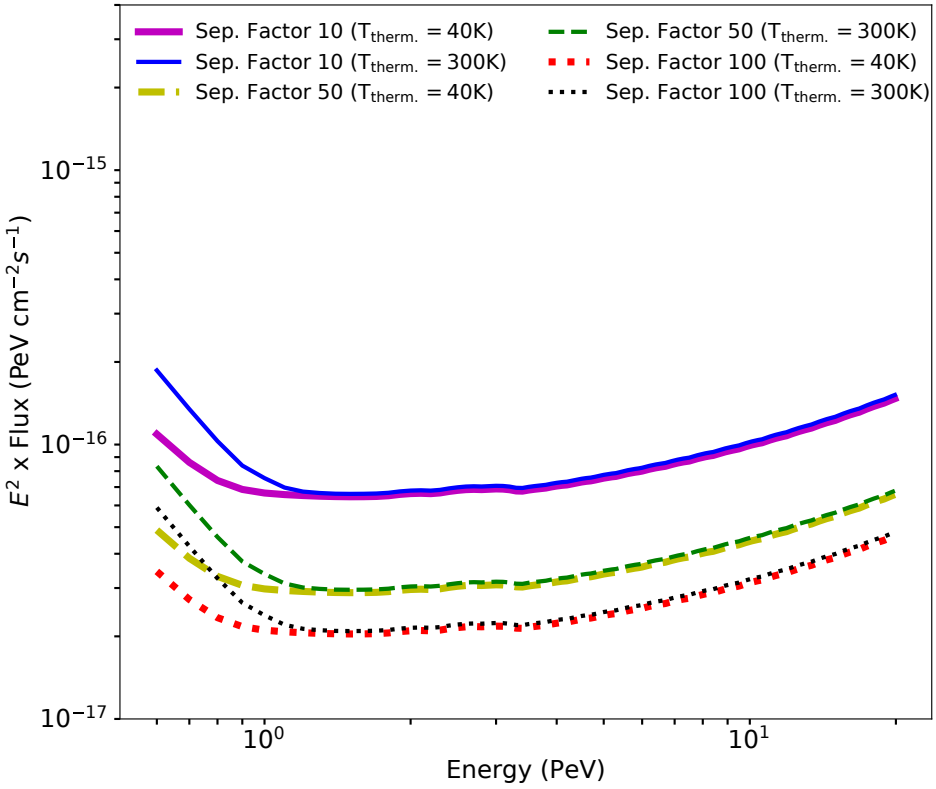

Figure 7.6: Integral sensitivity to a nominal flux with cut-off at 10 PeV for 5 years of observation. The sensitivity dependence on the gamma-hadron separation factor is shown. For both low thermal noise and high thermal noise case, , the higher separation factor shows the better sensitivity.

Depending on the level of the constant Q factor that can be achieved, the sensitivity curve for each case becomes worse or better, for the different cases of injected

flux. We can consider the case for the median flux of 10 PeV cut-off and see how the curve changes for different levels of separation factor. Figure 7.6 depicts this case. The figure shows the sensitivities for separation factors of 10, 50 and 100. These sensitivities are shown again for both thermal noise cases. It is obvious that the energy where the two thermal noise cases converge in their sensitivity does not change with the separation factor. Therefore, this is clearly a manifestation of their respective efficiencies.

It can be seen that if higher levels of separation factor are achieved, the sensitivity becomes much better for both flux scenarios. That is, by improving the background rejection more distinct gamma-ray events can be observed. Another way to improve this would be to collect more data, for longer periods of time and to increase the effective area of the array. Thus, it is clearly important to have better levels of Q factor for a fixed array design, in order to improve the sensitivity.

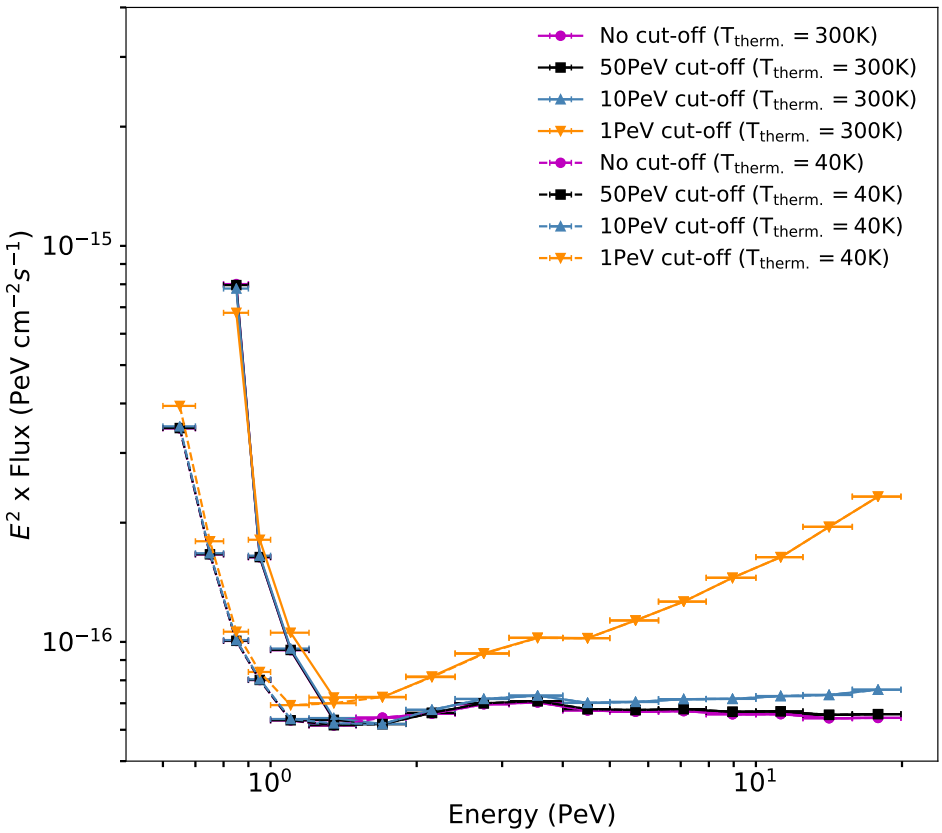

Figure 7.7: The differential sensitivity of the radio array to gamma-ray flux from the Galactic Centre with various cut-off energies. The sensitivity is shown for 5 yrs of observation and for a gamma-hadron separation factor of 100. The differential sensitivity is obtained from the integral sensitivity within the energy bin shown as error bars along the x axis. The solid curves depict the 300 K thermal noise scenario and the dashed curves depict the 40 K scenario.

On integrating the spectrum, the total number of detected photons are enhanced, and the significance is thereby improved. But this results in the shape of the spectrum being washed out. The differential sensitivity preserves the shape of the spectrum, and fluxes with different cut-off energies, vary in the corresponding

sensitivity only at energies where the spectral shape starts to deviate from each other.

Figure 7.7 shows the differential sensitivities obtained for fluxes with cut-off energies $E_c = 1$ PeV, 10 PeV, 50 PeV and at infinity (no cut-off). The dashed curve shows the 40 K case and the sold curve shows the 300 K case. This is produced by finding the total number of events in given an energy bin. The width of the energy bins are shown as error bars on the x axis. The figure shows the sensitivity for Q = 100.

It is clear that at lower energies, where the spectral shape of the injected fluxes are similar, similar sensitivities are seen for these fluxes. That is, it is now largely dependent only on the instrument and the spectral index. But as soon as the energy increases, the spectral shape changes (due to the cut-off) and the differential sensitivities deviate from each other correspondingly (compare with Figure 7.3).

7.3 Conclusion and remarks

The possibility to detect gamma rays above the higher fraction of cosmic rays using a radio array was discussed here. It is clear that with such an array, it is possible to prove if the Galactic Centre accelerates gamma rays up to PeV energies or not. A cut-off scenario at 1 PeV may result in a non-detection of gamma rays from the Galactic Centre. On the other hand, if the cut-off is at higher energies, the radio array can measure this flux and determine the exact cut-off energy. The sensitivity of this radio array is optimistic in the case of a flux with a cut-off energy that is even as low as 10 PeV. On the deployment of the entire array and successful measurement of PeV showers for sufficiently long time, it can be attempted to search for these PeV gamma rays from the Galactic Centre. For a case of non-observation, it will be possible to provide an upper limit to this gamma-ray flux. In the instance of a successful observation it will be possible to provide a flux behaviour with energy, which will become more precise with longer durations of measurement.

CHAPTER 8

Trigger Schemes for the Radio Array

Traditionally, triggers for radio air-shower arrays are issued using particle detectors as an external trigger source. Examples are LOPES and LOFAR (with scintillators providing the external trigger), AERA (with surface Cherenkov tanks acting as the external trigger) and Tunka-Rex (with the air-Cherenkov telescopes and scintillators acting as the external trigger). This method limits the efficiency of detection of the radio array to that of the particle array. Although this might not be an issue for nearly vertical showers, inclined showers can suffer from this, as the number of particles detected on the ground are very low, especially for showers with PeV energies. This is more critical for gamma-ray showers than for hadronic showers due to their lower muon content.

Experiments focused on neutrino detection like ARIANNA [71] and ANITA [94] have demonstrated their capability to measure air showers using the scheme of self-triggering. With a self-triggering scheme, the RFI noise sources have to be identified and taken care of in order to avoid "fake signals". A prototype system that operates in self-trigger mode was under operation for 4 years at the Pierre Auger Observatory [131]. Showers within the energy range of 0.1-10 EeV were successfully measured using this system. The study showed the necessity of a dynamic threshold for each antenna, that can be tuned based on the local noise condition of each antenna at a given time. CODALEMA-3, attempts to detect cosmic-ray showers using an interferometric scheme of self-triggering. A known catalogue of the sources of RFI near to the array is used to distinguish EAS signals from the anthropogenic radio signals [79][132]. TREND, located in a radio-quiet zone in South China, has shown that self-triggering works in low-noise conditions, using a simple signal-over-noise condition for the trigger [133] [134].

In this chapter, the different viable options for triggering the radio-antenna array at the South Pole will be explored in detail. They are divided into three: (i) the trigger capability of IceTop; determined using the measured IceTop data, (ii) the trigger capability of a future scintillator array, (iii) and a brief discussion on the possibility of self-triggering.

8.1 IceTop as an external trigger

IceTop, with 162 ice-Cherenkov tanks can be thought of as a source of external trigger for the radio antennas. There are two kinds of hit data available in IceTop. A *Hard Local Coincidence (HLC)* occurs when there are two tanks in a station with recorded hits. A *Soft Local Coincidence (SLC)* is referred to the situation where there is only one tank in a station with a recorded hit. The normal data-taking stream in IceTop operates under the condition that at least 6 HLC pulses should be detected (which corresponds to 3 stations). For cosmic rays that are nearly vertical, this means that the detector will have full efficiency above a PeV. This is not the case for inclined showers, where lesser number of particles will arrive at the detector. If a particle from the inclined shower survives until the ground and arrives at the detector, the IceTop tank will be able to measure this particle, just like it measures a particle from a vertical shower. Detector area effects don't come in to play over here since the tank is almost as high as it is wide (≈ 1 m). Measurements of vertical and horizontal muons, taken at the Pole, using IceTop tanks show that they can indeed measure particles from higher inclination [135]. This section explores the detection threshold and detection efficiency for measuring inclined air-showers using IceTop experimental data and simulations.

8.1.1 Constant Intensity Method for threshold determination

The standard IceTop data analysis does not include showers with inclinations greater than $35°$. Therefore, the energy calibration for the reconstruction routine has been done only up to $36°$. Due to this, the threshold energy of IceTop for showers coming from an inclination of $61°$ is unknown. To overcome this limitation, we adopt the method of constant intensities to estimate the energy threshold for showers that are inclined up to $65°$. This section discusses the details of this approach.

The constant intensity method stems from the notion that the cosmic-ray flux is isotropic and therefore has a constant rate from all directions for a given energy [136]. Therefore, the rate of arrival seen for the vertical showers should be the same as that for the inclined showers. This is only true above the threshold energy of the detector for the detection of inclined showers. Below this threshold energy, the detected rate starts falling down.

We can use this principle to determine the threshold energy for inclined showers. That is, by comparing the integral flux for inclined showers with that for vertical showers; and determining the energy where the flux starts falling down.

The differential flux in terms of the energy proxy—the shower size S_{125}—is given as

$$F = \frac{\mathrm{d}I}{\mathrm{d}S_{125}} = \frac{\mathrm{d}N}{\mathrm{d}S_{125}} \frac{1}{T A_{\mathrm{eff}}} \tag{8.1}$$

where T is the total measurement time, A_{eff} is the effective area, which is the projection of the detector area (A_0) into the entire solid angle of detection ($\Delta\Omega$).

$$A_{\mathrm{eff}} = \int_0^{2\pi} \int_{\theta_{\mathrm{min}}}^{\theta_{\mathrm{max}}} A_0 \cos\theta \mathrm{d}\Omega = \int_0^{2\pi} \int_{\theta_{\mathrm{min}}}^{\theta_{\mathrm{max}}} A_0 \cos\theta \sin\theta \mathrm{d}\phi \mathrm{d}\theta \tag{8.2}$$

On performing the integration over θ and ϕ, we get

$$A_{\mathrm{eff}} = \pi A_0 \Delta \cos^2\theta \tag{8.3}$$

where $\Delta\cos^2\theta = \cos^2\theta_{\min} - \cos^2\theta_{\max}$ gives the zenith angular bin width.

Therefore, if we divide the measurements into zenith angular bins of equal $\Delta\cos^2\theta$, the flux values in these bins will be the same. Upon integrating the flux above each energy bin, we get

$$I(> S_{125}) = \frac{N(> S_{125})}{\pi T A_0 \Delta\cos^2\theta} = \text{constant} \tag{8.4}$$

This means that we will be able to get constant intensities with such an approach, with the observed events being divided into bins of equal width in $\cos^2\theta$. In this study, we use a constant $\Delta\cos^2\theta = 0.1786$. This gives us 6 bins between 0° and 65°. Table 8.1 shows the resulting angular bins. Of these bins, we are interested in the final bin (55.83° - 64.99°) since this bin contains the events at $\theta = 61°$.

θ values	$\cos^2\theta$
0 - 21.72	1 - 0.863
21.72 - 31.55	0.863 - 0.726
31.55 - 39.86	0.726 - 0.589
39.86 - 47.73	0.589 - 0.452
47.73 - 55.83	0.452 - 0.315
55.83 - 64.99	0.315 - 0.179

Table 8.1: The θ and $\cos^2\theta$ bins into which the events are divided.

The differential and integral flux obtained in these angular bins, with respect to $\log_{10}(S_{125})$ is shown in Figure 8.1. The figure is produced by using ≈ 56 hours of data from the year 2012. Figure 8.1b is obtained on summing up the events above each $\log_{10}(S_{125})$ bin in Figure 8.1a. The conversion of the bins in S_{125} from log scale to regular scale is taken care of while summing the number of events.

Figure 8.1b shows that the energy range in each zenith bin for a constant value on the y-axis is the same. For example, if we take $I(> S_{125}) = 10^{-8}$, the mean energy of cosmic rays within all the angular bins are the same. This implies that a value of $\log_{10} S_{125} \approx 1.5$ in the bin 47.53° - 55.83° corresponds to $\log_{10} S_{125} \approx 2.3$ in the bin 0° - 21.72°. Therefore, we can use this to calibrate the unknown energy of the showers with higher inclination.

We choose a reference zenith angle in order to make a comparison between the showers coming from different zenith angles. All showers arriving from various inclinations are compared to showers arriving from this reference angle. Figure 8.2 shows the distribution of the incoming angles for a subset of the data from 2012. We can see that the median of these zenith angles is at 26°. This median angle is chosen as the reference angle to which all other showers are compared.

Once this reference angle is chosen, it is natural to compare the S_{125} obtained in all the 6 zenith bins to the S_{125} of the reference angle, 26°. Figure 8.3 depicts such a comparison made for some example values of $I(> S_{125})$. The vertical showers are shown on the right extreme of the plot and the more inclined showers are given at the left. The grey dashed line in the figure represents the reference angle, $\theta = 26°$.

It can be seen that in general, the S_{125} changes in a parabolic form as the arrival angle changes. This S_{125} value becomes lower as the zenith angle increases. This is due to the attenuation of the signal as the shower traverses the atmosphere. That is, the stage of development of the shower while it arrives on the ground depends on

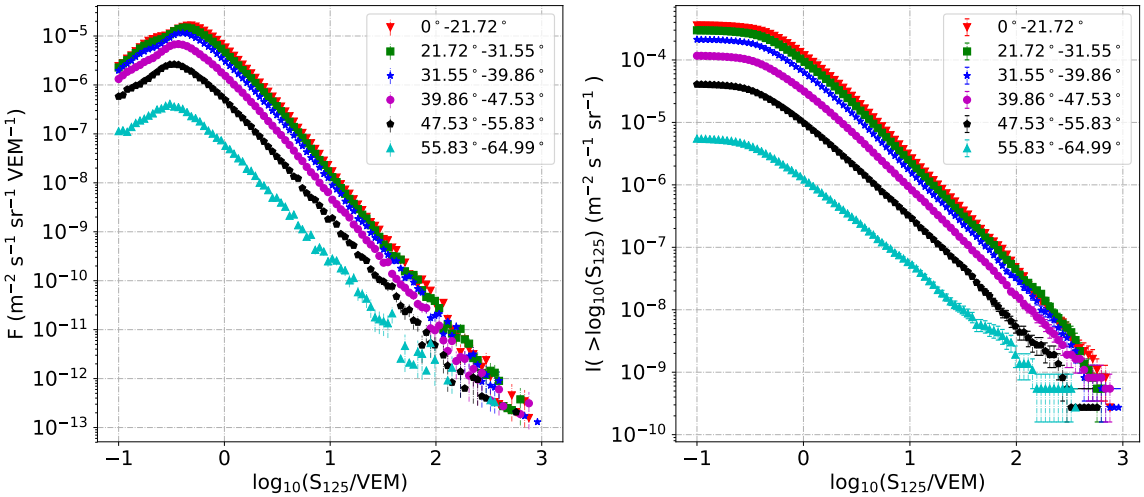

(a) Differential flux

(b) Integral flux

Figure 8.1: The differential (a) and integral (b) fluxes obtained for showers divided into zenith bins with equal values of $\Delta\cos^2\theta$. The figures represent the data measured by IceTop in the year of 2012.

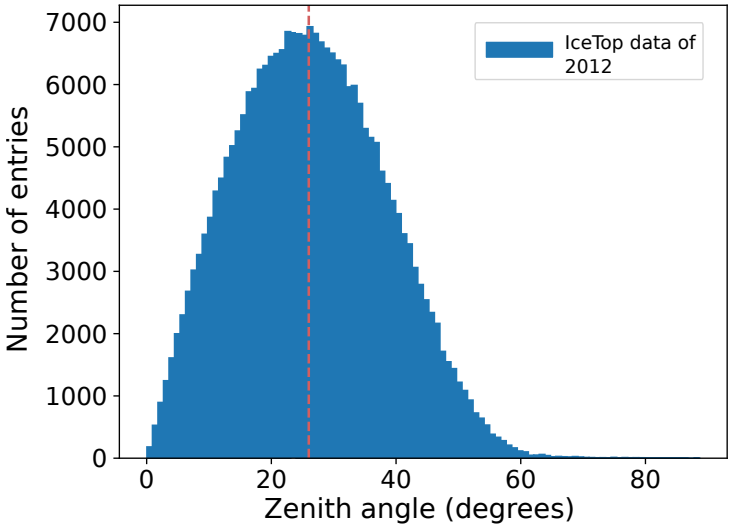

Figure 8.2: Distribution of the reconstructed angles obtained for a subset of the showers measured in the year 2012. The median angle is found to be 26°, represented by the red dashed line in the plot.

the inclination of the shower. The more inclined the shower is, the more stages it has passed through before reaching the ground, as shown in Figure 6.11. For the more inclined showers, this means that there is less energy deposited in the detector, which causes the S_{125} to be lower for these showers. Therefore, the distribution in Figure 8.3 has a parabolic shape.

It is possible to fit a parabola to this distribution of $\log_{10}S_{125}$ vs $\cos^2\theta$. A parabola of the form $ax^2 + bx + c$ is chosen over here, where $x = \cos^2\theta - \cos^2(26°)$. This is similar to the parabolic shape used by the Auger experiment [137]. On performing

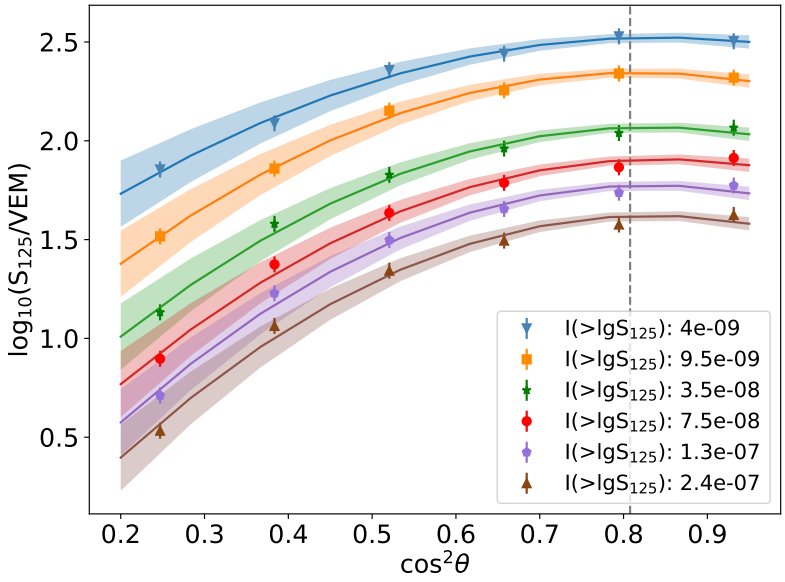

Figure 8.3: A parabolic shape of the form ax^2+bx+c is seen for the value of $\log_{10}S_{125}$ in different zenith bins for a given value of the integral flux. Some examples are shown here. The shaded area shows the error of the fit for each curve. The dashed line corresponds to the reference angle of 26°.

this fit, it is possible to find the value of $\log_{10}S_{125}$ obtained for the reference angle, for a given set of $\log_{10}S_{125}$ for the other angular bins. This value of S_{125} for the reference angle is hereby represented as $S_{125}^{26^\circ}$.

On obtaining the value of $S_{125}^{26^\circ}$ for all sets of showers in Figure 8.1b, we can re-order this integral flux in all zenith-angular bins in terms of $S_{125}^{26^\circ}$. This re-ordered integral flux is shown in Figure 8.4. The fit as explained above is performed only for showers that are well above the threshold energy. For example, showers in the last zenith bin are included in the fit only for a minimum integral flux value of $I(> S_{125}) = 3.9 \times 10^{-7}$ in Figure 8.4. For the inclined showers that fall in the integral flux bin lower than this, a constant shift in $\log_{10}S_{125}^{26^\circ}$ corresponding to the bin width of $\log_{10}S_{125}$ is applied.

On the re-ordering of the integral flux curves in this manner, it is seen that the flux values for all the zenith bins lie on top of each other, provided the measurement is above the threshold energy of the particular bin. Below this energy, the integral flux starts deviating from the general shape and starts decreasing with respect to the general trend as the energy decreases, until it becomes a constant value.

To determine the threshold value of $S_{125}^{26^\circ}$ for the last zenith bin, after which the system is fully efficient, we can compare the intensities of all the zenith bins close to this threshold $S_{125}^{26^\circ}$. Above the threshold, the intensities remain the same, as already explained, and below the threshold value, the intensity drops only for the zenith bin containing large angles.

In order to make this comparison, the values of $\log_{10}S_{125}^{26^\circ}$ are fixed and the intensities are compared with the $\cos^2\theta$ values. This comparison is made for $\log_{10}S_{125}^{26^\circ}$ from 1.38 to 1.43 for 2012 data, with an increment of 0.1 in its value. This is shown in Figure 8.5a. The x-axis shows the $\cos^2\theta$ values, of which the left extreme contains

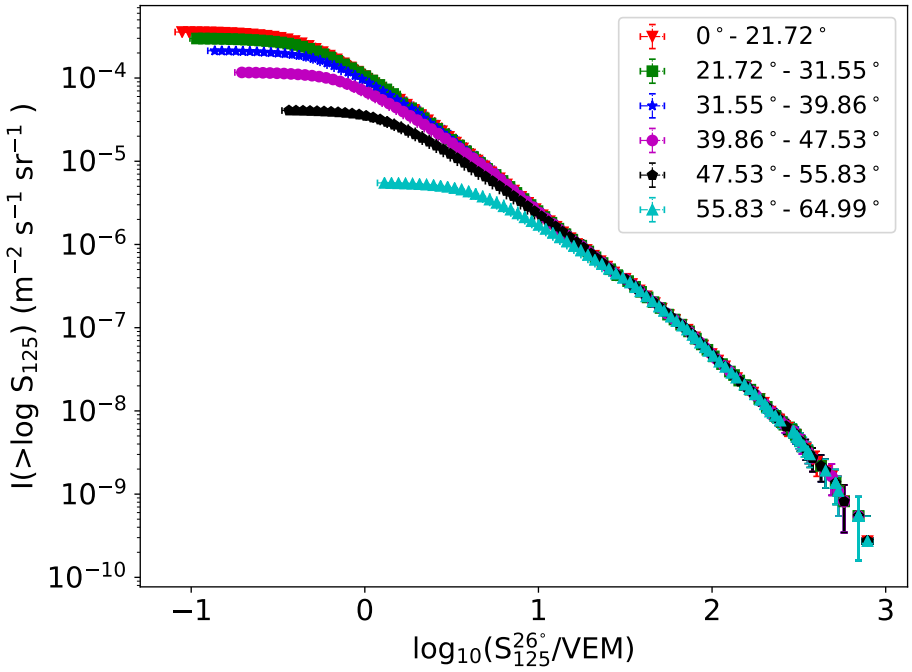

Figure 8.4: The integral flux for different zenith bins with equal $\Delta\cos^2\theta$ as shown in Figure 8.1b, re-scaled in terms of a the shower size at 125 m for a shower with zenith angle 26°. The flux curves above full threshold from these zenith bins now lie on top of each other.

the showers from 55.83° - 64.99°. We see that for the lower values of $\log_{10}S_{125}^{26^\circ}$ in the plot (viz. 1.38,1.39), the intensity is lower for the higher zenith angle bin. The intensities at other $\cos^2\theta$ bins are nearly constant, as should be the case.

For a value of $\log_{10}S_{125}^{26^\circ}$ = 1.43, the intensity of the left-most $\cos^2\theta$ bin is the same as that of the other angles for the year 2012. Therefore, this is the value of $\log_{10}S_{125}^{26^\circ}$ that corresponds to the threshold energy of this zenith bin. From the calibration of IceTop done for zenith angles up to 36°, where simulations are performed for a snow level of 2012, we know that this corresponds to an energy of 23.7 PeV. This means that if a surface-radio array existed at IceCube in the year 2012, it would have been possible to trigger the radio array for showers using IceTop above 23.7 PeV, with full efficiency.

On repeating the same procedure for data from 2013 to 2016, we can find the threshold energy for these years too. The Intensity vs $\cos^2\theta$ plots obtained for these years are also shown in Figure 8.5. It is clear that the threshold value of $\log_{10}S_{125}^{26^\circ}$ changes with each year of data, thereby changing the threshold energy every year. This can be attributed to the growing level of snow on top of the detectors, which causes the electromagnetic component to be absorbed before arriving the detector.

Figure 8.6 shows the variation in the threshold value of $\log_{10}S_{125}^{26^\circ}$ for showers within the zenith angle range of 55.83° - 64.99°. This data sample contains the showers measured at a zenith angle of 61°, in which we are interested. The blue square markers show the threshold values of $\log_{10}S_{125}^{26^\circ}$ obtained for different years of measurement, using the method described above.

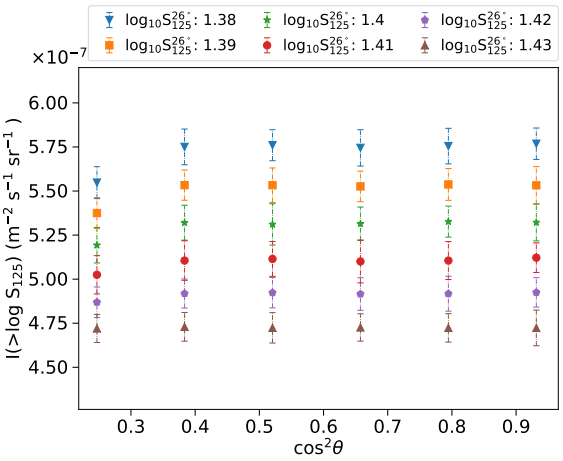

(a) 2012

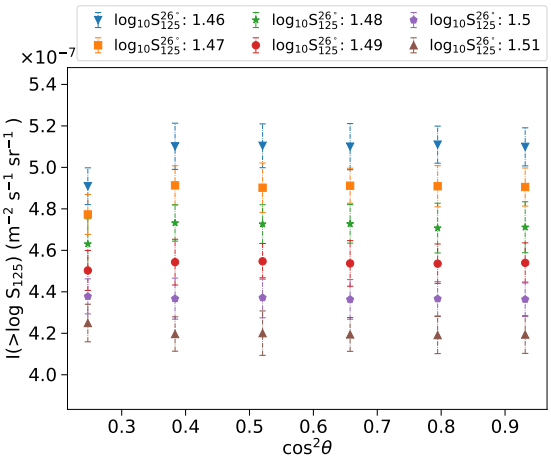

(b) 2013

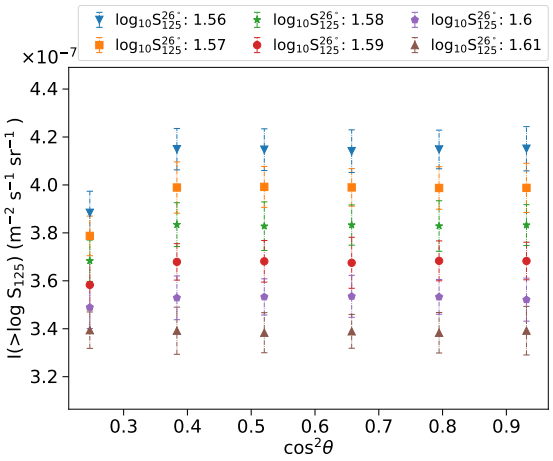

(c) 2014

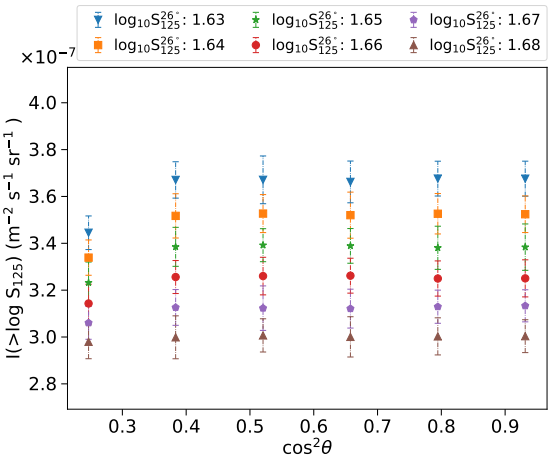

(d) 2015

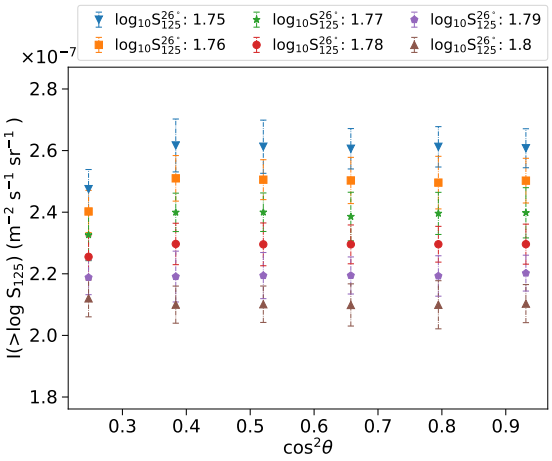

(e) 2016

Figure 8.5: Intensity vs $\cos^2\theta$ for given values of $\log_{10} S_{125}^{26^\circ}$. This is used to find the threshold energy of showers with larger zenith angles where the intensity becomes the same as that of the smaller zenith angles. This threshold is seen to change with the different years of measurement.

Year	Run time (hrs)
2012	56.03
2013	47.98
2014	47.15
2015	50.63
2016	49.71

Table 8.2: The runtime of the data used for applying constant intensity method for each year.

Using the calibration of S_{125} vs energy done for simulations using 2012 level of snow, we can estimate the corresponding threshold energy for all the years of data. This is done by keeping in mind that due to the changing levels of snow on top of the detector, the energy vs shower size calibration will surely change, causing the energy conversion done over here to be erroneous. There is no understanding of the level to which this error effects the estimation. The red dots show the threshold energy obtained for each year of data, using this conversion. The run time of the data used for the threshold estimation for each year is shown in Table 8.2.

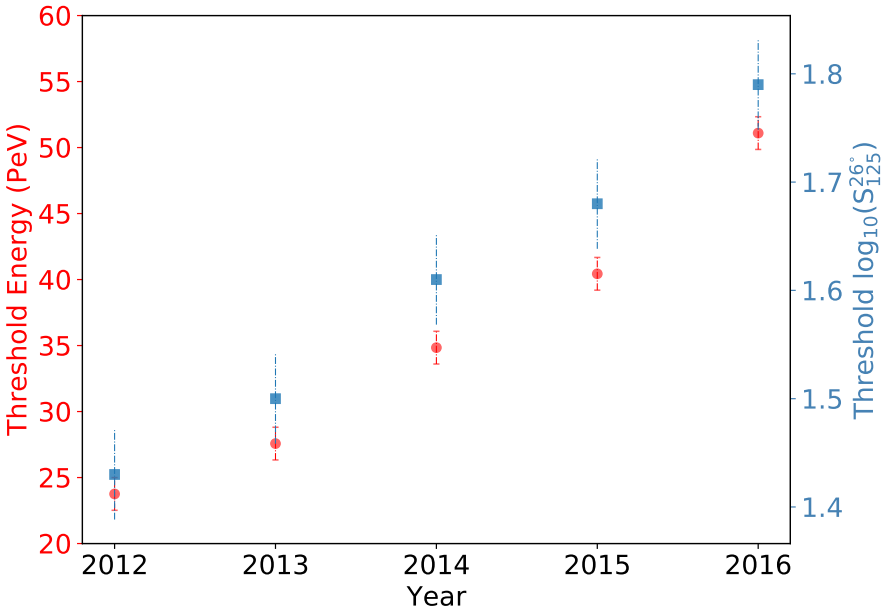

Figure 8.6: The changing value of the threshold $\log_{10} S_{125}^{26^\circ}$ and the corresponding threshold energy shown with blue squares and red dots respectively. This is for showers within a zenith angular range of 55.83° - 64.99°.

A general trend where the threshold energy increases with each year is seen over here. The trend seems to be nearly linear in behaviour. This method of determining the threshold for each year, is also an independent check on the accumulation of snow on top of the detector array, and the corresponding attenuation of the observed signals. It should be noted at this point that this threshold includes "reconstruction effects", since only the showers that could be reconstructed well by the software are

considered over here. This could mean that the absolute trigger threshold is lower than that shown here by around 3-4 PeV. Nevertheless, we see that even for the 2012 data, the full efficiency threshold is at 23 PeV, which is too high for triggering PeV gamma rays coming from 61°.

Since the year 2016, IceTop records measurements of air showers when at least 2 of the infill stations have a signal in them. That is, effectively, 4 tanks have recorded signals. Such a trigger will therefore measure the showers with energies lower than the energy of the showers passing the normal trigger condition. Inclined showers measured by IceTop using the infill trigger were also investigated as a part of this study. However, this data-set proved to be of low stability, especially for the estimation of the energy of inclined showers recorded by this trigger. The existing energy-reconstruction scheme for these showers rely heavily on the inclination of the shower, and can be used only for nearly vertical showers. Therefore, a very detailed study is required to estimate the threshold energy of inclined showers recorded by the infill-trigger, which is beyond the scope of this thesis.

It should be kept in mind that the data from IceTop will consist of showers mainly produced by nuclei with composition ranging from proton to iron. These hadronic showers will have more muons, thereby increasing the number of particles reaching the detector. Gamma-ray showers will therefore have slightly higher energy thresholds (a few PeV) than these cosmic-ray showers.

8.1.2 Gamma-ray simulations with IceTop

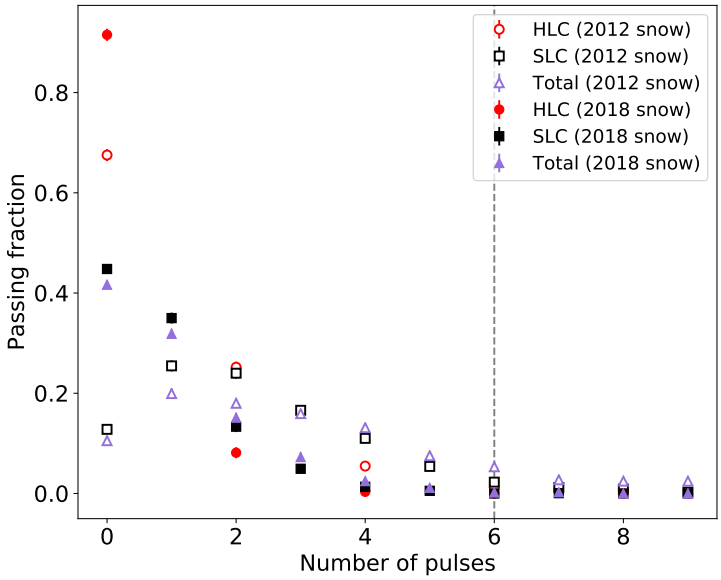

Figure 8.7: Passing fractions for gamma-ray showers with an energy of $10^{15.5}$ eV approaching the IceTop array at a zenith angle of 61°. The simulations are done with snow level of 2012 and and 2018. The grey line represents the 6 HLC pulses (hits in both tanks of a station) condition, which is required for triggering the array. For the level of snow in 2018, no such shower will pass the trigger condition of IceTop. Also for comparison are shown the SLC (one tank in a station) pulses and the total pulses (HLC+SLC).

In order to cross-check the inability of IceTop for triggering gamma rays showers

coming from the Galactic Centre, a few simulations were performed of gamma-ray showers with varying azimuth angles and with core positions lying within 400 m radius from the array centre. These showers have a zenith angle of 61°. Since these showers take a large amount of simulation time, only 30 showers each were simulated using CORSIKA, for each energy. These showers were then re-sampled 50 times while passing through the detector response of IceTop, thereby increasing the statistics. That is, we have 1500 sample showers for each energy. This was done for different levels of snow on top of the detector, taken from the snow measurements of each year. The simulations are done as described in section 3.1.2.

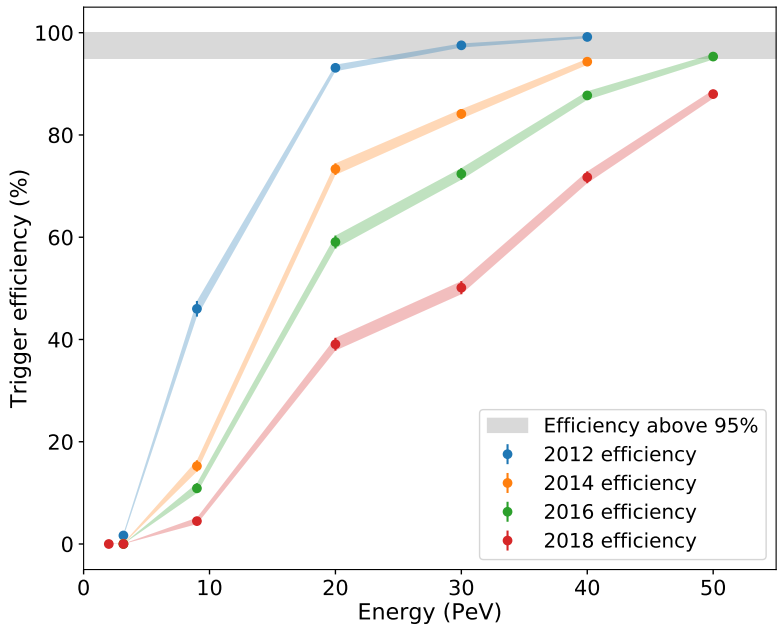

Figure 8.8: Variation in the trigger efficiencies for gamma-ray showers with IceTop as the snow level changes. 6 HLC pulses or more are needed to trigger the array.

Figure 8.7 shows the passing fraction for gamma-ray simulations for the years 2012 and 2018, for showers with an energy of $10^{15.5}$ eV. Here, passing fraction is defined as the fraction of events that pass a given condition. The condition is given by the number of pulses generated in the detector. These could be HLC, SLC or even the total pulses (HLC+SLC). The grey line represents the condition of having 6 HLC pulses, which is the trigger condition of IceTop. It can be seen that for 2012 snow, this trigger condition could be passed a few times. But as the snow increased to the level in 2018, no shower would pass this condition successfully. That is, gamma showers of ≈ 3.16 PeV would not have been triggered by IceTop.

We can see that the passing fraction is maximum when the requirement is to have 2 HLC pulses. For 2012 snow, this is around 30%. Nevertheless, as the snow increases, this goes down to around 10%. Therefore, this also is an unreliable condition. It would be better if both HLC and SLC pulses are considered. That is, to use the entire hit information in all tanks. But this is not done in the normal trigger scheme of IceTop since the amount of data will increase beyond the desired rate.

Figure 8.8 shows the simulated efficiency of the detection of gamma-ray showers for IceTop. If the shower produces 6 or more HLC pulses on the detector array, it is considered to be triggered. This corresponds to all HLC pulses above the grey

line in Figure 8.7. Clearly, we can see that the efficiency of detection is drastically changing due to the snow on top of the detector. Also, even during the year 2012, the showers will be fully triggered only above 20 PeV, which is too high for our purpose. Therefore, we can conclude that IceTop is not ideal as an external trigger for radio detection at PeV energies, for gamma rays coming from the Galactic Centre.

8.2 Scintillators as the external trigger

In a manner similar to that expressed in 8.1.2, gamma-ray showers of various energies that can be detected by the future scintillator array has been simulated. These showers again have a zenith angle corresponding to the arrival direction from the Galactic Centre and differs in its azimuth angles and core positions.

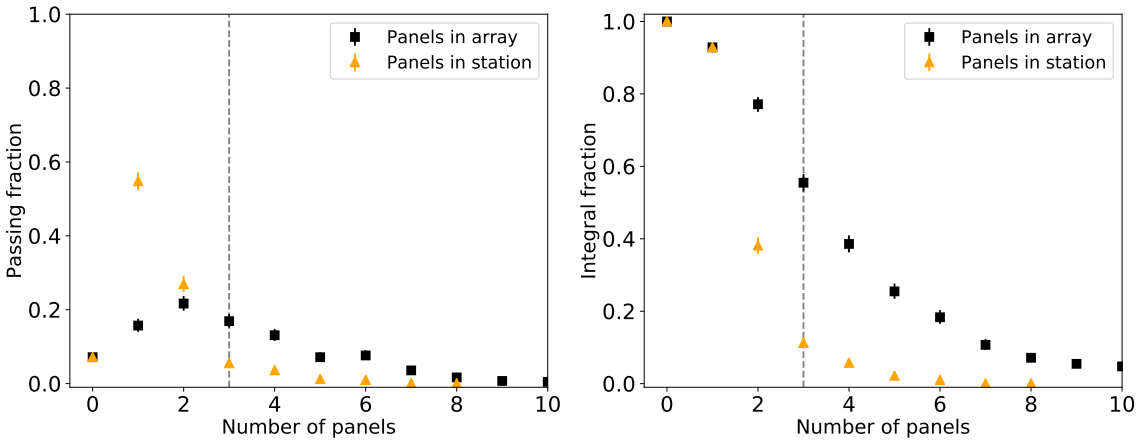

Figure 8.9: Passing fractions for 61° gamma rays of energy 2.5 PeV thrown on the scintillator array (left panel). The integral fractions are shown on the right panel. The grey dashed line shows the number of panels equal to (greater than or equal to) 3 in the left (right) panel.

The simulation routine of the scintillator array that is specifically developed for the IceTop enhancement is utilised over here [138]. The layout of the scintillator array used for the simulations is given in Figure 3.5. The scintillators used in the simulation resemble the structure of the prototype detectors deployed at the Pole during the Austral summer of 2017/2018. These detectors have a length of 1.875 m, a width of 0.8 m and a thickness of 1 cm giving a total sensitive area of 1.5 m^2. That is, their height is low when compared to the IceTop tanks (which have a height of ≈ 1 m). Therefore, there is a significant change in the effective area of a single detector as the shower becomes inclined. This means that the sensitive area is now area $\times$ cosθ. Nevertheless, the denser spacing of the future array can help in increasing the overall sensitive area available in the array, for inclined showers.

The scintillator array is simulated using the Geant4 toolkit [37] that is combined with the IceCube software framework [139] as shown in [39]. A total of 259 scintillators divided into 37 stations with 7 detectors each are simulated on the same footprint as that of IceTop. The signals detected by these scintillators are converted into VEM units (1 VEM is equivalent to an energy deposit of 1.6 MeV for the scintillators). The particles with low energy deposits are ignored in the simulations

since they would not be identified as signals by the system. For this, a cut of 0.5 VEM has been set for the charge deposit [138]. For further details of the scintillator simulation and reconstruction scheme, see [39].

The gamma-ray showers thrown on the scintillator array (produced by CORSIKA) are re-sampled 30 times within a core radius of 400 m (similar to 8.1.2). These showers range in an energy of 0.6 PeV to 10 PeV. The number of panels with signals that are detectable can be looked at for estimating the trigger efficiency of the array. The scintillators could provide a trigger either on a station level or on the level of the entire array. That is, a trigger signal to the antenna array can be sent either when there are 3 panels (e.g.) in a station or when there are 3 panels in the entire array with detectable signals. The passing fractions (number of events with x panels with signals, x being a variable) for both possible formats of the trigger conditions (station or array) are given in the left panel of Figure 8.9. The right panel of the figure shows the integral of the fractions shown in the left panel. That is the number of events with x or more panels with detectable signals. The grey dashed lines show the case when x is 3 in both plots. For the integral case, this line shows the number of events with 3 or more panels that have signals in a station or in the entire array.

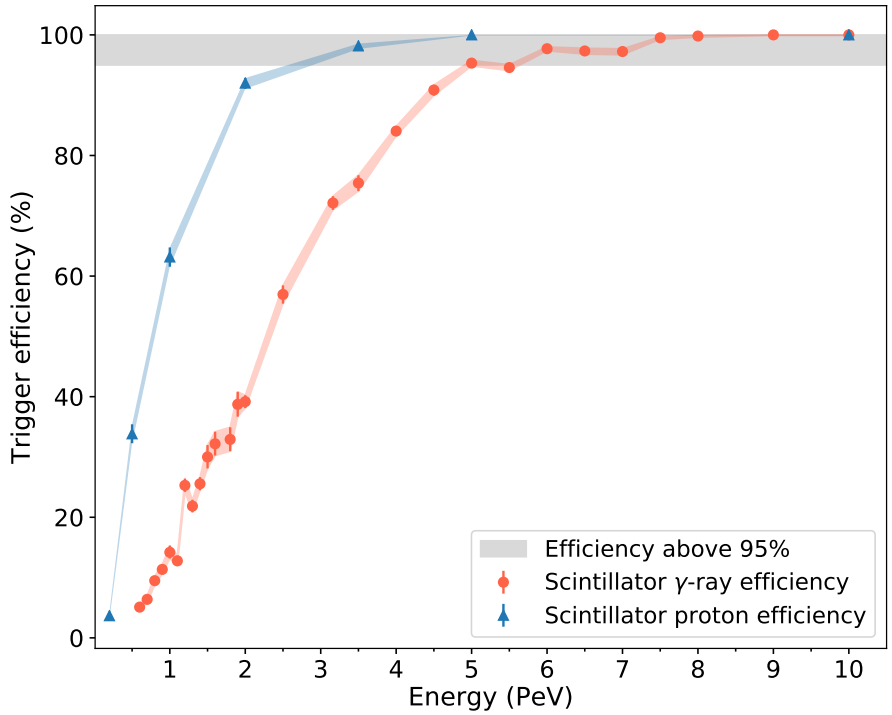

Figure 8.10: Trigger efficiency of the scintillator array for showers produced by gamma rays and protons with $\theta = 61°$. The azimuth angles and cores are randomly chosen.

From Figure 8.9, it is clear that if we trigger on the entire array rather than a single station, the passing fraction is much higher. That is, we can achieve much higher trigger efficiencies by triggering on the entire array (even though technically, it is much easier for the data acquisition to provide a local, station-based trigger). Moreover, 3 panels in an array is a reasonable condition that can avoid coincidences in the panels due to noise. Therefore, a condition of 3 or more panels with signals

in the entire array is looked at for studying the trigger efficiency of the scintillator array for gamma rays coming from the Galactic Centre.

Figure 8.10 shows the efficiency of the scintillator array to trigger gamma-ray showers approaching from 61° of different energies. For comparison, a few proton showers were also simulated with energies ranging from 0.2 PeV to 10 PeV. 30 proton showers each were simulated using CORSIKA and further re-sampled 30 times, resulting in 900 showers for each energy bin. We can see that the gamma-ray showers achieve full efficiency at 8 PeV and an efficiency above 95% at 5 PeV. Proton showers, on the other hand, achieve full efficiency already at 5 PeV and 95% efficiency at around 2.5 PeV. As expected, the scintillator array has much better efficiencies for triggering proton showers than for gamma-ray showers, due to the lower particle content of the inclined gamma showers on the ground. At energies close to 2.2 PeV 50% of the gamma-ray showers coming from the Galactic Centre will be triggered by the scintillators.

We can infer that when compared to the IceTop tanks, the scintillators are much better for triggering the antenna array. Nevertheless, the antenna array can achieve full efficiency already at 1.4 (or 1.1) PeV, for gamma rays from the Galactic Centre, which is much lower than that of the scintillators. This means that we will be heavily limited by the trigger capability of the particle detector array if we rely on external triggering.

8.3 Self-triggering of the antenna array

Under the assumption that the ambient noise condition at the South Pole is low, and mainly Galactic in origin, it may be possible to trigger the antenna array by itself. If the self-trigger efficiency is already high at around 1 PeV, this will be highly advantageous for the detection of gamma rays from the Galactic Centre. An online-interferometric scheme may help in identifying the shower signals from the noise. This would, however, require superior quality of data buffers and sampling. Any concrete estimation of the advantages of such a self-triggering scheme cannot be estimated yet. For this, we need an understanding of the RFI conditions at the South Pole.

Another possible method would be to have a few dedicated antennas that point in the direction of the Galactic Centre. These could provide a trigger to the entire antenna array as soon as an event is observed. The practicality of such a method for triggering the antenna array has to be studied in great detail. In short, the idea of self-triggering the radio array is in a fledgling stage now, and further in-situ measurements at the South Pole are needed to check the feasibility of this.

8.4 Conclusion and remarks

In this chapter, the different possible methods to trigger the radio array have been discussed. It is clear that IceTop will not be a good option as an external trigger, especially due to the increasing levels of snow that accumulates on top of it as each year passes by. Even in the initial stage, in 2012, when there was less snow, IceTop would have been able to trigger gamma rays from the Galactic Centre only from an energy of around 20 PeV. This is too high for our purpose.

We see that scintillators can perform much better in this case. They will be able to trigger from an energy of 5 PeV with a 95% efficiency, for gamma showers from the Galactic Centre. Even-though this is much better than IceTop, it will still limit the gamma ray detection of the radio array (which has a full efficiency from around 1 PeV). Therefore, if scintillators are used as an external trigger, one will have to device other solutions to increase the trigger efficiencies at energies down to a PeV. One way to do this could be with the use of a layer of scintillators that are positioned in an inclined manner, thereby increasing the effective area for inclined showers. Such a scenario should be studied in detail in the future.

If all chances of triggering the antenna array externally will limit its performance at energies close to a PeV, we may have to look into self-trigger systems. Possible methods of implementing a self-trigger was also discussed briefly in this chapter. It is unclear if this would be possible or not. The relatively radio-quiet conditions that are expected at the South Pole could be a positive sign for the success of self-triggering. Nevertheless, future measurements of the radio conditions at the Pole are required to understand the potential of this.

CHAPTER 9

Summary and Outlook

The focus of this thesis has been on devising a method to measure possible PeV gamma rays from the Centre of our Galaxy, using a radio air shower array at the South Pole. This is motivated by the possible PeVatron that was observed by H.E.S.S., near the Centre of the Milky way. The diffuse flux of gamma rays within 10 parsecs of the black hole Sgr A* was seen to have a spectral shape that followed an $E^{-2.32}$ power-law behaviour, extending up to energies of nearly a 100 TeV. The best fit to this spectrum was that without a cut-off energy. Therefore, one can attempt to search for an extension of this spectrum at PeV energies.

The location of IceCube is ideal for such a search due to its continuous exposure to the Galactic Centre at a zenith angle of 61°. Nevertheless, the existing instrumental setup is not sufficient to observe PeV gamma rays coming from such a large inclination. To this effect, it was decided to take advantage of the fact that radio detection of inclined air showers is far superior to that with particle detectors. However, for the detection of PeV gamma rays, the threshold of radio detection had to be lowered by an order of magnitude.

With this goal, it was possible to establish that optimising the frequency range of the radio array to the band 100-190 MHz will enhance the signal-to-noise ratio (SNR) considerably. This was found by scanning the SNR within various possible frequency bands, after conducting detailed studies of the expected radio signals and the noise. Such an improved level of SNR allows the lowering of the energy threshold down to 1.4 PeV for a thermal noise level of 300 K, with a full efficiency of detection. If the antenna has a lower thermal noise (40 K), like that of SKALA which is the candidate antenna for a radio enhancement at the South Pole, a better detection efficiency can be achieved. The use of such antennas will lower the threshold further down to 1.1 PeV with a full detection efficiency. A non-zero efficiency can be achieved for an energy greater than 0.6 PeV for the low thermal noise case, and for an energy greater than 0.7 PeV for a thermal noise of 300 K.

Such low levels of threshold energy is predicted for the first time for a radio air shower experiment. On pushing down the energy threshold, the range of energies over which the radio technique can be used to probe the processes in the Universe widens. With this, air showers with PeV energies can be measured for the first time using the radio technique.

A radio air shower array co-located with IceCube will help us in determining the existence of a PeVatron at the Galactic Centre. A positive detection of PeV gamma rays from this direction will help in determining the flux of gamma rays from this

source. Such a measurement is expected to improve with a longer observation time and will ultimately help in describing the spectral shape more precisely. It can also help in determining the cut-off energy of the candidate accelerator at the Galactic Centre. For the low thermal noise case, a separation factor of 10 is enough for achieving 5σ detection capability within 5 years for an energy above 0.7 PeV, even for a median case of a spectrum with cut-off at 10 PeV. This is even better for fluxes that have a cut-off energy higher than 10 PeV. A higher separation factor will be needed for a flux with a cut-off energy as low as 1 PeV. Therefore, an optimistic sensitivity is expected for the radio array to the flux of PeV gamma rays from the Galactic Centre. On the non-detection of PeV gamma rays from the Galactic Centre, the experiment will be able to establish upper limits to this flux for the first time.

A method of achieving the desired level of gamma-hadron separation factor has to be established using detailed studies, in the future. Such a study can focus on utilising information of the Cherenkov ring, which is directly related to the shower maximum. Gamma-ray showers are in general expected to have deeper showers in the atmosphere than cosmic ray showers. Therefore, this parameter can help in the identification of the particle species. Further separation can be achieved by utilising the muon information of the shower. A combined detection of the particle detectors on the surface, the in-ice detectors and the radio array is expected to help in this separation. Such methods can be utilised in a future study to formulate a scheme to distinguish between showers induced by gamma rays and those induced by hadrons.

The various possible methods of triggering the radio antenna array is also studied as a part of this thesis. It was found that IceTop has too high an energy threshold for showers from the direction of the Galactic Centre to act as an efficient external trigger for the radio antenna array. This was found by using the method of constant intensities on the data that was measured by IceTop in the years 2012 to 2016. The energy at which the intensity falls off for showers within the zenith angle range of 55°-65° was found for each year of data. For showers within this range of inclination, the threshold turns out to be 23 PeV, even for the low snow condition of 2012. The trend with which this threshold energy increases each year, due to the accumulation of snow, was also found out through this. This method is also an independent check on the effect of snow accumulation on top of the IceTop array.

An enhancement of IceTop using scintillator detectors is planned, for calibrating the IceTop array and thereby improving the measurement of air showers at the South Pole. These future scintillators can potentially act as a better alternative for triggering the antenna array externally. The simulated array of scintillators is expected to have a 95% trigger efficiency above 5 PeV for gamma showers from the Galactic Centre. Even though this is better than the IceTop array, it is not low enough to utilise the full capability of the radio array for PeV gamma-ray detection. The possibility of a self-triggered radio array has to be studied in detail. The expected radio-quiet environment at the South Pole can help in this case, as already shown by TREND, which is also located in a radio-quiet location. However, in-situ measurements at the South Pole are required to further understand the feasibility of a self-triggered array.

As a result of the work done in this thesis, a fully operational radio array is planned at the South Pole, as a hybrid installation along with the scintillator array. Such a radio array would require a 10-20% resolution in its energy reconstruction

and 20-30 g/cm^2 resolution in the depth of the shower maximum of the observed air shower. It is already shown by experiments like AERA and LOFAR that this resolution is easily achievable. As a first step towards this radio array, two prototype antennas will be deployed in the Austral summer of 2018/2019. The radio antenna developed for the SKA-low experiment, SKALA, will be used for this. This antenna operates within the frequency band of 50-350 MHz, and therefore includes the optimal band of 100-190 MHz that was determined in this thesis. The signals obtained from the SKALA antenna can be digitally filtered to the optimal band for an enhanced performance and for the detection of PeV gamma rays. The deployed SKALA antennas will be used to measure the noise conditions at the South Pole.

Apart from contributing to the PeVatron search, this radio array will enhance the air shower measurements of IceCube considerably. This array will help in the measurements of the mass composition of the air showers by extracting the complete electromagnetic information of the air shower. In combination with the IceTop array, the scintillators, and the in-ice detectors, this will make up a unique three-dimensional detector at the southern hemisphere, for composition measurements and for the study of hadronic interactions at high energies. The benefits of a hybrid array that includes radio antennas has already been established by experiments like the Pierre Auger Observatory and KASKADE-Grande. Nevertheless, the full extent of a three-dimensional mass-composition instrument at the South pole has to be studied in further detail.

The frequency optimisation performed in this thesis for the purpose of PeVatron search at the Galactic Centre can be done for other locations also. Such an optimisation done for the future installation of GRAND revealed the optimal band to be 100-180 MHz. Similarly, it was also found out to be 100-190 MHz for the location of the Pierre Auger Observatory. This means that this optimal frequency band is universal, and will help in the improvement of the performance of all future radio arrays. The GRAND collaboration has already taken this optimal band into consideration, and plans to operate within the band 50-200 MHz, which includes the optimal band. It has to be noted that the proposed optimal frequency band will be highly beneficial for the observation of inclined showers. Especially, close to the threshold energy, the radio footprint within the optimal band was found to be much larger than that seen with the standard band of 30-80 MHz. This will be highly beneficial for future arrays that focus on the observation of inclined air showers using the radio technique.

Appendix A

Comparison of Noise Models

As a sanity check for the noise model from Cane, that is used in this thesis, a comparison is done with the noise predicted using the Global Sky Model (GSM). Both models operate by using measured data of the Galactic noise at different frequencies, and applying a generic fit to it. GSM is more detailed than the Cane model, and includes directional information of the noise as well. The Cane model averages the noise only from the South and North Galactic Poles. Therefore, a slight lowering in the Galactic noise due to the larger emission from the Centre of the Galaxy is expected for the Cane model.

Here, the noise temperatures obtained from different Galactic coordinates is taken from GSM, for each frequency. This is then averaged out to get the average noise temperature at each frequency. This average noise temperature is then compared between the Cane and GSM models.

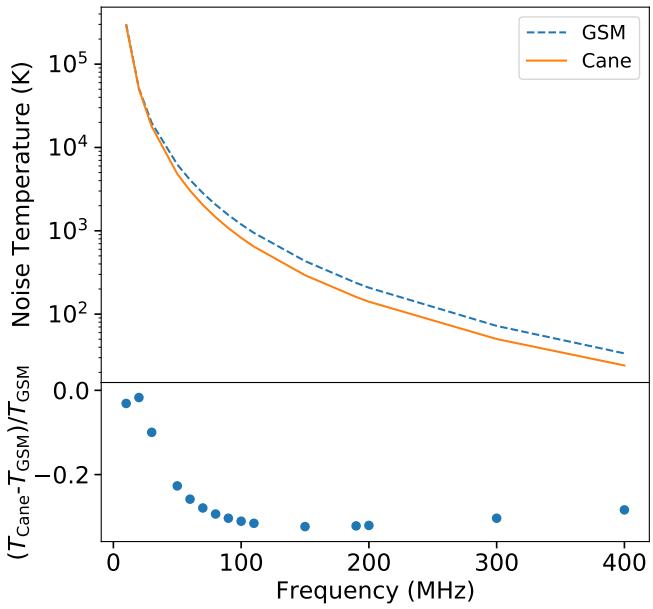

Figure A.1: Comparison of the noise temperature between 2 MHz and 400 MHz predicted by GSM and Cane. The top panel shows the average temperature value and the bottom panel shows the relative difference.

Figure A.1 shows this comparison for frequencies ranging from 2 MHz to 400

MHz. The upper panel shows the noise temperatures from both noise models. The lower panel shows the relative difference in temperatures between the two models, assuming the GSM model to be the true one. It can be seen that the two models agree in the noise temperature values in general. The overall behaviour with frequency is the same for both models. The relative difference ranges from 20% to 38 % 30 MHz to 400 MHz. This difference is even lower for frequencies lower than 30 MHz. This can be accounted to the excess of noise near to the centre of the Galaxy that is included in GSM. However, even with this difference, we can conclude that the variation between the models is low enough. Therefore, we can conclude that the Cane model can be trusted for studying the average behaviour of the noise that can be measured by the antennas.

Appendix B

Antenna Simulation

To extract the voltage traces of the radio signals simulated with CoREAS, a dipole antenna is used. The antenna is simulated using the C++ version of NEC [122]. The dipole antenna is simulated with a length of 2m, and is horizontally oriented 1 m above an infinite ground. The gain and impedance output from NEC were used o construct the antenna response at different frequencies.

The resulting antenna has a resonance at 150 MHz. The effective height of the antenna at various frequencies is shown in Figure B.1. This effective height is folded into the signals obtained from CoREAS, in the frequency space to get the observable amplitude from the air shower.

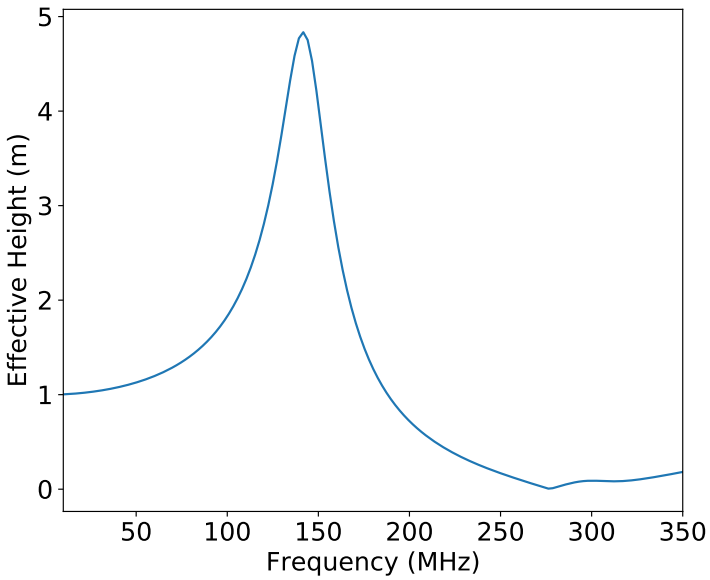

Figure B.1: Frequency dependence of the effective Height of the dipole antenna that was used for the simulations.

APPENDIX C

Frequency Optimization at GRAND and AERA

C.1 GRAND

The **G**iant **R**adio **A**rray for **N**eutrino **D**etection, a planned large-scale radio detector array for neutrino detection aims at measuring ultra-high energy neutrinos, cosmic rays and gamma rays. This array aims on measuring very inclined air showers produced after the interaction of tau neutrinos in the mountain range [23]. The first stage of the array (GRANDProto35) will be installed in the Tianshan valley in China, co-located with TREND. Since the goal is to have a stand-alone radio array that operates without the help of any particle detectors, it is of great importance to have a high-performance radio array. Since the project is still in its development stage, it provides a window of opportunity to aim for a superior performance. Therefore, a frequency-band optimisation, similar to that done for the surface enhancement of IceTop, was done for GRAND.

For this study, the showers were generated using ZHAires [64], with the environment (magnetic field, observation level) similar to that of the GRAND location [140]. The atmosphere is chosen to be the Linsley US standard atmosphere. The magnetic field of the location of TREND is used in these simulations (strength = 56.5000 μT). The signals are produced with a time interval of d$t = 1$ ns, whereas for IceTop simulation it was 0.2 ns. Although the antennas used for GRANDProto35 are butterfly antennas, we use the same dipole antenna used for the simulations in this thesis. In this thesis, we used the dipole antenna response with the effective heights given within a frequency interval of 2.4 Hz, as shown in Appendix B. On the other hand, the GRAND simulations require only a frequency binning of 2.66 MHz, due to the larger time samples in the simulations. So an interpolation of the antenna response obtained for the IceTop simulations (produced with NEC++ [122]) is done. This interpolated response is used to produce signals (Ex, Ey, Ez) in the units of μV.

Two antennas each are used for the EW and NS directions. These are assumed to be kept on a mountain slope of $10°, 20°$ etc. Here, it is assumed that there is no antenna kept in the vertical direction. So the Ez component is not taken into account.

The signals produced in this manner are then used to determine the signal-to-noise ratio (SNR) in different frequency bands. The method is similar to that shown in chapter 6. The noise assumed is an average galactic noise with an additional ther-

mal noise of 300 K (see chapter 5). Since the SNR from the EW and NS polarisations are in power units, they can be directly added up to get the total SNR. This SNR is then compared for various frequency bands.

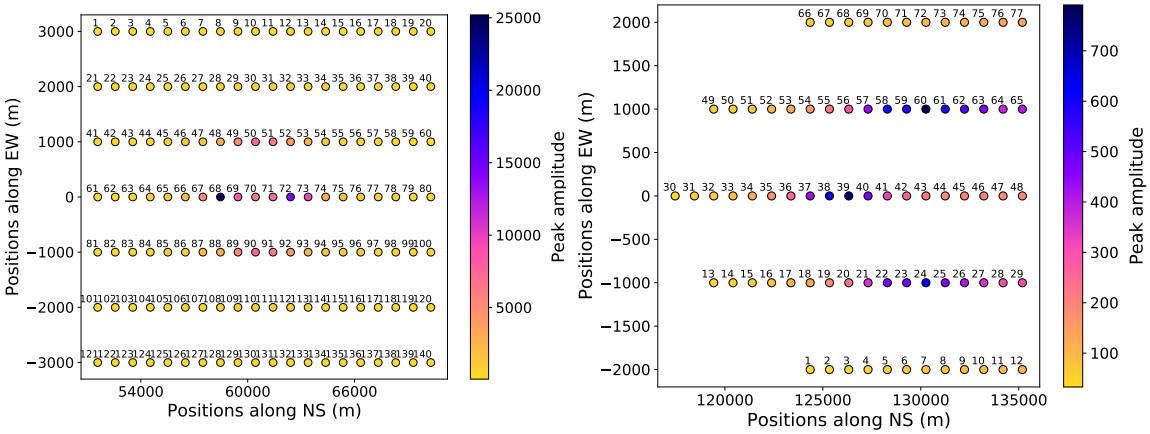

(a) proton, $\theta = 80°, \phi = 0°, E = 10$ EeV

(b) neutrino, $\theta = 93°, \phi = 0°, E = 0.5$ EeV

Figure C.1: The antenna positions used for simulating some example proton and neutrino showers, that are used for the frequency scan. The antennas are located on a slope of $10°$ and are 1 km apart from each other [140].

Figure C.1 shows two example showers that are simulated for the frequency optimisation. The antennas are aligned with a spacing of 1 km and lie on a slope of $10°$. The simulated antenna positions vary for each shower, according to the distance between the array and the first interaction of the shower. The farther the shower is, the larger is the array that is simulated. Figure C.1a has an injection height of 10^6 m and Figure C.1b has 2800 m injection height. Therefore, the former has a larger simulated array than the latter.

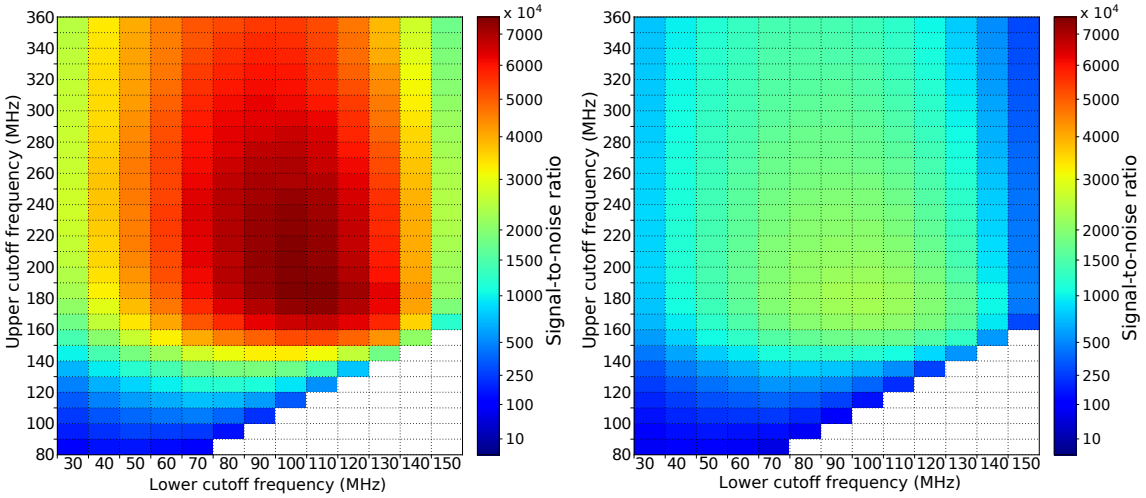

(a) station 68

(b) station 73

Figure C.2: GRAND proton shower of energy 10 EeV and zenith angle $80°$ and azimuth angle $0°$ arriving on antennas placed on a slope of $10°$ as shown in C.1a.

Figure C.2 shows the frequency band scan done for stations 68 and 73 of Figure C.1a. These are the stations on the Cherenkov ring and outside the Cherenkov ring.

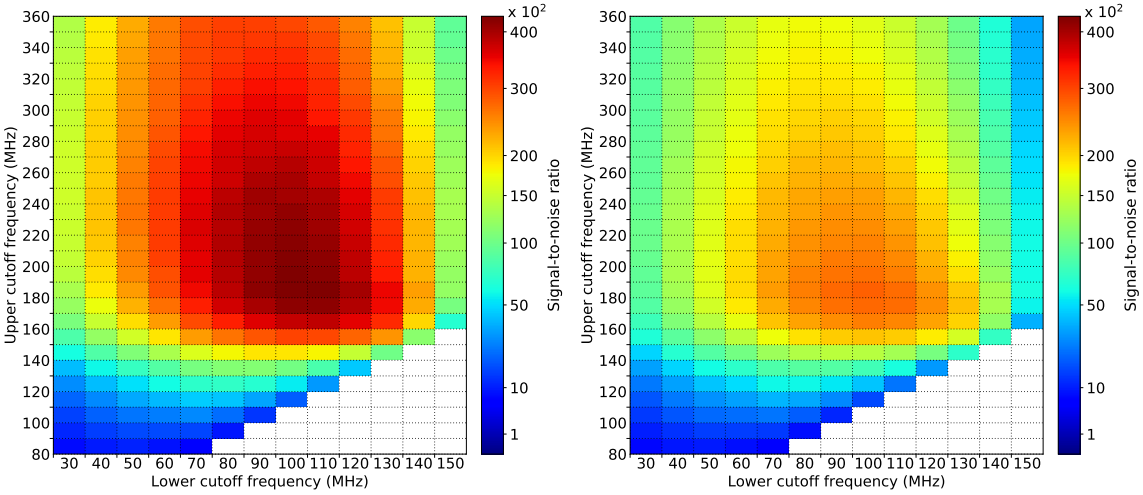

(a) station 68 (b) station 73

Figure C.3: GRAND neutrino shower of energy 5 EeV and zenith angle 87° and azimuth angle 0° arriving on antennas placed on a slope of 10° as shown in C.1a.

Similarly, Figure C.3 shows the frequency band scan done for a neutrino shower, that is shown in C.1b. The scan is shown for stations 38 and 41, which lie on the Cherenkov ring and inside the Cherenkov ring respectively. It is seen that the optimal band for the GRAND location is 100-180 MHz, which is consistent with the optimal band seen for IceTop [23]. This is true for both cosmic rays and neutrinos.

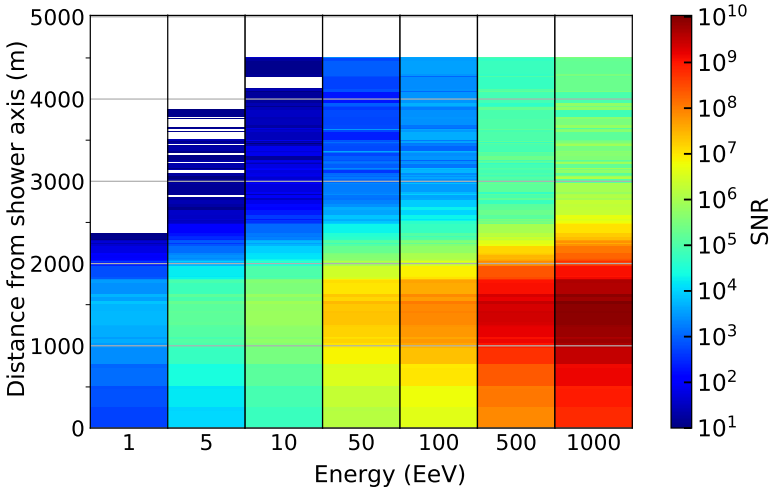

Figure C.4: The changing SNR of proton air showers with energies from 1 EeV to 1000 EeV. Here, $\theta = 85°$, $\phi = 0°$ and the mountain slope is 10°.

Similar to section 6.4.3, the change in the profile of proton showers simulated for the GRAND location was inspected, with the change in energy. For this, showers with energies ranging from 1 EeV to 1000 EeV were simulated. These showers have a zenith angle of 85° and an azimuth of 0°. This is shown in Figure C.4. As in the case of IceTop, we can see that the position of the Cherenkov ring remains the same. The increment in the size of footprint can also be seen as the energy increases. Here,

the energy binning is in larger steps than that for the IceTop simulations, thereby causing the large increase in footprint.

Based on this work, it has been decided that GRAND will operate on the frequency range of 50-200 MHz [23]. On going down to 50 MHz for the lower cutoff frequency, it will be possible to also include the well-studied lower frequencies in the measurements. From measurements with TREND, it is known that the RFI level at the TREND location is very low [91]. This will be very ideal for enhancing the SNR for GRAND with the optimal band.

C.2 The Pierre Auger Upgrade with Radio Antennas

A large-scale radio array is envisioned for the Pierre Auger Observatory in the future. This array aims at measuring horizontal air showers, which leave a large radio footprint on the ground. This array will therefore be able to separate the electromagnetic components with the radio array and the muons with the particle detectors. This will help in mass composition measurements. The radio array that will be used for this is planned to a total area of 3000 km^2 with antennas having a spacing of 1.5 km from each other [86].

A frequency optimisation study for such an array at the AERA location is done here, using the knowledge of the same process that is done for the IceTop-radio enhancement. The simulations used for this were produced to study inclined air showers and their lateral distribution [123]. These simulations were generated with a magnetic field, observation level and atmosphere of the Pierre Auger Observatory. The optimal band with a maximum value of the SNR will remain the same. Therefore, it is justified in using these simulations for our purpose.

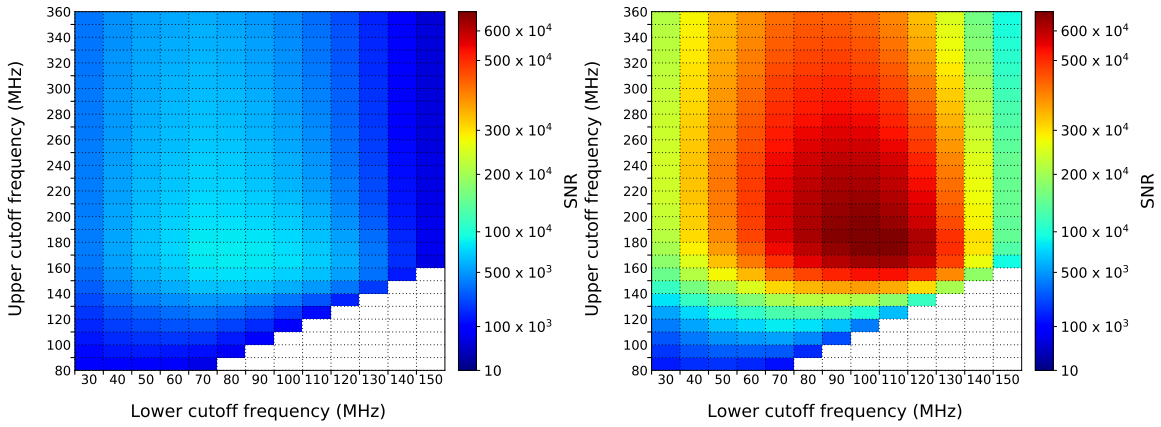

(a) Outside the Cherenkov ring

(b) At the Cherenkov ring

Figure C.5: AERA proton shower of energy 7.5 EeV and zenith angle 80° and azimuth angle 61°.

The simulations used a star shaped array for generating the signals from the shower on the ground. These were generated for the study reported in [123]. Figure C.5 shows the frequency scan for a station at the Cherenkov ring and outside the Cherenkov ring. We see that for the site of AERA also, the optimal band turns out to be 100-190 MHz, consistent with the results obtained for IceTop.

It should be kept in mind that this result is quoted, assuming that only the Galactic noise and the thermal noise of the antenna contribute to the total noise. However, this is not the case for the site at Pierre Auger Observatory. There is a significant amount of RFI reported at AERA. This can also be seen in chapter 5. This RFI noise level may be more in the optimal band reported here, when compared to the traditional frequency band of measurement (30-80 MHz) within which AERA operates. Therefore, a careful study of the noise at higher frequencies at the AERA site is needed to weigh the advantages of one band over the other.

Bibliography

[1] Johannes Blümer, Ralph Engel, and Jörg R. Hörandel. Cosmic rays from the knee to the highest energies. *Progress in Particle and Nuclear Physics*, 63:293--338, October 2009.

[2] M. C. Gonzalez-Garcia, Francis Halzen, and Soumya Mohapatra. Identifying Galactic PeVatrons with Neutrinos. *Astropart. Phys.*, 31:437--444, 2009.

[3] Francis Halzen, Alexander Kappes, and Aongus O Murchadha. Gamma-ray Astronomy with Muons: Sensitivity of IceCube to PeVatrons in the Southern Sky. *Phys. Rev.*, D80:083009, 2009.

[4] Zachary Griffith and Hershal Pandya for the IceCube collaboration. Search for PeV Gamma-Ray Point Sources with IceCube. In *Proceedings, 35th International Cosmic Ray Conference (ICRC 2017)*, 2017. PoS(ICRC2017)715.

[5] A. Abramowski et al. Acceleration of petaelectronvolt protons in the Galactic Centre. *Nature*, 531:476, 2016.

[6] A. Achterberg et al. First Year Performance of The IceCube Neutrino Telescope. *Astropart. Phys.*, 26:155--173, 2006.

[7] T. Huege and A. Haungs. Radio detection of cosmic rays: present and future. *JPS Conf. Proc.*, 9:010018, 2016.

[8] W. B. Atwood et al. The Large Area Telescope on the Fermi Gamma-ray Space Telescope Mission. *Astrophys. J.*, 697:1071--1102, 2009.

[9] M. Tavani et al. The AGILE space mission. *Nucl. Instrum. Meth.*, A588:52--62, 2008.

[10] N. Gehrels et al. The Swift Gamma-Ray Burst Mission. *Astrophys. J.*, 611:1005--1020, 2004. [Erratum: Astrophys. J.621,558(2005)].

[11] K. Bernloehr et al. The optical system of the HESS imaging atmospheric Cherenkov telescopes, Part 1: Layout and components of the system. *Astropart. Phys.*, 20:111--128, 2003.

[12] Jamie Holder et al. The first VERITAS telescope. *Astropart. Phys.*, 25:391--401, 2006.

[13] C. Baixeras et al. Commissioning and first tests of the MAGIC telescope. *Nucl. Instrum. Meth.*, A518:188--192, 2004.

[14] B. S. Acharya et al. Science with the Cherenkov Telescope Array. 2017.

[15] A. U. Abeysekara et al. On the sensitivity of the HAWC observatory to gamma-ray bursts. *Astropart. Phys.*, 35:641--650, 2012.

[16] Robert W. Atkins et al. Milagrito: A TeV air shower array. *Nucl. Instrum. Meth.*, A449:478--499, 2000.

[17] G. Di Sciascio. The LHAASO experiment: from Gamma-Ray Astronomy to Cosmic Rays. *Nucl. Part. Phys. Proc.*, 279-281:166--173, 2016.

[18] Miguel Mostafa, Segev Benzvi, Harm Schoorlemmer, and Fabian Schüssler. On the scientific motivation for a wide field-of-view TeV gamma-ray observatory in the Southern Hemisphere. *PoS*, ICRC2017:851, 2018.

[19] Silvia Vernetto and Paolo Lipari. Absorption of very high energy gamma rays in the Milky Way. *Phys. Rev.*, D94(6):063009, 2016.

[20] Paolo Desiati. IceCube: Toward a km3 Neutrino Telescope. In *Proceedings, 20th European Cosmic Ray Symposium (ECRS 2006): Lisbon, Portugal, September 5-8, 2006*, pages S5--73, 2006.

[21] Piotr Homola. Search for Ultra-High Energy Photons with the Pierre Auger Observatory. *arXiv e-prints*, page arXiv:1804.05613, April 2018.

[22] M. G. Aartsen et al. IceCube-Gen2: A Vision for the Future of Neutrino Astronomy in Antarctica. 2014.

[23] Jaime Álvarez-Muñiz et al. The Giant Radio Array for Neutrino Detection (GRAND): Science and Design. 2018.

[24] P. Allison et al. Design and Initial Performance of the Askaryan Radio Array Prototype EeV Neutrino Detector at the South Pole. *Astropart. Phys.*, 35:457--477, 2012.

[25] W. D. Apel et al. KASCADE-Grande Limits on the Isotropic Diffuse Gamma-Ray Flux between 100 TeV and 1 EeV. *Astrophys. J.*, 848(1):1, 2017.

[26] Hershal Pandya and Zachary Griffith for the IceCube collaboration. Search for diffuse gamma-ray emission from the Galactic plane with IceCube. In *Proceedings, 35th International Cosmic Ray Conference (ICRC 2017)*, 2017. PoS(ICRC2017)705.

[27] Yasunobu Uchiyama, Stefan Funk, Hideaki Katagiri, Junichiro Katsuta, Marianne Lemoine-Goumard, Hiroyasu Tajima, Takaaki Tanaka, and Diego F. Torres. Fermi Large Area Telescope Discovery of GeV Gamma-Ray Emission from the Vicinity of SNR W44. *APJ*, 749:L35, April 2012.

[28] R. Abbasi et al. IceTop: The surface component of IceCube. *Nucl. Instrum. Meth.*, A700:188--220, 2013.

[29] R. Abbasi et al. The IceCube Data Acquisition System: Signal Capture, Digitization, and Timestamping. *Nucl. Instrum. Meth.*, A601:294--316, 2009.

[30] R. Abbasi et al. The Design and Performance of IceCube DeepCore. *Astropart. Phys.*, 35:615--624, 2012.

[31] S. Klepser. *Reconstruction of Extensive Air Showers and Measurement of the Cosmic Ray Energy Spectrum in the Range of 1 – 80 PeV at the South Pole*. PhD thesis, Humboldt-Universität zu Berlin, 2008.

[32] K. Rawlins. Cosmic ray spectrum and composition from three years of IceTop and IceCube. *J. Phys. Conf. Ser.*, 718(5):052033, 2016.

[33] K. Rawlins for the IceCube collaboration. A Function to Describe Attenuation of Cosmic Ray Air Shower Particles in Snow. In *Proceedings, 34th International Cosmic Ray Conference (ICRC 2015)*, 2015. PoS(ICRC2015)0628.

[34] D. Heck, G. Schatz, T. Thouw, J. Knapp, and J. N. Capdevielle. CORSIKA: A Monte Carlo code to simulate extensive air showers. 1998. FZKA-6019.

[35] Alfredo Ferrari, Paola R. Sala, Alberto Fasso, and Johannes Ranft. FLUKA: A multi-particle transport code (Program version 2005). 2005.

[36] Eun-Joo Ahn, Ralph Engel, Thomas K. Gaisser, Paolo Lipari, and Todor Stanev. Cosmic ray interaction event generator sibyll 2.1. *Phys. Rev. D*, 80:094003, Nov 2009.

[37] S. Agostinelli et al. GEANT4: A Simulation toolkit. *Nucl. Instrum. Meth.*, A506:250--303, 2003.

[38] S. Kunwar T. Huber, J. Kelley and D. Tosi for the IceCube-Gen2 collaboration. The IceTop Scintillator Upgrade. In *Proceedings, 35th International Cosmic Ray Conference*, 2017. PoS(ICRC 2017)401.

[39] A. Leszczyńska for the IceCube-Gen2 collaboration. Simulation study for the IceTop enhancement with a scintillator array. In *Proceedings of the 26th Extended European Cosmic Ray Symposium and 35th Russian Cosmic Ray Conference (E+CRS 2018)*, volume in press, 2018.

[40] Jan Auffenberg the IceCube-Gen2 collaboration. IceAct: Imaging Air Cherenkov Telescopes with SiPMs at the South Pole for IceCube-Gen2. In *Proceedings, 35th International Cosmic Ray Conference*, 2017. PoS(ICRC2017)1055.

[41] David Seckel. Cosmic Ray Science Potential for an Extended Surface array at the IceCube Observatory. In *Proceedings, 34th International Cosmic Ray Conference: The Hague, The Netherlands, July 30-August 6*, 2015. PoS(ICRC 2015)694.

[42] J. van Santen for the IceCube-Gen2 collaboration. IceCube-Gen2: the next-generation neutrino observatory for the South Pole. In *Proceedings, 35th International Cosmic Ray Conference*, 2017. PoS(ICRC 2017)991.

[43] A. Haungs, H. Rebel, and M. Roth. Energy spectrum and mass composition of high-energy cosmic rays. *Rept. Prog. Phys.*, 66:1145--1206, 2003.

[44] Ralph Engel, Dieter Heck, and Tanguy Pierog. Extensive air showers and hadronic interactions at high energy. *Annual Review of Nuclear and Particle Science*, 61(1):467--489, 2011.

[45] Hershal Pandya for the IceCube collaboration. A composition sensitive log-likelihood ratio for cosmic rays and gamma rays. In *Proceedings, 35th International Cosmic Ray Conference (ICRC 2017)*, 2017. PoS(ICRC2017)514.

[46] W. Heitler. *Quantum theory of radiation*. 1954.

[47] Ralph Engel, Dieter Heck, and Tanguy Pierog. Extensive air showers and hadronic interactions at high energy. *Ann. Rev. Nucl. Part. Sci.*, 61:467--489, 2011.

[48] J. Blumer. Cosmic rays at the highest energies and the Pierre Auger Observatory. *J. Phys.*, G29:867--879, 2003.

[49] J. V. Jelley, J. H. Fruin, N. A. Porter, T. C. Weekes, F. G. Smith, and R. A. Porter. Radio Pulses from Extensive Cosmic-Ray Air Showers. *Nature*, 205:327--328, jan 1965.

[50] H. Schoolemmer. *Tuning in on cosmic rays*. PhD thesis, Radboud Universiteit Nijmegen, 2012.

[51] Krijn D. de Vries, Olaf Scholten, and Klaus Werner. Macroscopic Geo-Magnetic Radiation Model: Polarization effects and finite volume calculations. *Nucl. Instrum. Meth.*, A662:S175--S178, 2012.

[52] O. Scholten, K. Werner, and F. Rusydi. A Macroscopic Description of Coherent Geo-Magnetic Radiation from Cosmic Ray Air Showers. *Astropart. Phys.*, 29:94--103, 2008.

[53] G.A. Askaryan. Excess negative charge of an electron-photon shower and the coherent radio emission from it. *Soviet Phys. JETP*, Vol: 14:441, 1962.

[54] G.A. Askaryan. Coherent radio emission from cosmic showers in air and in dense media. *Soviet Phys. JETP*, Vol: 21:658, 1965.

[55] K. D. de Vries, A. M. van den Berg, O. Scholten, and K. Werner. Coherent Cherenkov Radiation from Cosmic-Ray-Induced Air Showers. *Phys. Rev. Lett.*, 107:061101, 2011.

[56] A. Zilles. *Emission of Radio Waves in Particle Showers: Validation of microscopic simulations with the SLAC T-510 experiment and their potential in the future Square Kilometre Array*. PhD thesis, Karlsruhe Institute of Technology, 2016.

[57] Thierry Gousset, Olivier Ravel, and Christelle Roy. Are vertical cosmic rays the most suitable to radio detection? *Astroparticle Physics*, 22(1):103 -- 107, 2004.

[58] Olga Kambeitz. Measurement of horizontal air showers with the Auger Engineering Radio Array. *EPJ Web Conf.*, 135:01015, 2017.

[59] Krijn D. de Vries, Olaf Scholten, and Klaus Werner. The eva code: Macroscopic modeling of radio emission from air showers based on full mc simulations including a realistic index of refraction. *AIP Conference Proceedings*, 1535(1):133--137, 2013. 5TH INTERNATIONAL WORKSHOP ON ACOUSTIC AND RADIO EEV NEUTRINO DETECTION ACTIVITIES: ARENA 2012.

[60] T. Huege. Radio detection of cosmic ray air showers in the digital era. *Phys. Rept.*, 620:1--52, 2016.

[61] E. Zas, F. Halzen, and T. Stanev. Electromagnetic pulses from high-energy showers: Implications for neutrino detection. *Phys. Rev. D*, 45:362--376, Jan 1992.

[62] M. Ludwig and T. Huege. REAS3: Monte Carlo simulations of radio emission from cosmic ray air showers using an "end-point" formalism. *Astroparticle Physics*, 34:438--446, January 2011.

[63] S. J. Sciutto. AIRES: A System for air shower simulations. User's guide and reference manual. Version 2.2.0. 1999.

[64] J. Alvarez-Muñiz, W. R. Carvalho, and E. Zas. Monte Carlo simulations of radio pulses in atmospheric showers using ZHAireS. *Astroparticle Physics*, 35:325--341, January 2012.

[65] T. Huege, M. Ludwig, and C. W. James. Simulating radio emission from air showers with CoREAS. *AIP Conf. Proc.*, 1535:128, 2013.

[66] K. Bechtol A. Zilles, K. Belov et al. Modelling of radio emis- sion in the SLAC T-510 experiment using microscopic Geant4 simulations. In *Proceedings, 34th International Cosmic Ray Conference (ICRC 2015)*, 2015. PoS(ICRC2015)313.

[67] W. D. Apel et al. Improved absolute calibration of LOPES measurements and its impact on the comparison with REAS 3.11 and CoREAS simulations. *Astropart. Phys.*, 75:72--74, 2016.

[68] W. D. Apel et al. A comparison of the cosmic-ray energy scales of Tunka-133 and KASCADE-Grande via their radio extensions Tunka-Rex and LOPES. *Phys. Lett.*, B763:179--185, 2016.

[69] Anne Zilles. Geant4 simulations of radio signals from particle showers for the SLAC T-510 experiment. 2017.

[70] A. Nelles et al. Measuring a Cherenkov ring in the radio emission from air showers at 110–190 MHz with LOFAR. *Astropart. Phys.*, 65:11--21, 2015.

[71] S. W. Barwick et al. Radio detection of air showers with the ARIANNA experiment on the Ross Ice Shelf. *Astropart. Phys.*, 90:50--68, 2017.

[72] P Abreu et al. Antennas for the detection of radio emission pulses from cosmic-ray induced air showers at the Pierre Auger Observatory. *Journal of Instrumentation*, 7(10):P10011, 2012.

[73] F. G. Schröder et al. Tunka-Rex: a Radio Extension of the Tunka Experiment. *J. Phys. Conf. Ser.*, 409(1):012076, 2013.

[74] Lilian Martin et al. Main features of cosmic ray induced air showers measured by the CODALEMA experiment. In *Proceedings, 35th International Cosmic Ray Conference (ICRC 2017)*, 2017. PoS(ICRC2017)414.

[75] P. Schellart et al. Detecting cosmic rays with the LOFAR radio telescope. *Astron. Astrophys.*, 560:A98, 2013.

[76] H. Falcke et al. Detection and imaging of atmospheric radio flashes from cosmic ray air showers. *Nature*, 435:313--316, 2005.

[77] Jelena Petrovic et al. Radio emission of highly inclined cosmic ray air showers measured with LOPES. In *Proceedings, 29th International Cosmic Ray Conference (ICRC 2005) - by Forschungszentrum Karlsruhe, Institute for Nuclear Physics, and University Karlsruhe, Institute for Experimental Nuclear Physics: Pune, India, August 3-11, 2005*, volume 6, pages 337--340, 2006.

[78] D. Ardouin et al. Radio-Detection Signature of High Energy Cosmic Rays by the CODALEMA Experiment. *Nucl. Instrum. Meth.*, A555:148, 2005.

[79] Diego Torres Machado. Latest results of the CODALEMA experiment: cosmic rays radio detection in a self trigger mode. *J. Phys. Conf. Ser.*, 409(1):012074, 2013.

[80] M. P. van Haarlem et al. LOFAR: The LOw-Frequency ARray. *Astron. Astrophys.*, 556:A2, 2013.

[81] S. Buitink et al. Method for high precision reconstruction of air shower X_{max} using two-dimensional radio intensity profiles. *Phys. Rev.*, D90(8):082003, 2014.

[82] S. Buitink et al. A large light-mass component of cosmic rays at $10^{17} - 10^{17.5}$ eV from radio observations. *Nature*, 531:70, 2016.

[83] Alexander Aab et al. The Pierre Auger Cosmic Ray Observatory. *Nucl. Instrum. Meth.*, A798:172--213, 2015.

[84] S. Argiro, S. L. C. Barroso, J. Gonzalez, L. Nellen, Thomas Cantzon Paul, T. A. Porter, L. Prado, Jr., M. Roth, R. Ulrich, and D. Veberic. The Offline Software Framework of the Pierre Auger Observatory. *Nucl. Instrum. Meth.*, A580:1485--1496, 2007.

[85] P. Abreu et al. Advanced functionality for radio analysis in the Offline software framework of the Pierre Auger Observatory. *Nuclear Instruments and Methods in Physics Research A*, 635:92--102, April 2011.

[86] Jörg Hörandel for the Pierre Auger Collaboration", title = "A large radio array at the Pierre Auger Observatory. In *Proceedings of the 8th international workshop on Acoustic and Radio EeV Neutrino Detection Activities (ARENA 2018)*, volume in press, 2018.

[87] P. A. Bezyazeekov et al. Measurement of cosmic-ray air showers with the Tunka Radio Extension (Tunka-Rex). *Nucl. Instrum. Meth.*, A802:89--96, 2015.

[88] Frank G. Schröder. Radio detection of Cosmic-Ray Air Showers and High-Energy Neutrinos. *Prog. Part. Nucl. Phys.*, 93:1--68, 2017.

[89] P. A. Bezyazeekov et al. Radio measurements of the energy and the depth of the shower maximum of cosmic-ray air showers by Tunka-Rex. *JCAP*, 1601(01):052, 2016.

[90] Tim Huege et al. High-precision measurements of extensive air showers with the SKA. *PoS*, ICRC2015:309, 2016. [34,309(2015)].

[91] Olivier Martineau-Huynh for the TREND collaboration. Status of the TREND project. *arXiv e-prints*, page arXiv:1204.1599, April 2012.

[92] GRAND Collaboration, Jaime Alvarez-Muniz, Rafael Alves Batista, Aswathi Balagopal V., Julien Bolmont, Mauricio Bustamante, Washington R. Carvalho, Didier Charrier, Ismael Cognard, Valentin Decoene, Peter B. Denton, Sijbrand J. De Jong, Krijn D. De Vries, Ralph Engel, Ke Fang, Chad Finley, Stefano Gabici, QuanBu Gou, Junhua Gu, Claire Guépin, Hongbo Hu, Yan Huang, Kumiko Kotera, Sandra Le Coz, Jean-Philippe Lenain, Guo-Liang Lu, Olivier Martineau-Huynh, Miguel Mostafá, Fabrice Mottez, Kohta Murase, Valentin Niess, Foteini Oikonomou, Tanguy Pierog, Xiangli Qian, Bo Qin, Duan Ran, Nicolas Renault-Tinacci, Markus Roth, Frank G. Schröder, Fabian Schüssler, Cyril Tasse, Charles Timmermans, Matias Tueros, Xiangping Wu, Philippe Zarka, Andreas Zech, B. Theodore Zhang, Jianli Zhang, Yi Zhang, Qian Zheng, and Anne Zilles. The Giant Radio Array for Neutrino Detection (GRAND): Science and Design. *arXiv e-prints*, page arXiv:1810.09994, October 2018.

[93] S. W. Barwick et al. Constraints on cosmic neutrino fluxes from the anita experiment. *Phys. Rev. Lett.*, 96:171101, 2006.

[94] S. Hoover et al. Observation of Ultra-high-energy Cosmic Rays with the ANITA Balloon-borne Radio Interferometer. *Phys. Rev. Lett.*, 105:151101, 2010.

[95] S. W. Barwick et al. A First Search for Cosmogenic Neutrinos with the ARIANNA Hexagonal Radio Array. *Astropart. Phys.*, 70:12--26, 2015.

[96] P. Allison et al. Performance of two Askaryan Radio Array stations and first results in the search for ultrahigh energy neutrinos. *Phys. Rev.*, D93(8):082003, 2016.

[97] R. Bard et al. Design and Performance of an Interferometric Trigger Array for Radio Detection of High-Energy Neutrinos. 2018.

[98] Sebastian Böser. Prospects for a radio air-shower detector at the South Pole. *AIP Conf. Proc.*, 1535(1):116, 2013.

[99] Sebastian Böser and IceCube Collaboration. A Radio Air-Shower Test Array (RASTA) for IceCube. *Nuclear Instruments and Methods in Physics Research A*, 662:S66--S68, January 2012.

[100] Sebastian Boser. A Radio Air-Shower Test Array (RASTA) for IceCube. *Nucl. Instrum. Meth.*, A662:S66--S68, 2012.

[101] Frank G. Schröder. Physics Potential of a Radio Surface Array at the South Pole (ARENA 2018). In *Acoustic and Radio EeV Neutrino Detection Activities (ARENA 2018) Catania, Italy, June 12-15, 2018*, 2018.

[102] E. Holt. *Combined Detection of Muons and Radio Emission of Cosmic-Ray Air Showers*. PhD thesis, Karlsruhe Institute of Technology, 2018.

[103] M. G. Aartsen et al. Anisotropy in Cosmic-ray Arrival Directions in the Southern Hemisphere Based on six Years of Data From the Icecube Detector. *Astrophys. J.*, 826(2):220, 2016.

[104] Alexander Aab et al. Observation of a Large-scale Anisotropy in the Arrival Directions of Cosmic Rays above 8×10^{18} eV. *Science*, 357(6537):1266--1270, 2017.

[105] W. D. Apel et al. Kneelike structure in the spectrum of the heavy component of cosmic rays observed with KASCADE-Grande. *Phys. Rev. Lett.*, 107:171104, 2011.

[106] Alexander Aab et al. Combined fit of spectrum and composition data as measured by the Pierre Auger Observatory. *JCAP*, 1704(04):038, 2017. [Erratum: JCAP1803,no.03,E02(2018)].

[107] A. Balagopal V., A. Haungs, T. Huege, and F. G. Schröder. Search for PeVatrons at the Galactic Center using a radio air-shower array at the South Pole. *Eur. Phys. J.*, C78(2):111, 2018.

[108] E. de Lera Acedo, N. Razavi-Ghods, N. Troop, N. Drought, and A. J. Faulkner. SKALA, a log-periodic array antenna for the SKA-low instrument: design, simulations, tests and system considerations. *Experimental Astronomy*, 39:567--594, October 2015.

[109] M. Renschler et al. Detector developements for a hybrid particle and radio array for cosmic-ray air-shower detection. In *Proceedings of the 26th Extended European Cosmic Ray Symposium and 35th Russian Cosmic Ray Conference (E+CRS 2018)*, volume in press, 2018.

[110] International Telecomunication Union. Recommendation. ITU-R:P.372--12, 2015.

[111] Angelica de Oliveira-Costa, Max Tegmark, B. M. Gaensler, Justin Jonas, T. L. Landecker, and Patricia Reich. A model of diffuse Galactic Radio Emission from 10 MHz to 100 GHz. *Mon. Not. Roy. Astron. Soc.*, 388:247, 2008.

[112] H. V. Cane. Spectra of the non-thermal radio radiation from the galactic polar regions. *Monthly Notices of the Royal Astronomical Society*, 189:465--478, 1979.

[113] E. Polisensky. LFmap: a low frequency sky map generating program. Long Wavelength Array (LWA) Memo Ser.:111, 2007.

[114] Michael Duvernois. The Radio Air Shower Test Array (RASTA)- Enhancing the IceCube observatory. In *Proceedings, 32nd International Cosmic Ray Conference (ICRC 2011)*, volume 3, page 251.

[115] M. G. Aartsen et al. The IceCube Neutrino Observatory Part VI: Ice Properties, Reconstruction and Future Developments. In *Proceedings, 33rd International Cosmic Ray Conference (ICRC2013): Rio de Janeiro, Brazil, July 2-9, 2013*, 2013.

[116] Tim Huege. Private communication.

[117] Pedro Abreu et al. Antennas for the Detection of Radio Emission Pulses from Cosmic-Ray. *JINST*, 7:P10011, 2012.

[118] Dmitriy Kostunin. Private communication.

[119] A. Balagopal V., A. Haungs, T. Huege, and F. G. Schröder. PeVatron Search Using Radio Measurements of Extensive Air Showers at the South Pole. In *Proceedings of the XV International Conference on Topics in Astroparticle and Underground Physics (TAUP 2017)*, volume in press, 2017.

[120] A. Balagopal V., A. Haungs, T. Huber, T. Huege, M. Kleifges, M. Renschler, H.Schieler, F. G. Schröder, and A. Weindl. A Surface Radio Array for the Enhancement of IceTop and its Science Prospects. In *Proceedings of the 8th international workshop on Acoustic and Radio EeV Neutrino Detection Activities (ARENA 2018)*, volume in press, 2018.

[121] Felix Riehn, Ralph Engel, Anatoli Fedynitch, Thomas K. Gaisser, and Todor Stanev. A new version of the event generator Sibyll. *PoS*, ICRC2015:558, 2016.

[122] Timothy C.A. Molteno. NEC2++: An NEC-2 compatible Numerical Electromagnetics Code. Technical Report ISSN 1172-496X, Electronics Technical Reports No. 2014-3, October 2014.

[123] T. Huege, L. Brenk, and F. Schlüter. A Rotationally Symmetric Lateral Distribution Function for Radio Emission from Inclined Air Showers. *ArXiv e-prints*, August 2018.

[124] Leon Cohen. *Time-Frequency Analysis*. 1995.

[125] Alexander Aab et al. Energy Estimation of Cosmic Rays with the Engineering Radio Array of the Pierre Auger Observatory. *Phys. Rev.*, D93(12):122005, 2016.

[126] M. G. Labate, P. Dewdney, R. Braun, M. Waterson, and J. Wagg. The SKA low-frequency telescope: Performance parameters and constraints on the array configuration. In *2017 11th European Conference on Antennas and Propagation (EUCAP)*, pages 2259--2263, March 2017.

[127] Christian Glaser, Martin Erdmann, Jörg R. Hörandel, Tim Huege, and Johannes Schulz. Simulation of Radiation Energy Release in Air Showers. *JCAP*, 1609(09):024, 2016.

[128] Markus Ahlers. Private communication.

[129] M. G. Aartsen et al. The IceCube Neutrino Observatory - Contributions to ICRC 2015 Part III: Cosmic Rays. 2015.

[130] A. Corstanje et al. The shape of the radio wavefront of extensive air showers as measured with LOFAR. *Astropart. Phys.*, 61:22--31, 2015.

[131] Pedro Abreu et al. Results of a Self-Triggered Prototype System for Radio-Detection of Extensive Air Showers at the Pierre Auger Observatory. *JINST*, 7:P11023, 2012.

[132] Richard Dallier. Multi-scale and multi-frequency studies of cosmic ray air shower radio signals at the CODALEMA site. *PoS*, ICRC2015:293, 2016.

[133] Sandra Le Coz et al. Detection of Extensive Air Showers with the self-triggered TREND radio array. *PoS*, ICRC2017:406, 2018.

[134] D. Ardouin et al. First detection of extensive air showers by the TREND self-triggering radio experiment. *Astropart. Phys.*, 34:717--731, 2011.

[135] X. Bai, T. K. Gaisser, A. Karle, K. Rawlins, G. M. Spiczak, and Todor Stanev. Muon flux at the geographical south pole. *Astropart. Phys.*, 25:361--367, 2006.

[136] D. M. Edge, A. C. Evans, H. J. Garmston, R. J. O. Reid, A. A. Watson, J. G. Wilson, and A. M. Wray. The cosmic ray spectrum at energies above 10-to-the-17 ev. *J. Phys.*, A6:1612--1634, 1973.

[137] Markus Roth. Measurement of the UHECR energy spectrum using data from the surface detector of the Pierre Auger Observatory. In *Proceedings, 30th International Cosmic Ray Conference (ICRC 2007): Merida, Yucatan, Mexico, July 3-11, 2007*, volume 4, pages 327--330, 2007.

[138] Agnieszka Leszczyńska. Private communication.

[139] R. Abbasi et al. All-particle cosmic ray energy spectrum measured with 26 IceTop stations. *Astropart. Phys.*, 44:40--58, 2013.

[140] Anne Zilles. Private communication.

List of Figures

Acknowledgements

First of all, I am grateful to my referee Prof. Johannes Blümer and my co-referee Prof. Thomas Schwetz-Mangold for offering me the opportunity and support to work on this PhD project.

My deepest gratitude to Andreas Haungs, my supervisor, for his immense amount of support and understanding throughout the course of my PhD. I have learnt so much under your guidance Andy: from physics to the different aspects of life in science, and most importantly how to always have a sense of humour. Thank you so much for providing me with this wonderful opportunity to work at KIT. It wouldn't have been possible without you.

I am indebted to Frank Schröder for the deep discussions and extremely useful inputs. Thanks for always supporting me, for taking the time to answer my questions and for pushing me towards the right direction.

I would like to thank everyone at IKP for the wonderful company and discussions, especially to the members of the Cosmic Ray Technologies group at KIT. Thanks to Tim Huege, Timo Karg, Larissa Paul, and the members of the cosmic ray working group at IceCube for the help and input I got from you.

A huge thanks to the WAB-team at KIT for always making Friday evenings interesting. My special thanks goes to Katrin and Donghwa, for always being there to listen to my worries and for the wonderful discussions. Thanks to Anne and Frank for practising German with me and motivating me to learn the language.

Thanks to Sabine for being a constant, reliable person. Life at IKP would have crumbled without you. I really appreciate the efforts of Doris to make our lives easier at IKP. Thank you for continuously taking care of our computing system, and for all the additional computing privileges ;) Thanks a lot to Jürgen for taking care of all my parallel simulations, for taking care of our lsdf space and all of our jobs. Also, thank you for taking care of our daily morning coffee!

It has been wonderful to share my office with Anne, Katrin, Agnieszka, Marie and Fiona. It has truly been a lively and fun place to work, with mutual respect and friendship. Thanks for all the useful discussions and scientific input.

Thanks to all of my friends, both near and far, for always being there for me. Thanks to Shyam, Veena and Geetu for being like my family away from home. I am eternally grateful to Ashik for his unending support and understanding, for always trying to cheer me up, and for keeping me grounded.

I would like to thank my family for their unwavering belief in me. Thank you Amma for always keeping me in your prayers, Acha for always encouraging and

understanding me and for being a pillar of strength, and Appooppa for always motivating me to follow my passion.

Erklärung

Karlsruhe, den 23.01.2019

Erklärung der selbständigen Anfertigung meiner Dissertationsschrift

Hiermit versichere ich, dass ich die Dissertationsschrift mit dem Titel

A Quest for PeVatrons Employing
Radio Detection of Extensive Air Showers

selbständig und ohne unerlaubte fremde Hilfe verfasst habe. Dabei habe ich keine anderen, als die von mir angegebenen Hilfsmittel benutzt.

Aswathi Balagopal V.